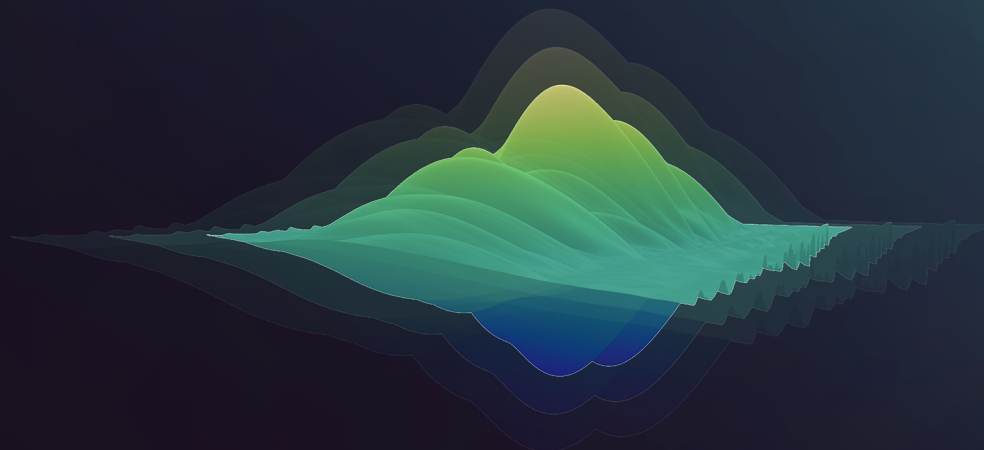


Submerged Floating Tunnel:

A structural response optimization of the transition structure subjected to earthquakes

by

J.M. Aalbers



This page was intentionally left blank

Submerged Floating Tunnel:

A structural response optimization of the transition structure subjected to earthquakes

by

J.M. Aalbers

To obtain the degree of Master of Science
At Delft University of Technology,
to be defended publicly on Friday September 30 at 11:00 AM.

Student number:	4913256
Project period:	December 2021 - September 2022
Graduation committee:	
Dr.ir. A. Tsouvalas,	Department of Offshore Engineering & Dynamics of Solids and Structures, TU Delft
ir. T. Molenkamp,	Department of Offshore Engineering, TU Delft
Dr. ir. K.N. van Dalen,	Department of Dynamics of Solids and Structures, TU Delft
ir. A. Luttikholt,	Tunnel Engineering Consultants (TEC)

An electronic version of this thesis is available at <http://repository.tudelft.nl/>.

Cover Image: Statens Vegvesen



This page was intentionally left blank

Preface

Dear reader,

This is my thesis report which finalizes my Master's study in Structural Engineering with specialisation in Structural Mechanics at TU Delft. The project is carried out in collaboration with Tunnel Engineering Consultants (TEC) and the Faculty of Civil Engineering and Geosciences of TU Delft.

Moreover, this challenging period finalizes an important stage of life after 8 years of studying, including 4 years of Hbo Civil Engineering, a 1.5 year pre-Master's and finally a 2.5 year Master's. I look back on this formative period as a time where I got to truly discover where I am passionate about and had the opportunity to meet many wonderful people along the way.

I would like to thank several people who helped me throughout the past 10 months on an intellectual and personal level. First of all, I would like to express my gratitude to my thesis committee: Dr. ir. A. Tsouvalas, ir. T. Molenkamp, Dr. ir. K.N. van Dalen and ir. A. Luttikholt. Thank you for your time, motivating words and advice in finding the right direction for the project. Next, I would like to thank Arjan Luttikholt from TEC/Witteveen+Bos for not only providing guidance in the thesis project, but also showing me the broader range of possibilities after my studies. Thank you Timo, for elaborately taking the time to explain the complex matter, especially in the earlier stages of this thesis. You helped me see how complicated problems could often be solved in a rather simple way.

But at the end of the day, when the laptop is shut, I felt lucky to have my girlfriend Nina and my good friends and family to make this time not only educational but also enjoyable. They were able to give me perspective and keep me motivated, even when some frustrations arose. Special thanks to Nina for your patience, love and willingness to hear so much about tunnels and earthquakes. Lastly, I want to express my gratitude to my parents for giving me the opportunity to study and inspire me to not always take the shortest route, but inspire me to do Hbo first and then a Master's.

With everyone together, the last years were a meaningful and thought-provoking period. Now that this thesis is completed, I look forward to the opportunities that are coming next.

*Jesper Aalbers,
Delft,
September 23, 2022*

Abstract

This study presents the structural response of a Submerged Floating Tunnel (SFT) subjected to earthquake loading and other relevant static loading types. The SFT is a competitive solution for crossings of deep seas, canals and fjords, as it is submerged in water and floats at a fixed submersion depth. It is supported by its buoyancy and tethers, connected to the seabed to maintain the structure at an even submersion level. Influence on the environment is low compared to other competitive structures, as the structure does not occupy any surface of the seabed, except for the tether foundations. Moreover, the environment has little influence on the SFT's operability, as it is insensitive to harsh weather conditions. However, in areas of high seismicity, the SFT's dynamic characteristics must be carefully tuned to the expected type of earthquake to optimize its performance. Previous research showed that special care should be taken of the transition between the SFT and land tunnels, as this joint has proven itself to be the main challenge.

The purpose of this research is to alter the transition structure between the SFT and adjacent land tunnels, such that an optimal dynamic response of a SFT is found to seismic events (Chapter 1). Initially, its performance is measured by comparing the seismic serviceability limit state (SLS) response to the static ultimate limit state (ULS) response. Subsequently, for more severe earthquakes, it is measured by comparing the SLS seismic stresses with maximum allowed levels of concrete prestress.

To analyse the SFT behaviour, a global model has been created of the SFT+land-tunnel system in Chapter 3, which is built by means of a linear-elastic finite element method in Python. It accounts for dynamic loads through the soil and tethers, as well as static loads by the structure's weight, traffic and buoyancy. The influence of stagnant water is accounted for by the Morison equation. Soil-Structure-Interaction (SSI) is incorporated using a Substructuring method. The properties of the soil and tethers are found in local sub-models, after which the total structural response of the global model is solved in the frequency domain. Later, its response is transformed to the time domain to obtain a time-series of displacements and forces. Its dynamic characteristics are studied by comparing Fourier spectra with SFT natural frequencies, which gives insight in the influence of design choices on the time-domain response.

The global model is validated with a replica model in the finite element software DIANA FEA (Chapter 4). A realistic case study is defined based on a previous TEC project in Chapter 5 and later applied in a parameter study in Chapter 6. Here, the effects of various design choices with respect to the transition structure are monitored using 3 earthquake signals. 5 standard end-joints and 2 special end-joints with seismic base isolation and viscous dampers are tested. The effects of Multi-Support-Excitation is studied by letting earthquakes horizontally approach the SFT with various wave speeds and angles of attack. Finally, the effect of SSI is compared with a non-SSI case, to see its contribution to the research.

In Chapter 7, the results are discussed and in Chapter 8 a conclusion is provided together with recommendations for both TEC and future research.

List of Figures

2.1	Visualisation of SFT supported by tethers	4
2.2	Schematization of longitudinal cross-section	5
2.3	Archemedis' principle	5
2.4	Examples of SFT cross-sections	6
2.5	Mechanics of end-joint	8
2.6	Monolithic end-joint	8
2.7	Hinge end-joint	9
2.8	Hinge with bending capacity end-joint	9
2.9	Seismic base isolation with fuse end-joint	10
2.10	Hinge with viscous damper end-joint	10
2.11	P-wave (a) & S-wave (b) (schematized)	12
2.12	Love wave (c) & Rayleigh wave (d) (schematized)	12
2.13	Worming (left) and Snaking (right) deformation modes due to passing waves	13
2.14	Single DOF model (Stewart et al., 1999)	14
2.15	Winkler (a), Filonenko-Borodich (b) & Pasternak foundations (c)	15
3.1	Mechanical scheme	20
3.2	Tether descritization	25
3.3	Absolute tether stiffness, phase angle and flexibility	25
3.4	Soil-structure interaction model	26
3.5	Comsol boundary & interface conditions	27
3.6	Load application lines	27
3.7	Mooring lines schematized (left) & Non-linear force-elongation relationship (right)	28
3.8	Flow chart of the Python code	29
4.1	DIANA validation model	30
4.2	Input signal	32
4.3	comparison of eigen frequencies	32
4.4	Mode shapes of the python validation model	33
4.5	Comparison of longitudinal displacements	34
4.6	Comparison of horizontal displacements	34
4.7	Comparison of vertical displacements	34
4.8	Comparison of horizontal bending moments	35
4.9	Comparison of vertical bending moments	35
4.10	Comparison of normal forces	35
4.11	Comparison of horizontal shear forces	36
4.12	Comparison of vertical shear forces	36
4.13	Comparison of tether normal forces	37
5.1	Location (in blue): Golden Horn, Istanbul, Turkey (Meriç et. al., 2007)	38
5.2	Geological profile of building site (modified from Meric et al., 2007)	39
5.3	Scaled, symmetrical geological profile	39
5.4	Tunnel cross-section	41
5.5	Linearized Gina stiffness	42
5.6	Fourier spectrum of Acceleration signals	45
5.7	Acceleration signals (scaled to 0.1 g)	45
5.8	Displacement signals (scaled to 0.1 g)	46
6.1	Load Model 1 (NEN-EN-1991-2 table 4.2)	48
6.2	Load Model 1 (NEN-EN-1991-2 figure 4.2a)	48
6.3	Static displacements, bending moments and stresses - SLS without traffic	49
6.4	Static displacements, bending moments and stresses - SLS	50
6.5	Static displacements & internal forces - ULS	51
6.6	Longitudinal eigen frequencies for several end-joints	52
6.7	Longitudinal eigen modes (hinged end-joint)	53
6.8	Longitudinal Fourier transform & Natural frequencies of horizontally rigid joints	53

6.9	Longitudinal Fourier transform & Natural frequencies of horizontally flexible joint (GINA/10)	53
6.10	Longitudinal displacements of Bingol (left), Derince (middle) & Van (right) - monolithic end-joint - synchronized loading	54
6.11	Normal forces of Bingol (left), Derince (middle) & Van (right) - monolithic end-joint - synchronized loading	55
6.12	Vertical natural frequencies for several end-joints	55
6.13	Vertical eigenmodes (hinged end-joint)	56
6.14	Vertical Fourier transform & Natural frequencies of monolithic end-joint	56
6.15	Vertical Fourier transform & Natural frequencies of hinged end-joint	56
6.16	Vertical results (Bingol) - monolithic end-joint - synchronized loading	57
6.17	Vertical results (Derince) - monolithic end-joint - synchronized loading	57
6.18	Vertical results (Van) - monolithic end-joint - synchronized loading	57
6.19	Horizontal natural frequencies for several end-joints	58
6.20	Horizontal eigenmodes (hinged end-joint)	58
6.21	Horizontal Fourier transform & Natural frequencies of monolithic end-joint	59
6.22	Horizontal Fourier transform & Natural frequencies of hinged end-joint	59
6.23	Horizontal results (Bingol) - monolithic end-joint - synchronized loading	59
6.24	Horizontal results (Derince) - monolithic end-joint - synchronized loading	60
6.25	Horizontal results (Van) - monolithic end-joint - synchronized loading	60
6.26	Modes of most rigid end-joint types in longitudinal, horizontal and vertical direction	61
6.27	Modes of most flexible end-joint types in longitudinal, horizontal and vertical direction	61
6.28	Derince - Influence of end-joint on displacements (relative to the monolithic joint)	62
6.29	Comparison of monolithic and hinged natural frequencies with the Derince acceleration spectrum	63
6.30	$\sigma_{sft,1}$ & $\sigma_{sft,2}$ definitions	63
6.31	Surrounding normal stress lines (Van) - monolithic end-joint - synchronized loading	64
6.32		64
6.33	Maximum, minimum and difference of stresses per end-joint (Derince)	65
6.34	Tether stress results of Derince 0.1g with reduced tether stiffness ($A_{teth} = 0.150m^2$)	66
6.35	Influence of reduced tether stiffness on key parameters	66
6.36	Derivation of time delay t_0 due to angle of attack α	68
6.37	Maximum displacements for various shear wave speeds, normalized with respect to synchronized results	69
6.38	Maximum internal forces for various shear wave speeds, normalized with respect to synchronized results	70
6.39	Maximum stresses for various shear wave speeds, normalized with respect to synchronized results	70
6.40	Normalized maximum displacements for various angles of attack	71
6.41	Normalized maximum internal forces for various angles of attack	71
6.42	Normalized maximum stresses for various angles of attack	71
6.43	Wave velocity and arrival time of seismic wave	72
6.44	Increment of various parameters due to vertical traveling wave compared to synchronous support excitation	72
6.45	Laminated Rubber Bearing (a) & schematized displacement (b)	74
6.46	Longitudinal natural frequencies with base isolation and Fourier acceleration spectra	75
6.47	Result of base isolated end-joint - Derince (PGA=0.1g)	75
6.48	Result of GINA/10 end-joint with viscous damper - Van (PGA=0.1g)	76
6.49	Vertical displacement w_z - Monolithic end-joint - Van 0.1g	77
6.50		78
6.51	Vertical natural frequencies for standard and increased number of tethers	78
6.52	Influence SSI on horizontal natural frequencies with Van Fourier transform - Monolithic end-joint	79
6.53	Normalized influence of SSI on parameters - Monolithic end-joint	79
6.54	Comsol results: longitudinal displacement u_x due to vertical harmonic load	80
6.55	Longitudinal shortening (simplified)	80
6.56	Comsol results: longitudinal displacement u_x due to Horizontal harmonic load at location 10	81
6.57	Comsol results: horizontal displacement w_y due to vertical harmonic load	81
A.1	Shape function visualisation for EB-beam (left) and rod (right)	92

A.2	Full mass matrix of rod + 2D beam incl. added mass	93
A.3	Full stiffness matrix of rod + 2D beam	94

List of Tables

3.1	Geometrical properties of local model 2	26
5.1	Geological material characteristics	40
5.2	Material properties	40
5.3	Cross-sectional properties	41
5.4	End-joint spring stiffness parameters	43
6.1	Results end-joint with viscous damping - Van (scaled to PGA=0.1g)	76

Nomenclature

Abbreviations

Abbreviation	Definition
BC	Boundary Condition
BOEF	Beam on Elastic Foundation
BWR	Buoyancy-Weight Ratio
EB	Euler Bernoulli
FFT	Fast Fourier Transform
IC	Interface Condition
LHS	Left Hand Side
MEP	Mechanical, Electrical & Plumbing
MSE	Multi Support Excitation
SFT	Submerged Floating Tunnel
ODE	Ordinary Differential Equation
PDE	Partial Differential Equation
PGA	Peak Ground Acceleration
RHS	Right Hand Side
SLS	Serviceability Limit State
ULS	Ultimate Limit State

List of Symbols

Symbol	Definition	Unit
a_g	Ground acceleration	$[\frac{m}{s^2}]$
A	Cross-sectional area of SFT / land tunnel	$[m]$
A_{displ}	Area of water displacing body	$[m^2]$
A_{moor}	Mooring line cross-sectional area	$[m^2]$
A_{sft}	SFT cross-sectional area	$[m^2]$
A_{teth}	Tether cross-sectional area	$[m^2]$
\mathbf{c}_e	Element damping matrix	$[\frac{kNs}{m}]$
$c_{morison}$	Morison damping	$[\frac{kNs}{m}]$
c_x	End-joint longitudinal damping	$[\frac{m}{kNs}]$
$c_{\theta z}$	End-joint vertical rotation damping	$[\frac{kNms}{rad}]$
$c_{\theta y}$	End-joint horizontal rotation damping	$[\frac{kNms}{rad}]$
\mathbf{C}	Global damping matrix	$[\frac{kNs}{m}]$
C_D	Drag coefficient	[-]
C_M	Added mass coefficient	[-]
D	Tunnel diameter	$[m]$
E	Young's Modulus	$[\frac{kN}{m^2}]$
\mathbf{f}	Force vector in time domain	$[kN]$
$\tilde{\mathbf{f}}$	Force vector in frequency domain	$[kN]$
$f_{y,d}$	Design yield stress of steel	$[MPa]$
$F_{buoyancy}$	Buoyant force	$[kN]$
$F_{selfweight}$	Self-weight force	$[kN]$
g	Gravitational acceleration coefficient	$[\frac{m}{s^2}]$

Symbol	Definition	Unit
h	Finite element size	[m]
I	Moment of Inertia	[m^4]
k_{moor}	Mooring line stiffness	[$\frac{kN}{m}$]
\tilde{k}_{soil}	Dynamic soil stiffness	[$\frac{kN}{m^2}$]
\tilde{k}_{tether}	Dynamic tether stiffness	[$\frac{kN}{m}$]
k_x	End-joint longitudinal stiffness	[$\frac{kN}{m}$]
$k_{\theta z}$	End-joint vertical rotation stiffness	[$\frac{rad}{m}$]
$k_{\theta y}$	End-joint horizontal rotation stiffness	[$\frac{rad}{m}$]
\mathbf{k}_e	Element stiffness matrix	[$\frac{kN}{m}$]
\mathbf{K}	Global stiffness matrix	[$\frac{kN}{m}$]
L_{ctc}	Horizontal center-to-center distance between SFT tubes	[m]
L_{land}	Land tunnel length	[m]
L_{moor}	Mooring line center-to-center distance	[m]
L_{sft}	SFT length	[m]
L_{teth}	Tether center-to-center distance	[m]
N_{xx}	Normal force	[kN]
m_{add}	Added mass	[$\frac{ton}{m}$]
\mathbf{m}_e	Element mass matrix	[$\frac{ton}{m}$]
\mathbf{M}	Global mass matrix	[$\frac{ton}{m}$]
M_{yy}, M_{zz}	Horizontal & vertical bending moment	[kNm]
t	Time	[s]
t_0	Time delay	[s]
u_b	Body displacement	[m]
u_w	Water displacement	[m]
v_s	Shear wave velocity	[$\frac{m}{s}$]
V_{yy}, V_{zz}	Horizontal & vertical shearforce	[kN]
\tilde{W}_g	Fourier ground displacement	[m]
$\tilde{W}_x, \tilde{W}_y, \tilde{W}_z$	Structural frequency domain displacement in x, y & z	[m]
x	Location on longitudinal axis of global coordinate system	[m]
y	Location on vertical axis of global coordinate system	[m]
z	Location on horizontal axis of global coordinate system	[m]
α	Angle of attack of a seismic wave	[$^\circ$]
α_R	Rayleigh mass coefficient	[-]
β_R	Rayleigh damping coefficient	[-]
γ_{sat}	Saturated specific soil weight	[$\frac{ton}{m^3}$]
δ_h	Maximum allowed horizontal displacement	[m]
δ_z	Maximum allowed vertical displacement	[m]
λ	Wave length	[m]
ρ	Specific weight of SFT / land tunnel material	[$\frac{ton}{m^3}$]
ρ_c	Specific weight of concrete	[$\frac{ton}{m^3}$]
ρ_w	Specific weight of water	[$\frac{ton}{m^3}$]
$\sigma_{sft,1}$	Vertical outer fibre stress in SFT cross-section	[MPa]
$\sigma_{sft,2}$	Horizontal outer fibre stress in SFT cross-section	[MPa]
σ_{teth}	Tether stress	[MPa]
σ_v	Standard deviation of earthquake input velocity	[$\frac{m}{s}$]
ω	Radial frequency	[$\frac{rad}{s}$]

Contents

Acknowledgements	ii
Abstract	iii
List of figures	vi
List of tables	vi
Nomenclature	viii
1 Introduction	2
1.1 Objective	3
1.2 Research question	3
1.3 Sub-questions	3
1.4 Scope	3
2 SFTs in a Seismic Environment	4
2.1 Submerged Floating Tunnels	4
2.1.1 Buoyancy	5
2.1.2 Shapes & Materials	6
2.1.3 End joints	8
2.2 Earthquakes	11
2.2.1 Types of waves	12
2.2.2 Effects of passing waves on tunnels	13
2.3 Soil-structure interaction	14
2.3.1 Single DOF spring models	14
2.3.2 Distributed spring models	15
2.3.3 Substructuring approach	15
2.4 Fluid-structure interaction	17
2.4.1 Morison's equation	17
3 Methods	18
3.1 Assumptions	19
3.1.1 Non-linearities	19
3.1.2 Meshsize	19
3.1.3 Coupling	19
3.1.4 Local site response & amplification	19
3.2 Model description	20
3.2.1 Solution method	20
3.3 Global model - SFT & Land tunnel	21
3.3.1 Equations of Motion	21
3.3.2 Boundary & Interface conditions	23
3.4 Local model 1 - Tethers	25
3.5 Local model 2 - Soil	26
3.5.1 Comsol model	26
3.5.2 Boundary conditions	27
3.5.3 Loading	27
3.5.4 Bedding matrix assembly	27
3.6 Mooring lines	28
3.7 Python code	29

4	Validation of the model	30
4.1	DIANA & Python model	30
4.2	Loading	31
4.3	Results	32
5	Case study	38
5.1	Location	38
5.1.1	Geological material characteristics	40
5.2	Cross-sectional properties	40
5.3	End-joint properties	41
5.3.1	End-joint with bending capacity	42
5.3.2	End-joint with viscous damper	43
5.4	Earthquake signals	44
6	Parameter study	47
6.1	Static behavior	47
6.1.1	Static loading	47
6.1.2	Static results	49
6.2	Dynamic behavior	52
6.2.1	Longitudinal dynamic behavior	52
6.2.2	Vertical dynamic behavior	55
6.2.3	Horizontal dynamic behavior	58
6.2.4	Evaluation of the synchronized results	61
6.2.5	Effect of multi-support excitation	68
6.2.6	Alternative closure joints	74
6.2.7	Evaluation of the Effect of SSI	79
6.2.8	Evaluation of the effect of soil coupling	80
7	Discussion	82
7.1	Discussion on assumptions	82
7.1.1	Geometrical Non-linearity's	82
7.1.2	Material Non-linearities	82
7.1.3	Land tunnel element size	82
7.1.4	Coupling	83
7.1.5	Rayleigh Damping	83
7.1.6	Morison Damping	83
7.2	Discussion on results	84
8	Conclusion & recommendations	85
8.1	Conclusion	85
8.2	Recommendations for design of SFTs	88
8.3	Recommendations for future research	88
	References	89
	Appendices	91
	Appendix A Shape functions, Mass & Stiffness matrix definitions	92
	Appendix B Spring-dashpot interface element definitions	95
	Appendix C Results	96
C.1	Synchronized support excitation analysis results	96
C.1.1	Bingol	96
C.1.2	Derince	97
C.1.3	Van	97
C.2	Multi-Support-Excitation with various shear wave velocities - results	98
C.3	Multi-Support-Excitation with various angles of attack - results	99

Chapter 1

Introduction

In December 2020, the European Parliament signed the European Green Deal ([EC, 2022](#)): the EU's plan to make its economy more sustainable by achieving climate neutrality by 2050. A vital element of the plan is to roll out cleaner and healthier means of transport, as the transport sector is currently responsible for about 25% of the Union's greenhouse gas emissions. The European Green Deal seeks a 90% reduction in transport emissions by 2050. As part of the deal, the European Commission adopted its Sustainable and Smart Mobility Strategy, which included doubling rail freight and tripling highspeed rail activity by 2050. To do so, European countries need to be better interconnected to establish high speed railway connections across country borders.

In this process more structures are needed to span deep canals, lakes, seas and estuaries. Uptil now, most straightforward (long span) connections have been constructed across the more shallow waters by means of suspension bridges, floating bridges, bored and immersed tunnels. Currently, worlds deepest immersed tunnel, situated in Marmaray (Turkey), is built at an immersion depth of 60 meters. Bored tunnels can reach even greater depths, but at the cost of a large increase in length due to limitations in maximum slope. For bridges, the maximum depth of piers is at currently 122 meters below river level (Padma bridge, Bangladesh), but these come with high building costs. Intermediate supports can alternatively be founded on floating pontoons, provided that the local sea conditions are mild and that sea traffic is not hindered by the limited vertical clearance. However, when this is not the case and is combined with a deep and uneven seabed, out-of-the-box solutions are needed.

The Submerged Floating Tunnel (SFT), also known as a Submerged Floating Tube Bridge (SFTB), suspended tunnel or Archimedes bridge, might be the solution to solve these engineering challenges. It is a conceptual idea for a tunnel, submerged in water, floating at a certain immersion depth and supported by its buoyancy and steel tethers. Broadly speaking there exist two versions of the SFT: one with tethers connected to the seabed and one where tethers are connected to floating pontoons at the water surface. Mooring lines ensure that the tunnel stays in position when strong currents are present at the building site.

The idea of a floating tunnel is not new but dates back to 1886 and has been re-proposed as a concept to span waterways over the duration of the last century. Technologies to build such a structure were not available for a long time, but tools for construction and engineering got more advanced in the last decades. Knowledge that has been acquired in offshore engineering, while building tension leg platforms, can be transferred to the design of Submerged Floating Tunnels. This can make the construction of the first SFT one step closer. As a consequence, many studies and designs have been conducted in China, Japan, Norway and Italy in the last 15 years, but so far it has not resulted in the start of construction of the first SFT. It seems that more studies on the reliability and interference of the wide load spectrum will have to be performed to better understand its behavior.

1.1 Objective

The objective of this thesis project is to gather a set of design recommendations for the transition structure between a SFT and land tunnel. These recommendations shall be based on a Frequency Domain method that includes the effect of Soil-Structure Interaction and Fluid-Structure interaction. The dynamic stiffness of the soil around the land tunnel and the dynamic stiffness of the tethers must be derived in dynamic sub-models to account for their frequency dependent stiffness and radiation of energy. The obtained model will be applied in a case study where different variants of the transition structure shall be exposed to a variety of earthquakes to find a suitable end-joint. The resulting conclusions and recommendations can serve as guidance for future design of SFTs.

1.2 Research question

How can the design of the transition structure of a SFT be optimized such that the SLS dynamic stresses are closest to the ULS static stresses and displacements are within design requirements?

1.3 Sub-questions

1. What types of transition structures and joints can be used and which would be the most suitable for a SFT-shore connection?
2. How can the transition structure be properly modelled including the effects of the SFT and the land tunnel?
3. What method is most appropriate for assessing the dynamic model subjected to earthquake and other relevant loading types?

1.4 Scope

In the following the section the phenomena are described that are taken into account in this thesis project.

- Only global deformations and stresses in longitudinal direction will be assessed with analytical methods.
- Fluid structure interaction will be considered as damping. Currents & waves will not be taken into account.
- Pressure waves through water resulting from submarine earthquakes will not be taken into account.
- The effects and loads resulting from tsunamis will not be taken into account.
- Loads resulting from selfweight, buoyancy, traffic and earthquakes will be taken into account.

What geometries of the tunnel will we take into account?

- Only the SFT variant with tether-seabed supports is assessed, since this variant is most prone to earthquakes.
- During the parametric study one tunnel cross-section is used for the SFT and one for the land tunnel.

Chapter 2

SFTs in a Seismic Environment

This chapter describes the current state of knowledge for the 4 fundamental concepts this thesis is based on. The SFT structure and the phenomenon of earthquakes are further clarified, subsequently the interface of the structure with respectively soil and water are examined. This will illustrate their effects on the structures dynamic behavior and describe how to take them into account in a model.

2.1 Submerged Floating Tunnels

A submerged floating tunnel (see Figure 2.1) essentially contains a tubular structure, floating underwater, supported by its buoyancy and restoring pretension forces. The pretension forces originate from tethers that secure the elevation of the tube by vertically fastening it to the seabed. At the seabed the tether can attach to a gravity structure or anchor piles to transfer the tensile forces. The tethers are hollow circular members, preferably made out of steel, with diameters ranging from 1 up to 2.5 meters. The diameter and thickness of the tethers are chosen such that the stresses remain far below the yield limit of steel to prevent fatigue damage. Next, the tethers need a neutral buoyancy weight ratio such that the weight of the hollow section is equal to the upward buoyancy. This way, the self-weight of the tethers will be counteracted, such that they do not add extra weight to the SFT.

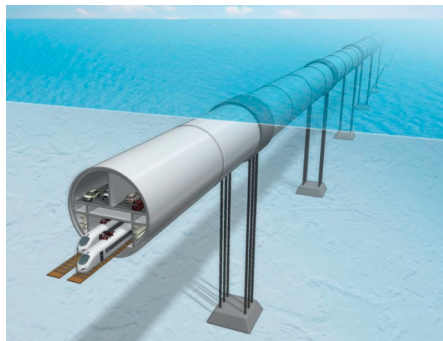


Figure 2.1: Visualisation of SFT supported by tethers

At either sides of the SFT, the structure transitions into land tunnels that start at SFT submer-
sion depth and ascend towards ground level through soil or rock (Figure 2.2). Depending on the
nature of the substrate, the type of land tunnel can vary between cut-and-cover or bored tunnels
in softer substrate types, to bored or sequentially excavated tunnels in harder types of substrate.
At the interface between the SFT and the land tunnel, a transition structure must be constructed
with the desirable type of immersion joint and possibilities to attach both tunnel types from either
sides. The transition structure can be built as a concrete box with an extra cellar for bearing
blocks, possible damping devices or seismic base isolators and room for maintenance activities.
Water tightness must be secured by use of rubber sealing profiles.

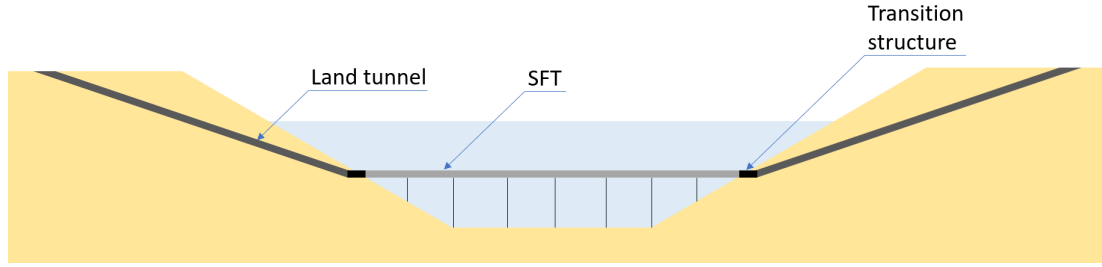


Figure 2.2: Schematization of longitudinal cross-section

2.1.1 Buoyancy

Buoyancy occurs when an object has the ability to float in a fluid. It is the upward force exerted on the object by the water body that opposes the weight of the immersed object. The ratio between the buoyant force and the objects weight determines the objects ability to float and is called the Buoyancy-Weight-Ratio or BWR.

$$\text{BWR} = \frac{F_{\text{buoyancy}}}{F_{\text{self weight}}} \quad (2.1)$$

Structures that have a positive BWR (greater than 1) are able to float in water, and the contrary (BWR below 1) means that the structure will sink without any mitigating measures. It is a key principle in the concept of SFTs, as the tubes buoyancy works like a support for the structure. Fluctuations in water levels, currents and a need for horizontal stability make that the buoyancy alone is not enough to support the SFT. Additional supports are needed using tethers connected to the seabed combined with a SFT with a positive BWR or connected to floating pontoons with a negative BWR. A study by Long, Ge & Hong (Long, Ge, & Hong, 2015) demonstrated that a BWR of 1.2 would be the most promising choice for SFTs based on the dynamic response and guidelines for security and comfort. Higher BWRs increase the amount of comfort, but come with larger monetary costs.

In the process of SFT cross-section design, the BWR is one of the first design objectives that shall be satisfied. The SFTs self weight can be found as the product of the cross-sectional area with the specific weight of the concrete. The buoyant force is defined by Archemedis' principle, which states that the buoyant force equals the weight of the fluid displaced by the objects body (see Figure 2.3).

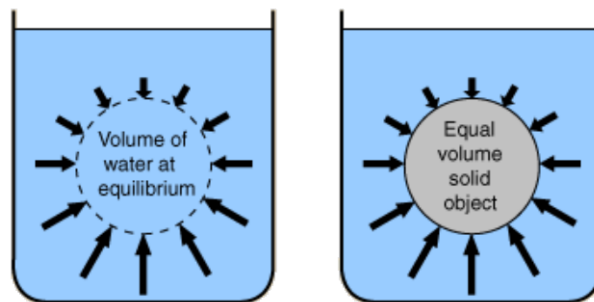


Figure 2.3: Archemedis' principle

$$\text{BWR} = \frac{A_{\text{displ}} \rho_w}{A_{\text{sft}} \rho_c} \quad (2.2)$$

For the cross-sectional design of the tethers the BWR (equation 2.2) is of importance as well, since the distribution of material and hollow area in the section can be chosen such that the tether possesses a neutral BWR. This way the tethers do not add any additional weight the the SFT structure, which is favourable.

2.1.2 Shapes & Materials

In preliminary designs of floating tunnels, various cross-sections have been proposed as can be found in literature. Many geometrical arrangements are available for the external SFT shape. The geometry of the cross section has to comply with several requirements. It must be easily manufactured, have enough buoyancy capacity and good hydrodynamic behavior with enough internal space to accommodate all required facilities and profile of free space for vehicles.

2.1.2.1 Cross-sections for smaller spans ($L \leq 500$ m)

The most straightforward shape and most commonly used in immersed tunnel design since the 1930s (Detroit Windsor tunnel) is the rectangular cross-section (Figure 2.4, top-right). It is relatively easy to manufacture due to use of straight angles only and the geometry allows for versatility in the organization of internal space (Martire & Mazzolani, 2010). Immersed tunnels however are not subjected to hydrodynamic action since they are embedded in a trench and covered by soil or rock. The rectangular shape would cause turbulence when submerged in a moving fluid. This problem could be overcome by use of a steel streamlined shell at either sides of the tunnel, creating a rounded surface over the flat walls. The result would be an inefficient use of area inside the shell, and the need to add many stiffeners inside it to prevent bending and buckling. Thus, a more rounded shape is preferred where the main load bearing walls also serve as outer walls.

Circular cross-sections (Figure 2.4, bottom-left) have been proposed repeatedly in preliminary SFT designs for the Messina Strait crossing, the Hogsfjord crossing and Sulafjord crossing. Although the manufacturability is of a more complex nature, the sections have a very good performance in hydrostatic pressures, as these only result in compressive stresses and no bending due to the internal hoop forces. The streamlined shape causes a lower resistance in moving fluid and the polar symmetry causes good hydro-dynamic stability: no sensitivity to flutter or torsional divergence phenomena (Martire & Mazzolani, 2010). Compared to the rectangular sections, its horizontal bending stiffness however is smaller, while this might be a very relevant quality for SFT's with larger spans (500+ meters). Namely, mooring lines only provide a limited amount of lateral stiffness to the system, thus a larger horizontal bending stiffness might be essential to decrease lateral displacements.

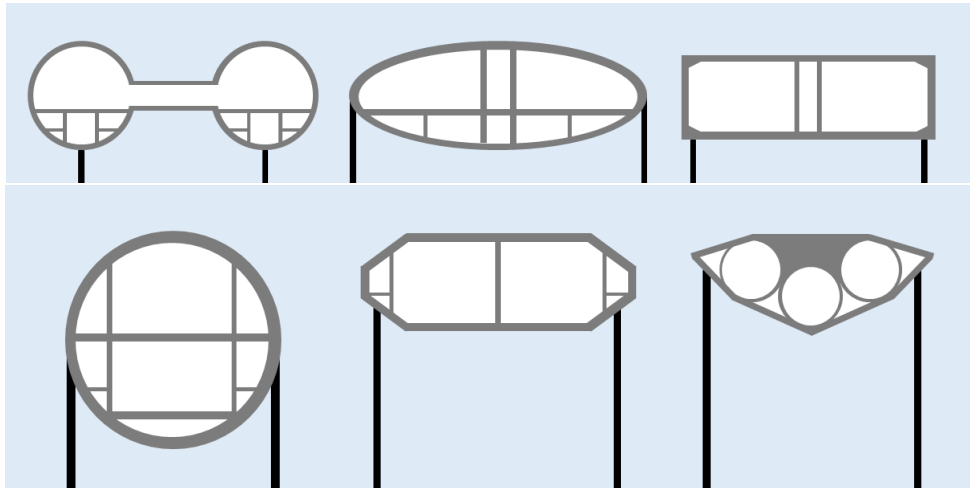


Figure 2.4: Examples of SFT cross-sections

2.1.2.2 Cross-sections for larger spans ($L > 500$ m)

When spans are increasing, cross-sections with a larger horizontal bending stiffness, but a higher degree of complexity (in terms of manufacturing), become more interesting. The single circular section can be reduced in height and horizontally stretched to create elliptical shaped sections. Alternatively, two smaller circular tubes can be used side-by-side, interconnected by cross-passages to create escape routes in case of emergencies. The double-circular shape acts like a horizontal truss structure, only adding material where it is most needed to restrain horizontal bending: the outer edges.

Elliptical sections as proposed by P. Zou (P. Zou, 2022) have a very good performance in horizontal water flow, with best balance in hydrodynamic performance and construction costs when the height to width ratio is 0.47. Li and Jiang (K. Li & Jiang, 2016) conducted numerical simulations to compare pressure distributions of rectangular and elliptical sections, combining fluid mechanical calculation with structural analysis. The conclusions of the report were that elliptical sections experience smaller displacements and stresses than the rectangular section. Li et al. (Q. Li, Jiang, & Chen, 2018) compared pressure characteristics of circular, elliptical and polygonal sections under wave impact. Circular sections experienced the largest wave forces, followed by the polygonal section and finally the elliptical section having the best performance.

Double circular sections as proposed by Speelman (Speelman, 2021) are constructed using two smaller sections, creating much less pressures by waves and currents due to the decreased vertical area that is in contact with surrounding water. Horizontal stiffness can be increased by simply placing the two tubes further apart, without adding too much more material (only in the bracings). In previous research the performance of one large circular section was compared to elliptical sections (Q. Li et al., 2018), but this was not done for two smaller sections. As the vertical surface of two sections next to each other is obviously smaller, the hydrodynamic forces also must be smaller. As this section has sufficient potential for optimizing the stiffness without drastically increasing the material use, this will be the cross section of choice for this research.

Other sections that have previously been considered are diamond shaped and octagonal sections. These sections seem to have inferior hydrodynamic properties compared to circular and polygonal sections, so these are not further investigated.

2.1.2.3 Materials

Materials to be used in SFT design shall have a proven performance and a lifetime of at least 100 years. Only well-known and reliable techniques and materials can be applied to ensure the safety and behavior of the new structure. For the SFT tube suitable materials are: steel, reinforced concrete, prestressed concrete and aluminium alloys. The tube can be constructed as one solid wall (steel or concrete) or as a sandwich of steel/aluminium with reinforced concrete. The advantage of using a steel wall combined with concrete is that buckling of steel and cracking of and leakage through the concrete will not be a problem. Also the steel can act as a formwork for the concrete, and then later be of use for the main load bearing tunnel wall. This way the steel and concrete can complement each other.

In case of a fully concrete tunnel, cracking can be counteracted by using pretensioned steel so that the full section is in compression. Alternatively, one can use a waterproofing membrane as mitigation measure where cracks are allowed to arise, but not grow above a certain limit. In the offshore industry, tethers are usually created out of synthetic fibres, rope, steel or aluminium alloys. As the forces and expected tether lengths are far above those of regular tethers, the first two options do not have the right qualifications for SFT tethers. Steel and aluminium remain. Steel has a high tensile strength, durability and is relatively resistant against fatigue. Aluminium on the other hand is light weight, not susceptible to corrosion, but has a lower resistance against fatigue. Therefore steel is the preferred material for the tethers.

Nowadays steel qualities up to S1300 exist, and pretension steel with steel qualities of FEP 1860 and FEP 2060 are not uncommon. Here the number indicates the yield strength in MPa. Dependent on the stress properties in the tethers an appropriate steel strength can be chosen. The stress difference due to traffic and hydrodynamic loads can however not be more than 200 MPa,

to prevent excessive fatigue damage.

2.1.3 End joints

The focus of this thesis is at the influence of seismicity on the transition structure. At the transition between SFT and landtunnel several types of joints can be realized, depending on the desired degree of restraints. The mechanics of the end-joint can be determined by a possible application of a spring (k_x) and a dashpot (c_x) at the interface between the SFT wall and the land tunnel wall (see Figure 2.5). This spring-dashpot can be applied around the full circumference of the tunnel tube or at discrete locations.

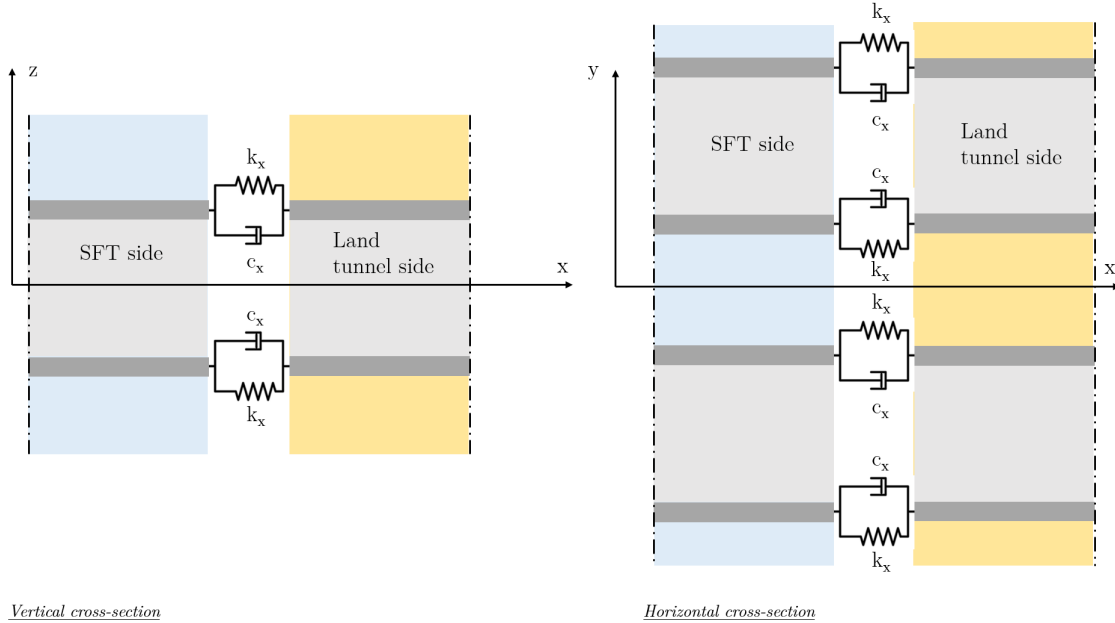


Figure 2.5: Mechanics of end-joint

2.1.3.1 Basic variants

In an ideal case, the end-joint is applied by letting the spring stiffness $k_x \rightarrow \infty$ and $c_x = 0$, such that a monolithic joint can be used (see Figure 2.6). The monolithic end-joint is preferred above other joints, because it ensures water tightness of the joint and has a higher durability, since no moving parts are involved. Due to lack of deformation capacity in monolithic joints, bending moments can grow large. When its capacity is exceeded the structural engineer must look at other alternative joints.

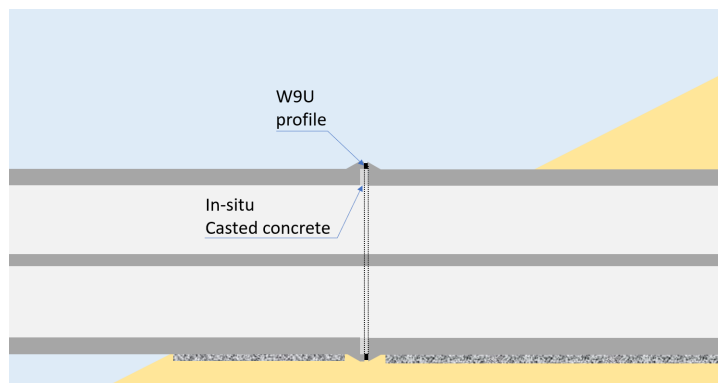


Figure 2.6: Monolithic end-joint

An obvious solution for problematic high bending moment is setting the stiffness and damping at the end-joint to zero ($k_x = c_x = 0$), to create a hinge connection. In practice this mechanical scheme

can be obtained by placing elastomeric bearing blocks or rubber gaskets around the circumference of the SFT-land-connection joint. The joint can be built in a dry environment and maintained throughout its lifetime by constructing a "joint house" (see Figure 2.7). To create a horizontal hinged connection, the same can be done at the sides. Waterproofing is ensured by means of a rubber omega profile.

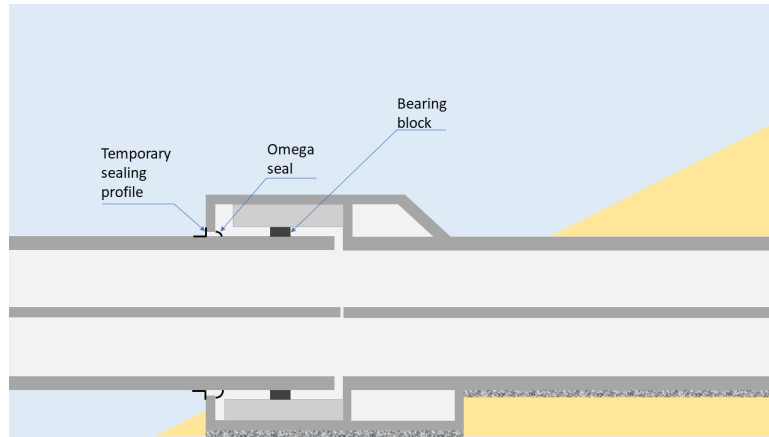


Figure 2.7: Hinge end-joint

Hinge connections can lead to large displacements over the SFT length and large rotations at the end-joint. If this is the case, the spring stiffness k_x can be increased to lower the displacements and create a connection with a horizontal and rotational spring stiffness. The damping values remain zero in this case ($c_x = 0$). A spring stiffness around the full circumference can be created using rubber gaskets, or optionally also rubber pads can be applied (see Figure 2.8). Pads and gaskets will add a small amount of damping to the system as well, although insignificant compared to hydraulic damping.

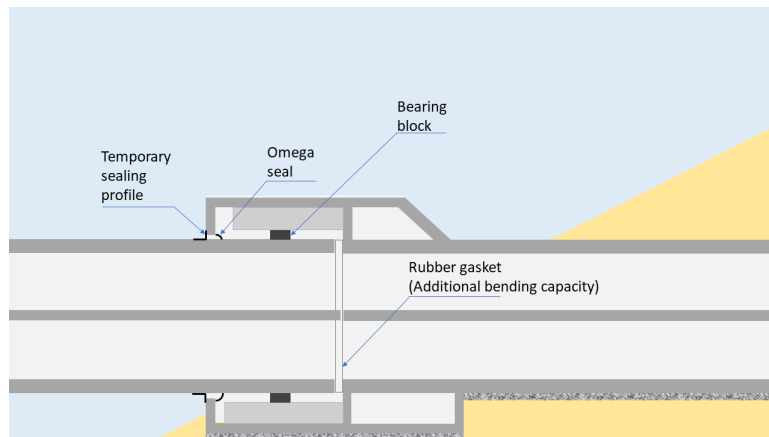


Figure 2.8: Hinge with bending capacity end-joint

2.1.3.2 Alternatives for areas with large seismicity

Deformations and internal forces might not stay within building code limits in case of large seismic activity. For bridges and buildings in seismically active areas, several solutions have been developed over the course of the last century and can be applied on a SFT structure.

Seismic base isolation is a popular method to decouple a superstructure from its substructure. It can be modelled by decreasing the longitudinal end-joint stiffness, without adding any rotational stiffness. Base isolation generally adds a significant amount of damping, depending on the type. Isolation can be created by applying elastomeric bearings, ball bearings, spherical bearings or spring systems. The system allows for large displacements in longitudinal direction and can therefore be combined with a "fuse": a component that sacrifices itself when a certain limit stress is exceeded. This combination ensures that longitudinal displacements will not exceed its limits

during serviceability limit state (SLS) situations, but allow for more flexibility in ultimate limit state (ULS) situations after the fuse breaks. Fuses are generally designed to be replaced within several days or weeks, so that infrastructure can be put back into use soon after an earthquake. An example cross-section of the transition structure with seismic base isolation and structural fuse is given in Figure 2.9.

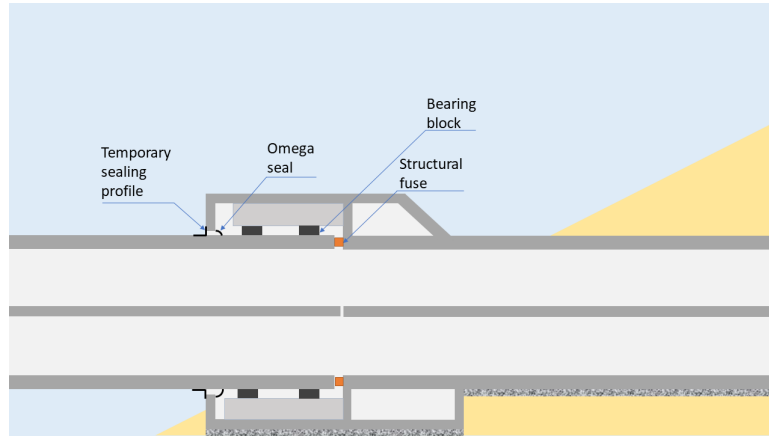


Figure 2.9: Seismic base isolation with fuse end-joint

Extra damping can be added to the joints displayed above, by adding viscous dampers at the top and bottom of the SFT (see Figure 2.10 for an example of the transition structure cross-section with viscous dampers). The dampers can be connected to the joint house to lead the forces to the foundation. Viscous damping is available in several forms, depending on the type of damper used. In this thesis a linear relationship ($a = 1.0$, see Equation 2.3) will be used between the velocity (v) applied to the damper end, and the reaction force (F) resulting from the damper. Non-linear damper with $0.3 \leq a < 1.0$ are available as well, but must be assessed using a non-linear time-history type of analysis.

$$F = c \times v^a \quad (2.3)$$

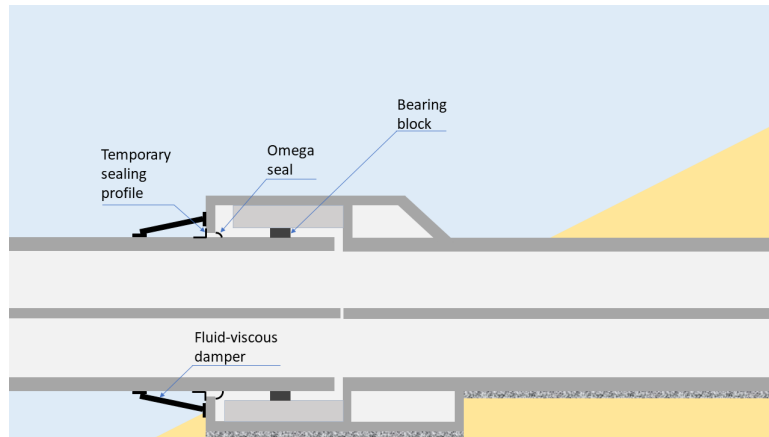


Figure 2.10: Hinge with viscous damper end-joint

2.2 Earthquakes

Earthquakes are in essence shaking of the ground, caused by a sudden release of energy inside the Earth's crust. This energy can originate from several sources, among them are volcanic eruptions, stresses induced by human activities (e.g. the extraction of gas, collapse of mines or explosions of chemical or nuclear devices), but foremost by tectonic activities (Ditmar, 2021). Tectonic plates are fragments of the outermost earth shell: the Lithosphere. It is broken up into 7 major plates and countless smaller plates. Below the lithosphere the earth's mantle is situated, where due to mantle convection, tectonic plates are constantly being created and consumed at their opposite boundaries. Mantle convection causes hot material to be added at the growing edge of a plate, and at the opposing edge dense material from the Lithosphere sinks into the mantle and is finally being absorbed by it. This causes tectonic plates to be constantly moving with respect to each other, which is now known as continental drift.

As the plate surfaces are rough, friction between plates causes stresses and strains to arise at the interfaces. Only when the strain energy is large enough it can be released by slipping of the plates (inter plate earthquakes) or by brittle ruptures inside of the plates (intra plate earthquakes). The earth then snaps back into its equilibrium position, causing vibrations to travel from the point of rupture (focus) to the earth's surface. These vibrations are known as "earthquakes".

Plate boundaries are categorized as divergent, convergent or transcurrent, depending on the relative movement of the adjacent plates. Next, the fault type of the plates can be classified into three main groups: the normal fault, the reverse fault and the strike-slip fault. The origin of a fault and its degree of activity is accounted for in a probabilistic seismic hazard analysis and thus of interest for the earthquake assessment of a structure. Additionally, the distance to the site is of interest. For near-fault projects the vertical ground motion, directivity effects* and high frequency content of the seismic signal shall be taken into account, whereas this is of less importance for projects at greater fault distance.

*Directivity is an effect of a fault rupturing whereby earthquake ground motion in the direction of rupture propagation is more severe than that in other directions from the earthquake source (USGS, 2022).

When the shearing of a fault originates at the focus, the body waves travel in the earth's interior, through hard bedrock and soil, to finally arrive at the building site of the SFT. When the wave passes from one soil type to another, refraction and reflection of the rays take place. These effects cause the ray direction to be changed, but also keeping a part of the seismic energy inside the first soil body. When a wave travels from a stiff to a softer soil, the wave bends upward and its speed is decreased, causing the wave front to approach the building site under an angle. This can lead to a phase shift in the time of arrival for a wave front to reach certain parts of the structure.

When an earthquake approaches the SFT it will cause excitations in the soil body surrounding the land-tunnels and transition structure. Additionally it will excite the foundation of the tethers, causing waves to travel through the tethers to the SFT. Since the tethers act relatively flexible, the forcing on the SFT (through the tethers) will mainly be of a vertical nature. For structures located in soft soils it is even possible for the soil to start resonating, which increases displacements and accelerations imposed to the tunnel. This effect can be taken into account using a local site response analysis.

Normally for smaller structures all components are excited by an earthquake simultaneously, but as SFTs are expected to have lengths exceeding 1 km, the earthquake will not arrive to all components in the same instance of time. This makes them prone to worming and snaking effects: two different modes of vibration, caused by respectively P- and S-waves arriving to the site horizontally.

2.2.1 Types of waves

Waves traveling through the earth's body can have 2 modes of vibration: either in compression or shear. When seismic waves are recorded by a seismographs the waves propagating in compression arrive first at the recording site, due to a larger wave velocity (c_s) where after the shear waves follow. Consequently, the two types of body waves in compression and shear are named Primary (P-)waves (Figure 2.11a) and Secondary (S-)waves (Figure 2.11b), with wave velocities c_S and c_P respectively. These can be approximated with the formulae below, where G is the shear modulus, ρ the density and k the bulk modulus of the material.

$$c_S = \sqrt{\frac{G}{\rho}}, \quad c_P = \sqrt{\frac{(4/3)G + k}{\rho}} \quad (2.4)$$

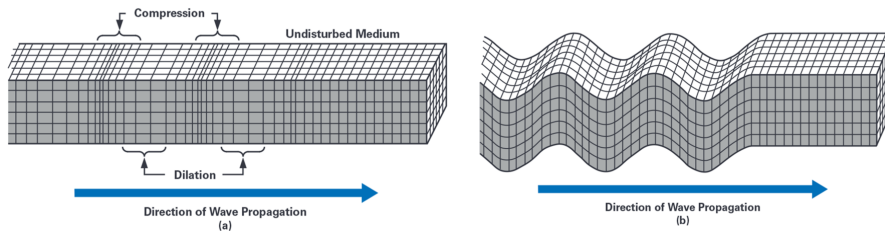


Figure 2.11: P-wave (a) & S-wave (b) (schematized)

P-waves are characterized by a particle motion in the same direction as the direction of propagation. For a S-wave, the particle motion is not in-line with the propagation direction, as the particles vibrate perpendicular to the wave direction, while propagating longitudinally. When body waves arrive at the surface of the earth, surface waves can be observed in the form of Rayleigh waves (Figure 2.12c) and Love waves (Figure 2.12d). Their amplitudes are maximum at the surface, and decay within several wavelengths into the subsoil.

Rayleigh waves are formed when longitudinal and transverse particle motion of P- and S- waves interfere, giving rise to an elliptical retrograde motion in the vertical plane, along the direction of propagation. Love waves are the second type of surface wave, having a horizontal transverse motion in shear. While body waves arrive at a building site approximately simultaneously, this is not the case for surface waves. Surface waves can make the supports of structures vibrate out-of-phase, giving rise to additional stresses in structures that span large lengths. The modes of vibrations are described in the following section.

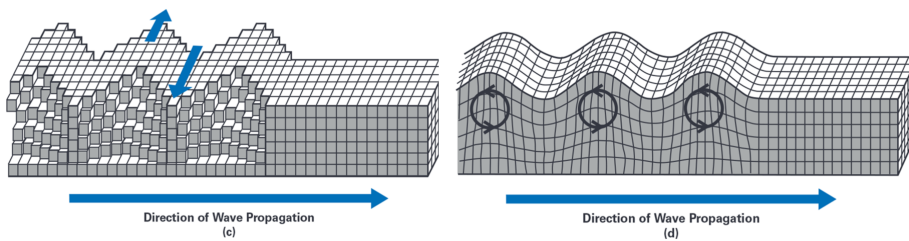


Figure 2.12: Love wave (c) & Rayleigh wave (d) (schematized)

2.2.2 Effects of passing waves on tunnels

The effects of passing surface waves on tunnels can be found by subjecting the supports to harmonic prescribed displacements with a phase shift along the length of the structure. The signal can be a regular sinusoidal wave or a recording of an earthquake. Observing the results in terms of stresses can lead to more insight on the severeness of the phenomenon and the necessity of measures. The direction in which surface waves approach a structure is of interest as well, as it can determine the mode of vibration: a worming mode or snaking mode.

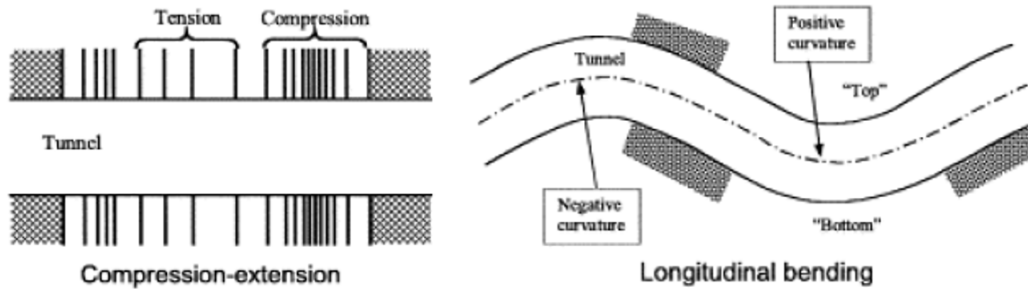


Figure 2.13: Worming (left) and Snaking (right) deformation modes due to passing waves

2.2.2.1 Worming mode (compression)

The worming mode (Figure 2.13, left) occurs when a Rayleigh wave (surface P-wave) approaches a slender structure parallel to its longitudinal axis ($\theta = 0^\circ$). It causes the soil surrounding the structure to alternately be compressed and extended in the direction of wave propagation. This effect is named “worming”, after the similarities with the movements of a worm.

Love waves (surface S-waves), can also provoke tension and compression in axial direction if they approach the structure in an angle θ where it holds that: $0 < \theta < 90^\circ$, where $\theta = 45^\circ$ causes the largest axial deformations.

2.2.2.2 Snaking mode (bending)

The snaking modes (Figure 2.13, right) occur when a Love wave approaches a slender structure parallel to its longitudinal axis ($\theta = 0^\circ$). The shearing effect of the wave makes the structure deform in transverse direction creating an S-shaped deformation pattern. This pattern can arise both vertically (SV-waves) and horizontally (SH-waves), depending on the shape of the approaching wave front.

The snaking effect can cause large rotations at the element joints, leading to possible openings between land tunnel elements. The SFT elements are connected monolithically, so for them the snaking effect can result in large tensile stresses due to bending.

2.3 Soil-structure interaction

For infra structures, traditionally system boundaries were defined at foundation level, so foundations and soil-foundation-interaction are not included in the dynamical model. Until approximately 40 years ago, this was believed to give conservative results, as wave energy is able to travel away from the structure through radiation damping. Also, in static analysis more flexibility from the soil system would often lead to a decrease of internal stresses. Later it was realized that this assumption can lead to considerable underestimations of the structures dynamic response. Thus, in projects where the lives of many are at stake, such as large infrastructural projects or nuclear and chemical plants, it has become more customary to expand the system boundaries and include SSI.

When ground motions are unhindered by the presence of structures, they are called free-field surface motions. The free-field waves then make up the entire wave field at the ground surface. In the seismic analysis of a structure founded on rock, the motion experienced by the base is essentially identical to that occurring in the same point before the structure is built (Wolf 1985). In that case the choice for a fixed base boundary condition is well founded. However, in the case of a soft site, two problems arise for this assumption:

1. The seismic input motion is derived for a free-field surface motion, but, the presence of a structure resting on or inside a soil will **alter the free-field ground motion** to some other (unknown) seismic input (Tsouvalas, 2020).
2. The flexibility of the soil attenuates from the assumption that the structures base is fixed. The structure will interact with the surrounding soil, leading to a further **change of the seismic ground motion and a change in dynamic properties of the structure**. The effect is usually an elongation of the fundamental structural period and increased energy dissipation due to radiation of waves into soil during the structural vibrations.

In engineering practice it is still often believed that the effects of SSI are favourable for the structures seismic performance, but these beliefs are not always justified. First, because a shift of the structural natural frequencies towards the frequencies that are most present in earthquakes. This can lead to larger displacements and internal forces. Second, in modern design codes displacement based methods are included, which limit the structures maximum displacements. The assumption of a rigid base may lead to underestimations of the maximum displacements, and thus be unconservative. Third, for complex dynamic systems it is impossible to know the actual structural response without modelling the soil and finally, engineers might fail to notice soil amplification effects which can have dreadful consequences.

2.3.1 Single DOF spring models

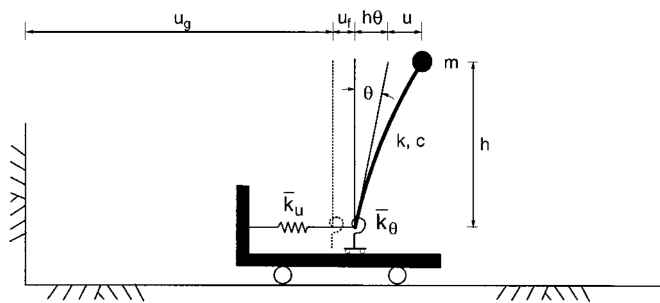


Figure 2.14: Single DOF model (Stewart et al., 1999)

Slender structures above ground level can generally be modelled using a simplified method of analysis. These structures can be schematized as a single degree-of-freedom (DOF) system on a flexible foundation consisting of a rotational and translational stiffness, as can for example be seen in Figure 2.14. The model is applicable to single story buildings that can be represented by a single DOF, or multi story structures where their dynamic behavior is dominated by its fundamental mode. The rotational and translational stiffness of the springs is described in the form of impedance functions. Descriptions of analytical solutions to these impedance functions can

be found in literature for various shapes of foundations and soil types, such as described by Luco & Johnson (Luco & Johnson, 1980).

2.3.2 Distributed spring models

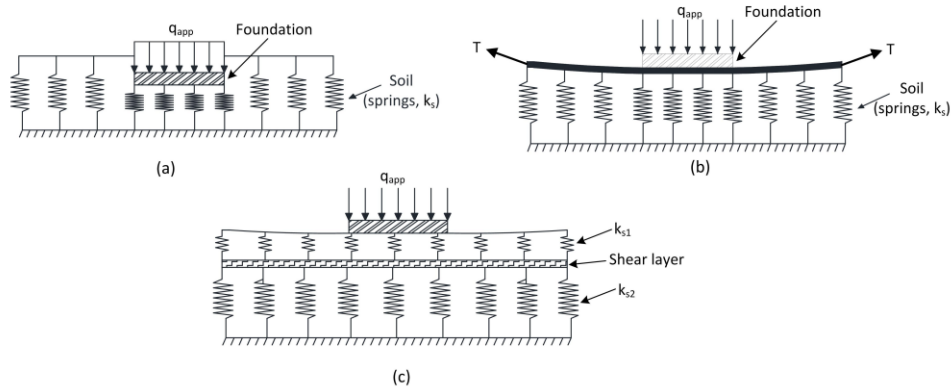


Figure 2.15: Winkler (a), Filonenko-Borodich (b) & Pasternak foundations (c)

Structures buried in soil or rock, such as tunnels, can in general not be modelled using the single DOF models mentioned in the previous section. In the past century, researchers have proposed models to describe the interaction for beams on elastic mediums. The first model was proposed by Winkler as a beam supported by independent springs. It is described by the following adapted Euler-Bernoulli beam equation:

$$EI_{beam} \cdot \frac{d^4 w_z}{dx^4} + k_s w_z = q \quad (2.5)$$

The original solution of the Winkler foundation assumes that the closely spaced springs of the foundation are completely independent of each other and there is no continuity in the foundation due to the lack of interaction between the springs (as can be seen in Figure 2.15a, (Haji, 2017)).

Later improvements on these foundation have been made by Filonenko-Borodich by connecting the tops of the springs to an elastic membrane under a tension force, to add shear interaction between springs (see Figure 2.15 b, (Haji, 2017)). The effect however was dependent of the fictitious tensile force, which is case dependent and based on experiments. Another model was introduced by Pasternak where shear interaction between the springs was created by adding a shear beam. Later he improved his model by adding an extra layer of springs on top of the shear beam (see Figure 2.15 c, (Haji, 2017))

In all 3 aforementioned distributed spring models the effect of damping through wave radiation and the frequency dependent stiffness of the soil is not accounted for. For structures that can be modelled as "infinitely long", such as railway tracks, the soil stiffness can be approximated by a constant value. But for SFTs this is not the case. Firstly, since the soil height on top of the SFT increases inland, which creates a higher (unsymmetrical) soil stiffness, and secondly, the hydrodynamic damping created by the water is of a greater influence near the transition structure. Therefore, a method should be found which can account for these effects.

2.3.3 Substructuring approach

Of all options structural and geotechnical engineers have, the direct interaction analysis (FE-model with full soil-structure domain modelled), would give the most accurate results when modelling SSI. This however still is very time consuming and not suitable for most designs. The alternative approach, employing a substructure system in which the foundation is modelled by a condensed foundation stiffness matrix and mass matrix along with equivalent forcing function represented by the kinematic motion, is more attractive. (Pecker, 2015). For linear systems the direct approach and the substructure approach are equivalent (Wolf, 1985). The approach ensures that the problem becomes better manageable as the system is split up at the soil-structure boundary and a clear distinction is made between the role of the geotechnical and structural engineer.

The soil domain is limited by a fictitious exterior boundary, which is placed so far away from the structure that during the total earthquake excitation, the waves generated along the structure-soil interface do not reach it (Wolf, 1985). At the exterior boundary a radiation boundary condition should be used. This allows outgoing waves to leave the modelling domain with minimal reflections (Comsol).

The substructuring approach is based on the principle of linear superposition, thus linear soil and structural behavior are most appropriate. Obviously, soil can behave in a non-linear way. In that case the stiffness matrix can be found by means of a (non-linear) pushover analysis and a linearization at the expected displacement amplitude of the soil-structure interface (Pecker, 2015). According to Eurocode 8, one may also choose for reduced soil properties to be used in the impedance matrix. These adaptations are only valid when the non-linearities do not significantly alter the seismic response. These effects are of importance for pile foundations, but for buried structures such as tunnels the effects are manageable. Therefore linear-elastic material properties are assumed in this thesis and a more straightforward manner to obtain the dynamic impedances at the foundation level is applied: a frequency domain finite element model.

Steps of the Substructuring Approach:

1. Determine the free field input motion such that the prescribed displacements at the soil-structure boundary are known. To do so, the kinematic interaction motion of the system must be accessed while the mass of the structure is set equal to zero. This can be done using a 1D, 2D or 3D site response analysis, in ascending order of complexity.
2. Compute the dynamic impedances at the foundation level. These impedances represent the frequency dependent stiffness of the soil-tunnel internal boundary: a unit harmonic force applied at location a creates a displacement at location b . The dynamic stiffness $k_{ab,ij}$ can be calculated for loading location $a = 1, 2, 3, \dots, n_{elems}$, displacement location $b = 1, 2, 3, \dots, n_{elems}$ which are the locations of the nodes in the land tunnel, and in directions $i, j = x, y, z$.

$$k_{ab,ij}(\omega) = \frac{F_{a,i}(\omega)}{u_{b,j}(\omega)} \quad (2.6)$$

Since the forces are all unit loads, $F_{a,i}(\omega) = 1$ for all values of a and i . The stiffness $k_{ab,ij}$ can be found for the column related to node b in direction j as:

$$\mathbf{k}_{b,j}(\omega) = \begin{bmatrix} u_{a=1,i=x}^{-1} & u_{a=1,i=y}^{-1} & u_{a=1,i=z}^{-1} & u_{a=2,i=x}^{-1} & \dots \\ u_{a=n-1,i=z}^{-1} & u_{a=n,i=x}^{-1} & u_{a=n,i=y}^{-1} & u_{a=n,i=z}^{-1} \end{bmatrix}^T \quad (2.7)$$

This can be done column by column, to obtain the full bedding stiffness matrix:

$$\mathbf{K}_{\text{bedding}}(\omega) = [\mathbf{k}_{b=1}, \mathbf{k}_{b=2}, \dots, \mathbf{k}_{b=n-1}, \mathbf{k}_{b=n}] \quad (2.8)$$

3. Analyse the dynamic response of the structure supported by the dynamic impedances and subjected to the derived free field input motion.

2.4 Fluid-structure interaction

2.4.1 Morison's equation

The motion of a vibrating body in water has an increased inertia and is damped by a force proportional to the square of the body's velocity [3]. The increased inertia (also called "added mass") can be interpreted as if it would take twice the force to increase the body's velocity with 1 m/s in water, as that it would in a vacuum.

The force can be described using Morison's equation for the in-line force on a body in oscillatory flow. It is the sum of two components: an inertia force acting in-phase with the flow's acceleration and a drag force proportional to the (signed) square of the flow velocity. The inertia force results from the potential theory of oscillating flows, while the drag force originates from the force that acts on a body in a steady flow.

The damping force for moving bodies in still water subjected to earthquakes can be estimated using the adapted Morison equation (Martire, Faggiano, Mazzolani, Zollo, & Stabile, 2010):

$$F_{\text{morison}}(t) = F_{\text{inertia}}(t) + F_{\text{drag}}(t) \quad (2.9)$$

$$F_{\text{morison}}(t) = (C_M - 1) \rho_w A_{\text{displ}} \left(-\frac{\partial^2 u_w}{\partial t^2} + \frac{\partial^2 u_b}{\partial t^2} \right) + \frac{1}{2} \rho_w D \bar{C}_D \left(-\frac{\partial u_w}{\partial t} + \frac{\partial u_b}{\partial t} \right) \left| -\frac{\partial u_w}{\partial t} + \frac{\partial u_b}{\partial t} \right| \quad (2.10)$$

Where u_b is the displacement of the body, u_w the displacement of the water, ρ_w is the water mass density, A the tunnel cross-sectional area, D is the tunnel outer diameter, C_D the drag coefficient and C_M the added mass (or inertia) coefficient. For submerged cylindrical structures the recommended values for C_D and C_M are: $C_D = 1$ and $C_M = 2$ (Journée & Massie, 2001).

As mentioned in the scope of the thesis, water current is not taken into account, thus

$$\frac{\partial u_w}{\partial t} = \frac{\partial^2 u_w}{\partial t^2} = 0. \quad (2.11)$$

This simplifies the equation to:

$$F_{\text{morison}}(t) = (C_M - 1) \rho_w A_{\text{displ}} \frac{\partial^2 u_b}{\partial t^2} + \frac{1}{2} \rho_w D \bar{C}_D \left(\frac{\partial u_b}{\partial t} \right) \left| \frac{\partial u_b}{\partial t} \right| \quad (2.12)$$

As all forces in the described FE-model are linearly proportional to the displacement, velocity and acceleration vector, the drag force in the Morison equation needs to be linearized with respect to the velocity. This is done by Julian Wolfram (Wolfram, 1999) for structures subject to irregular motions (such as earthquakes) in still water. When the water motion and the earthquake motion are both Gaussian random processes, the vibration velocity can be described by a Gaussian process with a zero mean. The drag force can then be found by minimizing the least squares error between the linear and the non-linear drag force as:

$$\bar{C}_D = C_D \frac{\langle v^2 |v| \rangle}{\langle v^2 \rangle} = C_D \frac{\sqrt{(8/\pi)} \sigma_v^3}{\sigma_v^2} = C_D \sqrt{(8/\pi)} \sigma_v \quad (2.13)$$

Here σ_v is the standard deviation of the earthquakes velocity input motion. The full linearized Morison equation then reads:

$$F_{\text{morison}} \approx (C_M - 1) \rho_w A_{\text{displ}} \frac{\partial^2 u_b}{\partial t^2} + \frac{1}{2} \rho_w D C_D \left(\sqrt{\frac{8}{\pi}} \sigma_v \right) \frac{\partial u_b}{\partial t} \quad (2.14)$$

Chapter 3

Methods

In this section, a frequency domain discretized modelling approach is presented to find the response of a SFT to an earthquake. The SFT motion can be found in the nodes by discretizing the structure and refining the mesh at those positions that are most of interest.

The choice was made by the author to use a discretized method, rather than an analytical modeling method, such as the modal analysis. In discretized methods, a solution for displacements and forces is only obtained in specific nodes, defined by the engineer. On the other hand, in analytical (continuous) methods a solution is obtained as a continuous displacement function. This is beneficial if one is interested in obtaining internal forces, as these can simply be found by taking the derivatives of the obtained displacement functions. Damping however, can only be applied proportional to the mass or stiffness. Local damping is not possible for continuous modal analysis. In contrast to analytical methods, discrete methods can account for local damping directly through a damping matrix. For SFTs the influence of local damping at the interface with water, soil, tethers and transition structure, can not be neglected. Thus, a discrete method is more appropriate for this case.

The most common solution method for discrete dynamic systems of equations is numerical time-integration, as applied in many commercial finite element software packages (DIANA, Ansys, Abaqus). Despite it being a very robust method, it gives very little insight in why a structure dynamically behaves as it does. Moreover, it can be very time consuming.

In this thesis it is chosen to use a frequency domain method, rather than an ordinary time integration method for multiple reasons:

1. Frequency domain methods give insight in the frequency contents, present in the forcing signal and their contribution to the dynamic response;
2. Frequency response functions can be obtained for the structure, which describe the sensitivity of a certain DOF to forcing in one or more other DOFs per frequency;
3. The input forces and output displacements can still be defined in terms of time dependent functions, using forward and inverse FFT's;
4. Convergence of the solution occurs while including relatively few frequencies, while for time integration methods many time steps must be included (every 0.001 to 0.005 seconds) to obtain convergence of results. Multiple iteration steps are not necessary for frequency domain methods.
5. In frequency domain methods, the "Substructuring method" can be used, which makes the modeling of the full soil body around the structure superfluous, while still accounting for soil-structure interaction. In this way, the number of DOFs can be drastically be reduced, without paying the price of large inaccuracies due to omitting SSI.

3.1 Assumptions

In the method of choice, several assumptions are made that simplify the problem to its most essential elements. These assumptions make the model suitable for obtaining insight on a high level, combined with a high time efficiency.

3.1.1 Non-linearities

Geometrical non-linearity's have been neglected in this thesis, because small displacements are expected. As long as for vertical displacements δ_z (equation 3.1) and for horizontal displacements δ_h (equation 3.2) the following two inequalities hold, this assumption should be justified:

$$\delta_z \leq \frac{\Delta L_{teth}}{100} \quad (3.1)$$

$$\delta_h \leq \frac{\Delta L_{moor}}{100} \quad (3.2)$$

Here, ΔL_{teth} is the longitudinal distance between tethers and ΔL_{moor} is the longitudinal distance between the mooring lines. In the discussion in Chapter 7 this will be reflected upon.

Material non-linearity's are neglected as well, since the displacements and stresses are checked in SLS. In this limit state no plasticity is allowed, and the stress-strain relations in the structure are linear until after failure. The structural response after failure is not part of the scope of this thesis. In the parameter study in Chapter 6 the structure will be considered failed when plasticity arises.

As material and geometrical non-linearity's are not considered necessary for this preliminary study, a linear-elastic frequency domain analysis is justified to study the structures dynamic response.

3.1.2 Meshsize

The maximum meshsize is found based on a rule-of-thumb that says that the meshsize of a finite element model should be no less than $\frac{1}{8}$ of the minimum wavelength in a structure. This wavelength can be found based on the lowest wave speed in concrete (3000 m/s) and the largest significant frequency expected in the earthquake signals (20 Hz). The minimum wavelength is $\lambda = \frac{v}{f} = \frac{3000}{20} = 150m$. The maximum meshsize of the land tunnel thus yields: $\Delta L_{max} = \frac{\lambda}{8} = 18.75m$. This number will be taken into account when choosing the meshsizes for the land tunnel and SFT in the global model.

3.1.3 Coupling

The coupling between the x, y and z direction through the soil shall be neglected. Later in the parameter study 7.1.4 this assumption will be reflected upon.

3.1.4 Local site response & amplification

Forcing is directly applied at the structures supports, instead of using a local-site response analysis. So amplification due to the soil's dynamic characteristics is not accounted for. Also the earthquake signals will not be scaled to the sites response spectrum.

3.2 Model description

The global model of the SFT and land tunnel is created using rod elements in longitudinal direction (see Figure 3.1, top) and Euler-Bernoulli beam elements in the vertical and horizontal transverse directions (see Figure 3.1, mid and bottom). Here, the SFT is schematized in orange and the land tunnels in blue. The interface conditions between the SFT and land tunnel are schematized as translation spring-dashpots in longitudinal direction and rotational spring-dashpots in transverse directions. The interaction between soil and the land tunnels is modelled using dynamic springs which are frequency dependent and coupled with the neighbouring spring elements in the same direction.

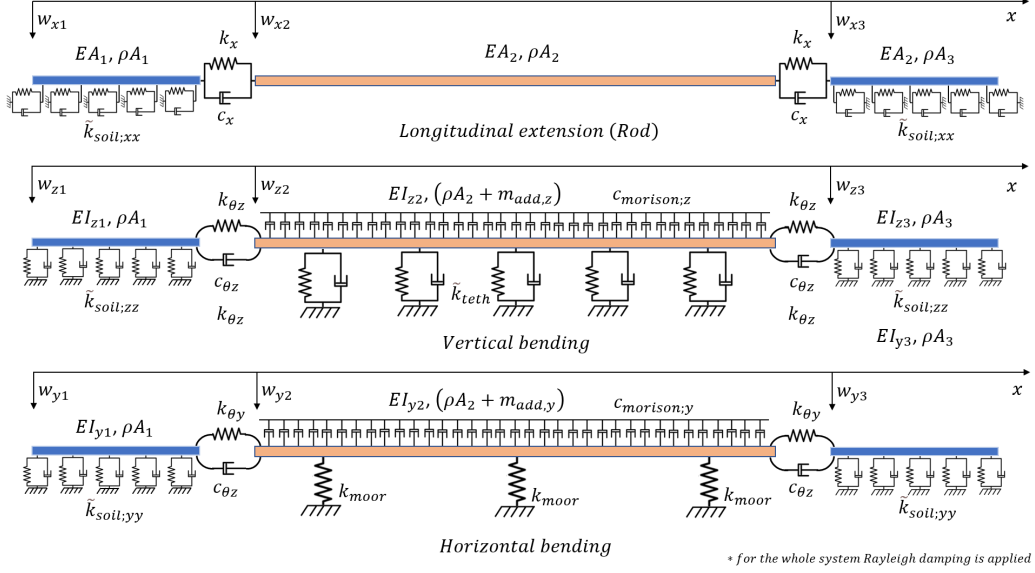


Figure 3.1: Mechanical scheme

3.2.1 Solution method

The main advantage of the method is that when the structure is discretized to a multi-degree of freedom system in the form of:

$$\mathbf{M}\ddot{\mathbf{u}} + \mathbf{C}\dot{\mathbf{u}}(t) + \mathbf{K}\mathbf{u}(t) = \mathbf{f}(t) \quad (3.3)$$

Where \mathbf{M} is the mass matrix, \mathbf{C} is the damping matrix, \mathbf{K} the stiffness matrix, \mathbf{f} the force vector and $\mathbf{u}(t)$ is the displacement vector. Time-derivatives are noted using Newtons notation. The system of equations can be transformed to the frequency domain and rewritten using a dynamic stiffness matrix $\tilde{\mathbf{K}}_{dyn}(\omega)$ and the displacement vector in the frequency domain $\tilde{\mathbf{u}}(\omega)$:

$$(-\omega^2\mathbf{M} + i\mathbf{C} + \mathbf{K})\tilde{\mathbf{u}}(\omega) = \tilde{\mathbf{f}}(\omega) \quad (3.4)$$

$$\tilde{\mathbf{K}}_{dyn}(\omega)\tilde{\mathbf{u}}(\omega) = \tilde{\mathbf{f}}(\omega) \quad (3.5)$$

Using equation 3.5 this system can be solved for the displacement vector $\tilde{\mathbf{u}}(\omega)$ in a single step per frequency. The (element-wise) absolute value of this vector can be interpreted as the amplitude of the steady state solution to a harmonic load with radial frequency ω . The (element-wise) arctangent of the imaginary over the real part of the displacement vector, represents the phase-angle:

$$amplitude = |\tilde{\mathbf{u}}(\omega)| \quad (3.6)$$

$$phase\ angle = Arg(\tilde{\mathbf{u}}(\omega)) \quad (3.7)$$

Most dynamic time-force or time-displacement signals with an arbitrary shape can be described as the sum of a finite number of sine and cosine functions (as done in Fourier Transforms). The

steady-state response of each of the frequency components can be found as described in equation 3.8, and by means of an inverse FFT a solution can be found back in the time domain as:

$$\mathbf{u}(t) = \frac{1}{2\pi} \int_{-\infty}^{\infty} \tilde{\mathbf{u}}(\omega) e^{i\omega t} d\omega \quad (3.8)$$

If one is interested in displacements and internal forces in between nodes, "shape functions" can be used. The shape functions used in this thesis are polynomials of the 3th order with C2 continuity for Euler-Bernoulli beams, and linear shape functions with C0 continuity for the rod elements (see Appendix A). These describe the deformations, while satisfying all the interface conditions. The bending moments and shear forces are found as the (negative) bending stiffness multiplied with respectively the 2th and 3th derivative of the beam shape function with respect to x . Normal forces can be found as the (negative) axial stiffness multiplied with the 1th derivative of the rod shape function with respect to x .

3.3 Global model - SFT & Land tunnel

In the next section the equations of motion and boundary and interface conditions of the global model are presented.

3.3.1 Equations of Motion

The equations of motion are defined for the longitudinal, vertical and horizontal directions. These are described in the form of ordinary differential equations (ODE's) in the frequency domain.

It must be noted that the forcing terms in the RHS of every ODE is only dependent on the stiffness and displacements of the soil in the direction corresponding with the direction of deformation. So, the ODE's of the longitudinal extension rod are only forced in longitudinal direction. The contribution of transverse forcing, through the coupling soil stiffness, is not taken into account, as this contribution is expected to be small.

The input soil displacements $\tilde{W}_g(\omega)$ in the RHS are found by applying a Fourier transform over the ground acceleration signal $a_g(t)$, to transform it from the time to the frequency domain. Then it is divided by $-\omega^2$ to obtain the Fourier displacement spectrum, as described in Equation 3.9.

$$\tilde{W}_g(\omega) = \frac{-\int_{-\infty}^{\infty} a_g(t) e^{-i\omega t} dt}{\omega^2} \quad (3.9)$$

3.3.1.1 Longitudinal extension (rod)

The rod is build up by 3 sections: section 1 and 3 are the land tunnels and section 2 is the SFT. The rod is supported by springs in the xx direction. Forcing is applied through the RHS as the longitudinal dynamic soil stiffness, multiplied with the longitudinal Fourier soil displacement. The Equations of Motion are displayed below, where ρA_i is the cross-sectional weight of section i , EA_i is the extensional stiffness of section i , $\tilde{k}_{soil;xx}$ is the dynamic soil stiffness in x -direction, and \tilde{W}_{xi} is the longitudinal displacement of section i in the frequency domain. $\tilde{W}_{g;x}$ is the longitudinal ground input displacement in the frequency domain.

$$-\rho A_1 \omega^2 \tilde{W}_{x1} + EA_1 \frac{\partial^2 \tilde{W}_{x1}}{\partial x^2} + \tilde{k}_{soil;xx}(\omega, x) \tilde{W}_{x1} = \tilde{k}_{soil;xx}(\omega, x) \tilde{W}_{g;x} \quad (3.10)$$

$(0 \leq x \leq L_{land})$

$$-\rho A_2 \omega^2 \tilde{W}_{x2} + EA_2 \frac{\partial^2 \tilde{W}_{x2}}{\partial x^2} = 0 \quad (3.11)$$

$(L_{land} \leq x \leq L_{land} + L_{sft})$

$$-\rho A_3 \omega^2 \tilde{W}_{x3} + EA_3 \frac{\partial^2 \tilde{W}_{x3}}{\partial x^2} + \tilde{k}_{soil;xx}(\omega, x) \tilde{W}_{x3} = \tilde{k}_{soil;xx}(\omega, x) \tilde{W}_{g;x} \quad (3.12)$$

$(L_{land} + L_{sft} \leq x \leq 2L_{land} + L_{sft})$

3.3.1.2 Vertical bending (beam)

The beams are build up in the same configuration as the rod: section 1 and 3 are the land tunnels and section 2 is the SFT. Forcing is applied through the RHS as the vertical dynamic soil stiffness, multiplied with the vertical Fourier soil displacement. The Equations of Motion are displayed below, where ρA_i is the cross-sectional weight of section i , EI_i is the bending stiffness of section i , the stiffness of tether number n is presented as $k_{teth,n}$ with its respective center to center distance in longitudinal direction ΔL_{teth} . $\tilde{k}_{soil;zz}$ is the dynamic soil stiffness in z-direction, and \tilde{W}_{zi} is the vertical displacement of section i in the frequency domain. $\tilde{W}_{g;z}$ is the vertical ground input displacement in the frequency domain.

The SFT section has an extra "added" mass ($m_{add,z}$), as well as a damping term resulting from the hydraulic drag force ($c_{drag,z}$). These originate from the Morison equation and represent the inertia and damping contributions of the water. The tethers are modelled in the form of frequency dependent springs, and these add stiffness to the system in the LHS, but also cause forcing through the RHS, when multiplied with the local Fourier ground displacements.

$$-\omega^2 \rho A_1 \tilde{W}_{z1} + EI_{z1} \frac{\partial^4 \tilde{W}_{z1}}{\partial x^4} + \tilde{k}_{soil;zz}(\omega, x) \tilde{W}_{z1} = \tilde{k}_{soil;zz}(\omega, x) \tilde{W}_{g;z} \quad (3.13)$$

$$(0 \leq x \leq L_{land})$$

$$-\omega^2 (\rho A_2 + m_{add,z}) \tilde{W}_{z2} + EI_{z2} \frac{\partial^4 \tilde{W}_{z2}}{\partial x^4} + i\omega c_{D,z} \tilde{W}_{z2} \quad (3.14)$$

$$+ \sum_{n=1}^{n_{teth}} \delta(x - L_{sft} - n\Delta L_{teth}) \tilde{k}_{teth,n}(\omega) \tilde{W}_{z2}$$

$$= \sum_{n=1}^{n_{teth}} \delta(x - L_{sft} - n\Delta L_{teth}) \tilde{k}_{teth}(\omega) \tilde{W}_{g;z} \quad (L_{land} \leq x \leq L_{land} + L_{sft})$$

$$-\omega^2 \rho A_3 \tilde{W}_{z3} + EI_{z3} \frac{\partial^4 \tilde{W}_{z3}}{\partial x^4} + \tilde{k}_{soil;zz}(\omega, x) \tilde{W}_{z3} = \tilde{k}_{soil;zz}(\omega, x) \tilde{W}_{g;z} \quad (3.15)$$

$$(L_{land} + L_{sft} \leq x \leq 2L_{land} + L_{sft})$$

3.3.1.3 Horizontal bending (beam)

At last, the horizontal beam is supported by springs in the yy direction. Forcing is applied through the RHS as the horizontal (transverse) dynamic soil stiffness, multiplied with the horizontal Fourier soil displacement. The Equations of Motion are displayed below, where ρA_i is the cross-sectional weight of section i , $EI_{y,i}$ is the horizontal bending stiffness of section i , $\tilde{k}_{soil;yy}$ is the dynamic soil stiffness in y-direction, and \tilde{W}_{yi} is the horizontal displacement of section i in the frequency domain. $\tilde{W}_{g;y}$ is the horizontal ground input displacement in the frequency domain.

The added mass and drag coefficients are present in the ODE's as well, although these have different values. This are caused by a different cross sectional diameter in the horizontal plane, resulting in other coefficients through the Morison equation.

The mooring lines are modelled in the form of regular springs (not dependent on radial frequency). These add stiffness to the system in the LHS and forcing through the RHS, in a similar fashion as for the tethers in the vertical bending beam. The mooring lines are oriented inclined in a 45° angle with the horizontal plane. Therefore the derived mooring line stiffness in 3.6 must be divided by $\sqrt{2}$. The stiffness of mooring line number n is presented as $k_{moor,n}$ with the respective center to center distance in longitudinal direction ΔL_{moor} .

$$-\omega^2 \rho A_1 \tilde{W}_{y1} + EI_{y1} \frac{\partial^4 \tilde{W}_{y1}}{\partial x^4} + \tilde{k}_{soil;yy}(\omega, x) \tilde{W}_{y1} = \tilde{k}_{soil;yy}(\omega, x) \tilde{W}_{g;y} \quad (3.16)$$

$$(0 \leq x \leq L_{land})$$

$$-\omega^2 (\rho A_2 + m_{add,y}) \tilde{W}_{y2} + EI_{y2} \frac{\partial^4 \tilde{W}_{y2}}{\partial x^4} + i\omega c_{D,y} \tilde{W}_{y2} +$$

$$\sum_{n=1}^{n_{moor}} \delta(x - L_{sft} - n\Delta L_{moor}) k_{moor,n} \tilde{W}_{y2} = 0 \quad (L_{land} \leq x \leq L_{land} + L_{sft})$$

$$\begin{aligned}
-\omega^2 \rho A_3 \tilde{W}_{y3} + EI_{y3} \frac{\partial^4 \tilde{W}_{y3}}{\partial x^4} + \tilde{k}_{\text{soil};yy}(\omega, x) \tilde{W}_{a3} &= \tilde{k}_{\text{soil};yy}(\omega, x) \tilde{W}_{g;y} \\
(L_{\text{land}} + L_{\text{sft}} \leq x \leq 2L_{\text{land}} + L_{\text{sft}}) &
\end{aligned} \tag{3.18}$$

3.3.2 Boundary & Interface conditions

The boundary conditions describe the displacements at the outer edges of the left and right land tunnel, while the interface conditions describe the relation between forces and displacements at the two transition structures.

The boundary conditions of the land tunnels are chosen such that the displacements of the boundary nodes are equal to the displacements of the surrounding soil. It is chosen this way, because those displacements can still influence the transition structure, and zero displacements would be unrealistic during the occurrence of an earthquake. Rotations at the outer edges are set equal to zero.

The interface conditions are defined to have equal translations in respectively y and z direction. Translations in x direction are related through a translation spring-dashpot interface element, where k_x is the longitudinal end-joint translation spring stiffness and c_x is the end-joint damping constant in the same direction. Vertical and horizontal rotations are connected through rotational spring-dashpot interfaces, where $k\theta_z$ and $k\theta_y$ are the vertical and horizontal end-joint rotation stiffnesses and $c\theta_z$ and $c\theta_y$ are the vertical and horizontal end-joint damping constants.

The boundary and interface conditions are described more elaborately below:

3.3.2.1 Longitudinal Boundary & Interface conditions

$$\begin{aligned}
BC1_x &: \tilde{W}_{x1} &= \tilde{W}_{g;x} & (x = 0) \\
IC1_x &: EA_1 \frac{\partial \tilde{W}_{x1}}{\partial x} - EA_2 \frac{\partial \tilde{W}_{x2}}{\partial x} &= (k_x + i\omega c_x) (\tilde{W}_{x1} - \tilde{W}_{x2}) & (x = L_{\text{land}}) \\
IC2_x &: EA_2 \frac{\partial \tilde{W}_{x2}}{\partial x} - EA_3 \frac{\partial \tilde{W}_{x3}}{\partial x} &= (k_x + i\omega c_x) (\tilde{W}_{x2} - \tilde{W}_{x3}) & (x = L_{\text{land}} + L_{\text{sft}}) \\
BC2_x &: \tilde{W}_{x3} &= \tilde{W}_{g;x} & (x = 2L_{\text{land}} + L_{\text{sft}})
\end{aligned} \tag{3.19}$$

3.3.2.2 Vertical Boundary & Interface conditions

$$\begin{aligned}
BC1_z &: \frac{\partial \tilde{W}_{z1}}{\partial x} &= 0 & (x = 0) \\
BC2_z &: \tilde{W}_{z1} &= \tilde{W}_{g;z} & (x = 0) \\
IC1_z &: \tilde{W}_{z1} &= \tilde{W}_{z2} & (x = L_{\text{land}}) \\
IC2_z &: EI_{z1} \frac{\partial^2 \tilde{W}_{z1}}{\partial x^2} - EI_{z2} \frac{\partial^2 \tilde{W}_{z2}}{\partial x^2} &= (k_{\theta z} + i\omega c_{\theta z}) \left(\frac{\partial \tilde{W}_{z1}}{\partial x} - \frac{\partial \tilde{W}_{z2}}{\partial x} \right) & (x = L_{\text{land}}) \\
IC3_z &: \tilde{W}_{z2} &= \tilde{W}_{z3} & (x = L_{\text{land}} + L_{\text{sft}}) \\
IC4_z &: \left(EI_{z2} \frac{\partial^2 \tilde{W}_{z2}}{\partial x^2} - EI_{z3} \frac{\partial^2 \tilde{W}_{z3}}{\partial x^2} \right) &= (k_{\theta z} + i\omega c_{\theta z}) \left(\frac{\partial \tilde{W}_{z2}}{\partial x} - \frac{\partial \tilde{W}_{z3}}{\partial x} \right) & (x = L_{\text{land}} + L_{\text{sft}}) \\
BC3_z &: \frac{\partial \tilde{W}_{z3}}{\partial x} &= 0 & (x = 2L_{\text{land}} + L_{\text{sft}}) \\
BC4_z &: \tilde{W}_{z3} &= \tilde{W}_{g;z} & (x = 2L_{\text{land}} + L_{\text{sft}})
\end{aligned} \tag{3.20}$$

3.3.2.3 Horizontal Boundary & Interface conditions

$$\begin{aligned}
BC1_y & : \quad \frac{\partial \tilde{W}_{y1}}{\partial x} = 0 & (x = 0) \\
BC2_y & : \quad \tilde{W}_{y1} = \tilde{W}_{g;y} & (x = 0) \\
IC1_y & : \quad \tilde{W}_{y1} = \tilde{W}_{y2} & (x = L_{land}) \\
IC2_y & : \quad \left(EI_{y1} \frac{\partial^2 \tilde{W}_{y1}}{\partial x^2} - EI_{y2} \frac{\partial^2 \tilde{W}_{y2}}{\partial x^2} \right) = (k_{\theta y} + i\omega c_{\theta y}) \left(\frac{\partial \tilde{W}_{y1}}{\partial x} - \frac{\partial \tilde{W}_{y2}}{\partial x} \right) & (x = L_{land}) \\
IC3_y & : \quad \tilde{W}_{y2} = \tilde{W}_{y3} & (x = L_{land} + L_{sft}) \\
IC4_y & : \quad \left(EI_{y2} \frac{\partial^2 \tilde{W}_{y2}}{\partial x^2} - EI_{y3} \frac{\partial^2 \tilde{W}_{y3}}{\partial x^2} \right) = (k_{\theta y} + i\omega c_{\theta y}) \left(\frac{\partial \tilde{W}_{y2}}{\partial x} - \frac{\partial \tilde{W}_{y3}}{\partial x} \right) & (x = L_{land} + L_{sft}) \\
BC3_y & : \quad \frac{\partial \tilde{W}_{y3}}{\partial x} = 0 & (x = 2L_{land} + L_{sft}) \\
BC4_y & : \quad \tilde{W}_{y3} = \tilde{W}_{g;y} & (x = 2L_{land} + L_{sft})
\end{aligned} \tag{3.21}$$

3.4 Local model 1 - Tethers

The dynamic behavior of the steel tethers is modelled through a local sub-model. Here the tethers are represented by tension rods to derive their frequency dependent stiffness. This stiffness is derived for every tether and later substituted into the global model. The stiffness only has to be derived once, after which it can be inserted as a linear (frequency dependent) spring in the model. This will reduce the number of DOFs needed for the global model.

In the local model the tether is free at node 1 and connected rigidly at node n+1. A unit load in the frequency domain is applied at node 1, representing the SFT moving in vertical harmonic motion.

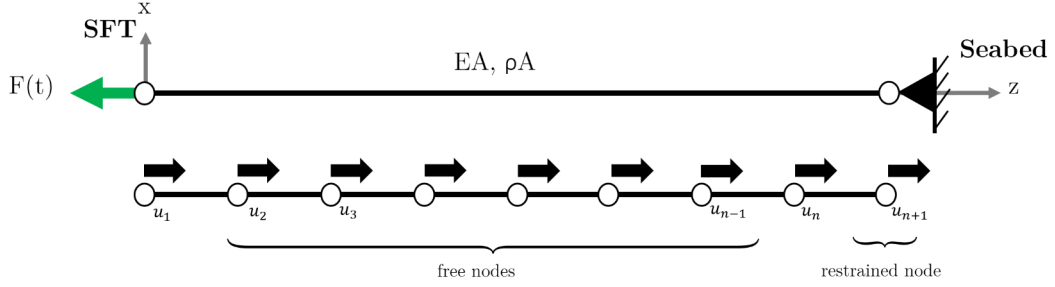


Figure 3.2: Tether discretization

$$\mathbf{k}_e = \frac{EA}{h} \begin{bmatrix} 1 & -1 \\ -1 & 1 \end{bmatrix}; \quad \mathbf{m}_e^{\text{cons}} = \frac{\rho_s A_t h}{6} \begin{bmatrix} 2 & 1 \\ 1 & 2 \end{bmatrix}; \quad \mathbf{c}_e = \alpha_R \mathbf{k}_e + \beta_R \mathbf{m}_e^{\text{cons}} \quad (3.22)$$

The element stiffness matrix \mathbf{k}_e , damping matrix \mathbf{c}_e and mass matrix $\mathbf{m}_e^{\text{cons}}$ are used as derived in A for a rod and assembled to the global stiffness, damping and mass matrices of size: $(n+1) \times (n+1)$ for a bar with n elements and n+1 nodes. As node n+1 is restrained, column and row n+1 can be removed from the system and a system of size $n \times n$ is obtained:

$$-\omega^2 \mathbf{M} \tilde{\mathbf{u}} + i\omega \mathbf{C} \tilde{\mathbf{u}} + \mathbf{K} \tilde{\mathbf{u}} = \mathbf{f}(\omega) \quad (3.23)$$

$$\mathbf{f}(\omega) = [1 \ 0 \ 0 \ \dots \ 0 \ 0]^T \quad (3.24)$$

This system can be solved in the frequency domain as:

$$\begin{aligned} \tilde{\mathbf{K}}_{\text{dyn}} &= -\omega^2 \mathbf{M} + i\omega \mathbf{C} + \mathbf{K} \\ \tilde{\mathbf{f}}(\omega_f) &= [1 \ 0 \ 0 \ \dots \ 0 \ 0]^T \\ \tilde{\mathbf{U}}(\omega) &= \tilde{\mathbf{K}}_{\text{dyn}}^{-1} \tilde{\mathbf{f}}(\omega_f = \omega); \\ k_{\text{teth}}(\omega) &= \frac{\tilde{\mathbf{f}}[1]}{\tilde{\mathbf{U}}(\omega)[1]} = \frac{\tilde{\mathbf{f}}[1]}{\tilde{\mathbf{K}}_{\text{dyn}}^{-1}[1, 1]} = \frac{1}{\tilde{\mathbf{K}}_{\text{dyn}}^{-1}[1, 1]} \end{aligned} \quad (3.25)$$

Resulting in a solution for the tether stiffness k_{tether} in the frequency domain, where [1] indicates the first index of a vector and [1, 1] The top left index of a matrix.

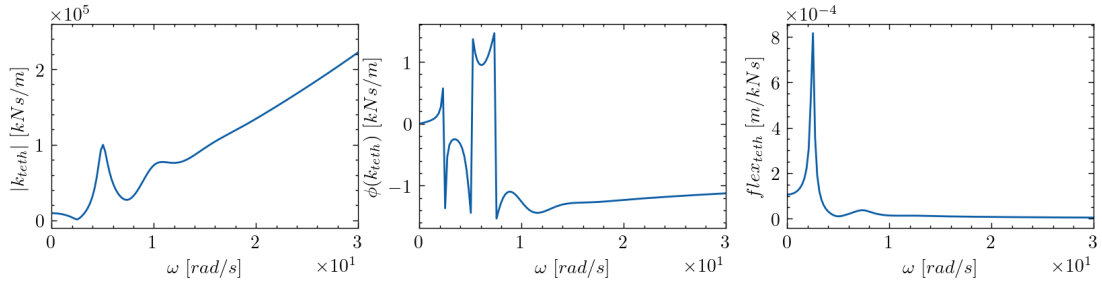


Figure 3.3: Absolute tether stiffness, phase angle and flexibility

For Young's modulus $E = 2 \cdot 10^7 \frac{kN}{m^2}$, cross-sectional area $A = 0.472m^2$, specific weight $\rho_s = 8.002 \frac{ton}{m^3}$ and Rayleigh damping coefficients $\alpha_R = 0.400$ & $\beta_R = 0.004$, the absolute stiffness $|k_{\text{teth}}|$, phase angle ϕ and flexibility are as displayed in Figure 3.3.

3.5 Local model 2 - Soil

To find the dynamic bedding stiffness of the soil around the land tunnel, a substructuring method is applied using the finite element software Comsol Multiphysics. The result is a second local model that computes the values for the bedding stiffness matrix of the land tunnel. Later the bedding matrix is imported into the global model to create an elastic foundation at the land tunnel DOFs.

The advantage of using Comsol in comparison to other FE-software, is that it allows for modelling the hydraulic part of the local model with equal rigor as the soil and structural elements. Next, it is also capable of solving the system of equations in the frequency domain, which is a requirement to be compatible with the method of this thesis.

3.5.1 Comsol model

The soil, rock, tunnel and water components are setup in the Comsol environment as visualised in Figures 3.4 and 3.5 below. The geometrical properties are listed in Table 3.1 and material and cross-sectional properties can be found in the case study in Chapter 5. The cross-section of the land tunnel and SFT are assumed similar and are simplified by not accounting for any internal walls, floors and emergency corridors (which cross-connects the two tubes). Therefore the moment of inertia and cross-sectional area are slightly underestimated, although the influences of these elements are small.

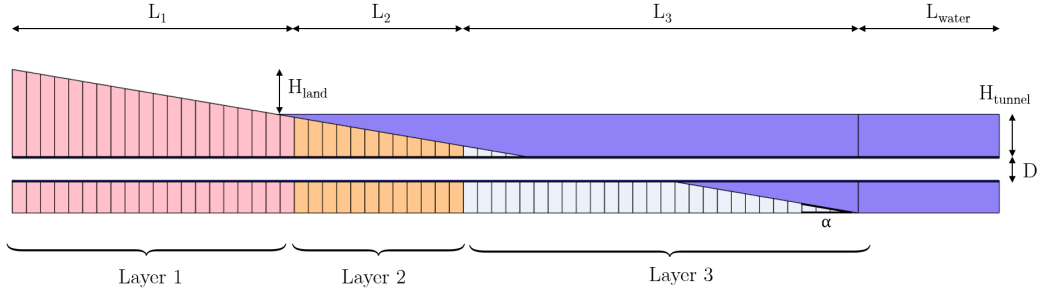


Figure 3.4: Soil-structure interaction model

Parameter	Value		Parameter	Value	
Total			Water		
Width	B	200 [m]	Water height	H_{water}	70 [m]
			Water length	L_{water}	100 [m]
Land			Tunnel		
Land maximum height	H_{land}	35 [m]	Tunnel diameter	D	18 [m]
Length layer 1 (claystone)	L_1	200 [m]	Tunnel length	L_{tunnel}	700 [m]
Length layer 2 (clay)	L_2	120 [m]	Tunnel top depth	H_{tunnel}	30 [m]
Length layer 3 (artificial filling)	L_3	280 [m]	Tunnel outer wall thickness	t_{wall}	1.15 [m]
Slope	α	9.63 [°]	Center to center distance	Δ_L	40 [m]

Table 3.1: Geometrical properties of local model 2

The soil and tunnel are created as solid mechanics elements, whereas water is defined using pressure acoustics elements. The solid mechanics elements are intended for general structural analysis of 3D, 2D, or axisymmetric bodies. The pressure acoustics elements, on the other hand, are used to compute the pressure variations for the propagation of acoustic waves in fluids at quiescent background conditions (*Comsol Documentation, 2022*). In Comsol both element types can be used in the same model, by creating "multiphysics acoustic-structure boundaries" at the interfaces.

3.5.2 Boundary conditions

Boundary conditions are established as indicated in Figure 3.5 below. At the water surface the pressure acoustics elements are given "free" boundary conditions, in Comsol named "sound soft boundary". The boundaries that in reality would be an interface with another water body, are setup as "infinity-boundaries", in Comsol named "cylindrical wave radiation boundary". It adds a radiation boundary condition for a cylindrical wave, which allows an outgoing cylindrical wave to leave the modeling domain with minimal reflections. The soil, rock and tunnel elements that would in reality have interfaces with other solid mechanics elements have "infinity-boundaries" as well, in Comsol named "low reflecting boundary". It is used to let waves pass out from the model without reflection. By default, it takes material data from the domain in an attempt to create a perfect impedance match for both pressure waves and shear waves (*Comsol Documentation, 2022*).

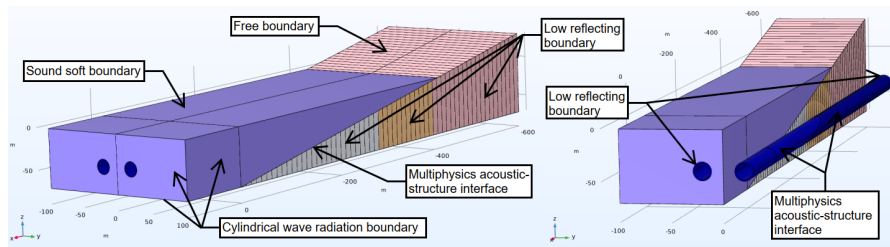


Figure 3.5: Comsol boundary & interface conditions

3.5.3 Loading

Loadig is applied in the form of a unit harmonic load of 1 kN, distributed equally over the length of "load application lines" (see Figure 3.6). This harmonic load is applied separately in x, y and z direction and at radial frequencies of $\omega = 2.5, 5.0, 7.5, \dots, 50.0 \text{ rad/s}$. Using a parametric sweep in Comsol, the system is solved for a set of 25 different locations for the load application lines. The location is altered by stepwise shifting the lines land inward (along the x-axis) with 25 steps of 10 meter each. It is done in 25 steps, because in the global model it is chosen to devide the land tunnels in 25 separated nodes.

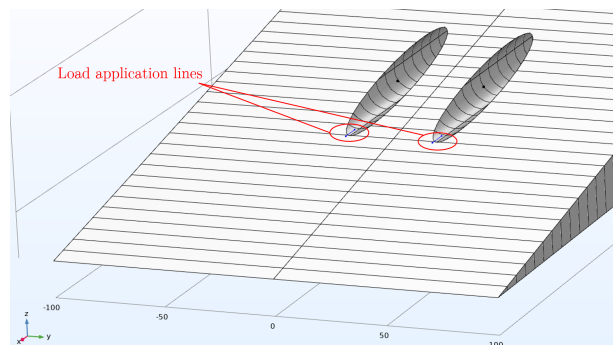


Figure 3.6: Load application lines

3.5.4 Bedding matrix assembly

When the system is solved for all 25 load locations, with unit force in direction x, y and z separately, and at each location for all 20 different values of ω , the bedding matrix can be assembled as described in subsection 2.3.3.

3.6 Mooring lines

Mooring lines are attached to the SFT to secure its position in horizontal transverse direction, as currents would otherwise make the tube deform too much. They can only transfer tensile forces, as the diagonal lines will slack when loaded in compression. Hence, only the lines in tension are actively keeping the SFT in place. At the seabed a gravity structure or pile foundation can be constructed to transfer the tensile mooring forces.

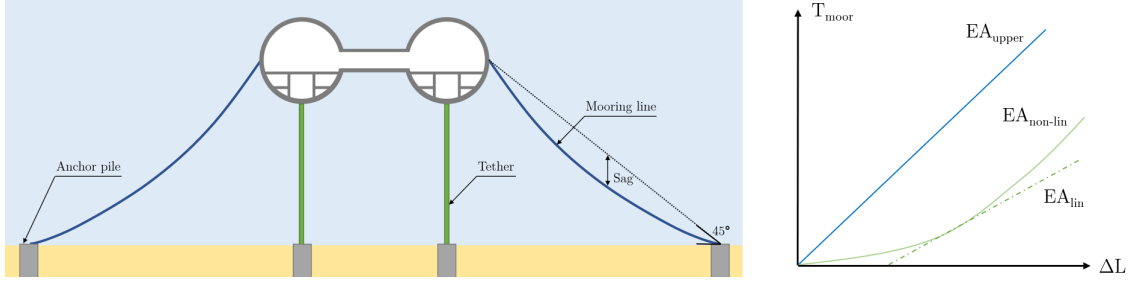


Figure 3.7: Mooring lines schematized (left) & Non-linear force-elongation relationship (right)

In an undeformed state, the mooring lines are not in tension and only loaded by their self weight acting downward. This will cause the lines to sag and have a stiffness that deviates from that of normal straight lines or rods. When loaded in tension the sag will decrease, while compression will increase the sagging of the mooring lines. The stiffness can be described by a non-linear force-displacement relationship, where the force increases exponentially with the displacement. For this stiffness to be implemented in the global model, a linearization around its neutral position is needed. This can be done using the relationship described by Peters (Peters, 1993) in equation 3.26.

$$EA_{lin} = \frac{EA}{1 + EA \frac{(gl)^2(T_i + T_j)}{24T_i^2 T_j^2}} \quad (3.26)$$

In this formula, the cross-sectional area is assumed as $A_{moor} = 0.10m^2$, The young's modulus of steel is $E_s = 2 \times 10^8 kN/m^2$ and the gravitational acceleration is $g = 9.81m/s^2$. The upper bound tensile force T_j and lower bound tensile force T_i must be estimated when the range is unknown. The average tensile force is known from the self weight of the mooring lines, thus an estimation can be made of the deviations from this average.

$$T_i = \sqrt{2}\rho Agl - \Delta T_{mooring}; T_j = \sqrt{2}\rho Agl + \Delta T_{mooring} \quad (3.27)$$

The length of the mooring line is increased due to the sag f , and can be calculated using equation 3.28:

$$l_{sag} = l \left(1 + \frac{3}{8} \left(\frac{f}{l} \right)^2 \right) \quad (3.28)$$

$$f = \frac{gl^2}{8T} \quad (3.29)$$

The linearized mooring line stiffness is then obtained as:

$$k_{moor} = \frac{EA_{lin}}{l_{sag}} \quad (3.30)$$

This mooring stiffness is working diagonally in the y-z plane, while in the the global model the mooring line stiffness only acts in horizontal direction (y) on the SFT. It is chosen to not account for the vertical mooring stiffness, as its stiffness is a fraction (0.01-0.1%) of the stiffness the tethers add to the system. The horizontal stiffness can be found as:

$$k_{moor,y} = \frac{k_{moor}}{\sqrt{2}} \quad (3.31)$$

3.7 Python code

The method described in this chapter is applied in a numerical model using the programming language Python. The structure of the Python code has been schematized in the flow chart below in Figure 3.8. It describes the flow of data through the global model, and how the relations are determined between Comsol Submodel 1, the Tether Submodel 2 and the global model. After the calculations in the global model, post-processing of the displacements leads to internal forces and stresses. These results are visualized by means of various types of graphs, surface plots and movies.

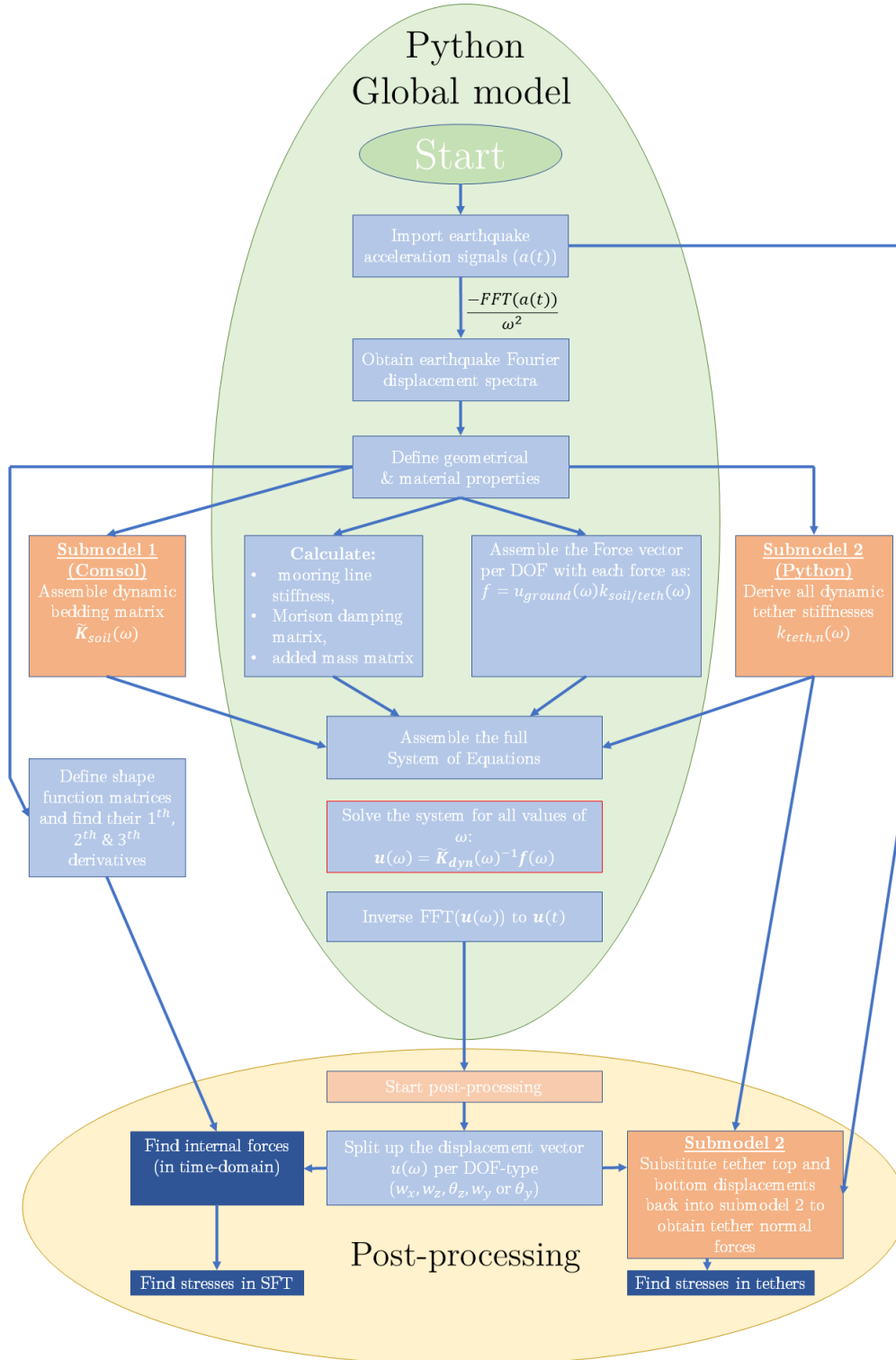


Figure 3.8: Flow chart of the Python code

Chapter 4

Validation of the model

In this chapter the model is validated using a finite element software (DIANA). A replica of the structure is created to compare their dynamic behaviors and other characteristics. Using this approach various signals can be applied and system parameters can be tweaked to create more insight. It was chosen not to do this based on previous SFT related research, as small deviations in modeling choices can cause large differences in results for structural dynamics.

The main difference between the DIANA and the Python model is that DIANA solves the system of equations using a regular Newton-Raphson (numerical) integration scheme, whereas the Python model is solved in the frequency domain using Fourier transforms. First, the modes and eigen frequencies are compared using an eigenvalue analysis. Later a comparison is made for the displacements, bending moments and normal- and shearforces resulting from the DIANA time-history and python frequency domain analysis.

4.1 DIANA & Python model

For the purpose of validation it is chosen to simplify the system to a SFT with 1 tether of 50m and 2 spans of 100m. At either sides of the SFT, land tunnels of 100m are modelled as a beam on elastic foundation (BOEF). The beam type for both the SFT and the landtunnels is of the Class-I type (Euler-Bernoulli). The tether is modelled using a spring interface element. The meshsize of the land tunnels is 10m and at the SFT 1m. The foundation supports the structure in all 3 directions with an equal bedding stiffness of $k_{soil} = 10^7 kN/m^2$ in x, y and z. Coupling between the x, y and z direction through the bedding is not accounted for, thus prescribed accelerations in x, result in zero displacements at all nodes in y and z direction. The tunnel cross-section has an area of $A = 159.32m^2$, a Young's modulus $E_c = 20,000MPa$, and a vertical and horizontal moment of Inertia of $I_{zz} = I_{yy} = 3872m^4$. The tether is given a cross-sectional area $A_{teth} = 0.472m^2$ and a Young's modulus of $E_s = 200,000MPa$.

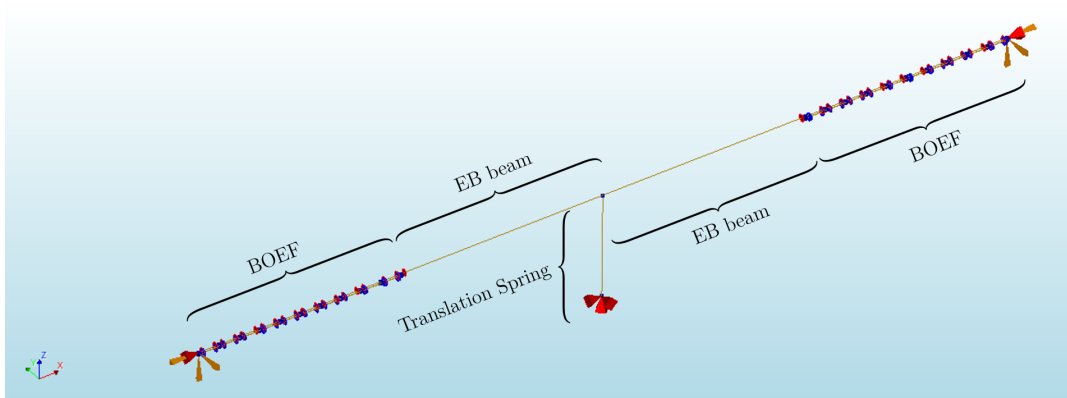


Figure 4.1: DIANA validation model

The boundary conditions at both tunnel ends are clamped, but are given the same prescribed accelerations in x, y and z direction as the bedding nodes. At the foot of the tether a hinged

connection is applied. The interface conditions at the transition between the land tunnel and SFT are assumed fully continues, as well as at the SFT mid node ($x = 200m$) where there is continuity of displacements (incl. tether), rotations, bending moments and shearforces (incl. tether). See equation 4.1.

$x = 0$	$BC1 :$	$\frac{\partial^2 w_{a1}}{\partial t^2} = \frac{\partial^2 w_{prescr}}{\partial t^2}$	(with $a = x, y, z$)
	$BC2 :$	$\frac{\partial w_{a1}}{\partial x} = 0$	(with $a = y, z$)
$x = L_{land}$	$IC1 :$	$w_{a1} = w_{a2}$	(with $a = x, y, z$)
	$IC2 :$	$\frac{\partial w_{a1}}{\partial x} = \frac{\partial w_{a2}}{\partial x}$	(with $a = y, z$)
	$IC3 :$	$\frac{\partial^2 w_{a1}}{\partial x^2} = \frac{\partial^2 w_{a2}}{\partial x^2}$	(with $a = y, z$)
	$IC4 :$	$\frac{\partial^3 w_{a1}}{\partial x^3} = \frac{\partial^3 w_{a2}}{\partial x^3}$	(with $a = y, z$)
$x = L_{land} + \frac{L_{SFT}}{2}$	$IC5 :$	$w_{a2} = w_{a3}$	(with $a = x, y$)
	$IC6 :$	$w_{z,teth} = w_{z2} = w_{z3}$	
	$IC7 :$	$\frac{\partial w_{a2}}{\partial x} = \frac{\partial w_{a3}}{\partial x}$	(with $a = y, z$)
	$IC8 :$	$\frac{\partial^2 w_{a2}}{\partial x^2} = \frac{\partial^2 w_{a3}}{\partial x^2}$	(with $a = y, z$)
	$IC9 :$	$\frac{\partial^3 w_{a2}}{\partial x^3} = \frac{\partial^3 w_{a3}}{\partial x^3}$	(with $a = y, z$)
$x = L_{land} + L_{SFT}$	$IC10 :$	$EI_{sft} \frac{\partial^3 w_{z2}}{\partial x^3} - EI_{sft} \frac{\partial^3 w_{z3}}{\partial x^3} + EA_{teth} \frac{\partial w_{z,teth}}{\partial z} = 0$	
	$IC11 :$	$w_{a2} = w_{a3}$	(with $a = x, y, z$)
	$IC12 :$	$\frac{\partial w_{a2}}{\partial x} = \frac{\partial w_{a3}}{\partial x}$	(with $a = y, z$)
	$IC13 :$	$\frac{\partial^2 w_{a2}}{\partial x^2} = \frac{\partial^2 w_{a3}}{\partial x^2}$	(with $a = y, z$)
$x = 2L_{land} + L_{SFT}$	$IC14 :$	$\frac{\partial^3 w_{a2}}{\partial x^3} = \frac{\partial^3 w_{a3}}{\partial x^3}$	(with $a = y, z$)
	$BC3 :$	$\frac{\partial^2 w_{a1}}{\partial t^2} = \frac{\partial^2 w_{prescr}}{\partial t^2}$	(with $a = x, y, z$)
	$BC4 :$	$\frac{\partial w_{a3}}{\partial x} = 0$	(with $a = y, z$)

(4.1)

Damping is applied in the form of Rayleigh damping with $\alpha_R = 0.400$ & $\beta_R = 0.004$. Morison damping is not applied in the validation model.

4.2 Loading

The loading on both structures is applied in the form of a prescribed acceleration at the bedding (in x, y and z direction) and at the tether seabed support (in z direction). The acceleration signal is derived as the second time derivative of the signal of a smooth blockwave with a displacement of 0.01m. The formula of the displacement signal is:

$$w_{prescr}(t) = \begin{cases} 0 & \text{for } 0 < t < 1[\text{s}] \\ a_{11}(t-1)^{11} + a_{10}(t-1)^{10} + a_9(t-1)^9 + a_8(t-1)^8 & \text{for } 1 < t < 2[\text{s}] \\ +a_7(t-1)^7 + a_6(t-1)^6 + a_5(t-1)^5 + a_4(t-1)^4 & \text{for } t > 2[\text{s}] \\ 0 & \text{for } t > 2[\text{s}] \end{cases} \quad (4.2)$$

with $a_{11} = 0.0008596362437$; $a_{10} = 45.21666689$; $a_9 = -226.0960197$; $a_8 = 466.054813$; $a_7 = -507.6224834$; $a_6 = 309.230708$; $a_5 = -100.6391427$ and $a_4 = +13.85459674$.

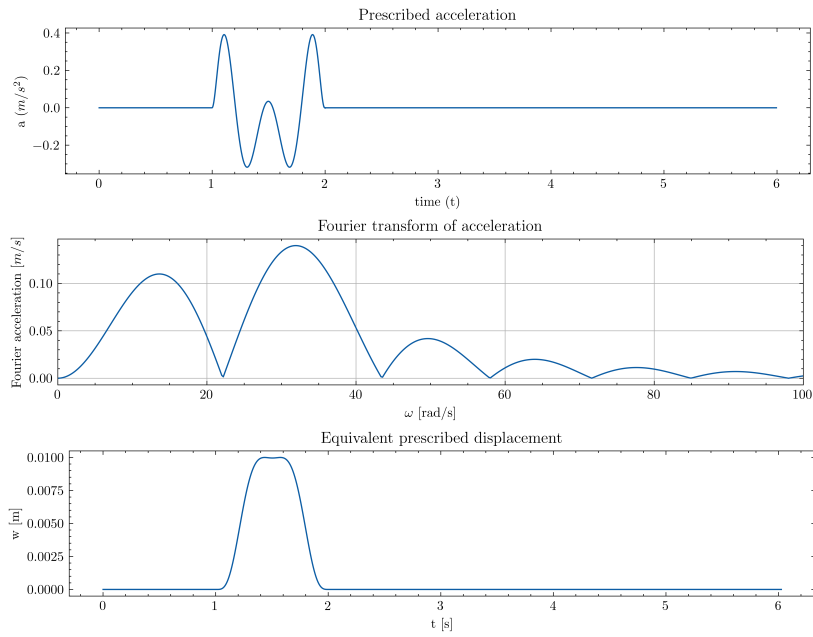


Figure 4.2: Input signal

4.3 Results

In this section the results of the DIANA and Python validation analyses are compared to evaluate if the deformations and internal forces match.

From Figure 4.3 it can be seen that the eigen frequencies of the Python and DIANA model have a good agreement for the longitudinal, horizontal and vertical direction. The differences are greatest for the fundamental frequencies (1.235, 4.273 & 3.973% for respectively the x, y and z direction) and converge quickly for the higher frequencies (less than 0.15% for the 7th mode in all directions).

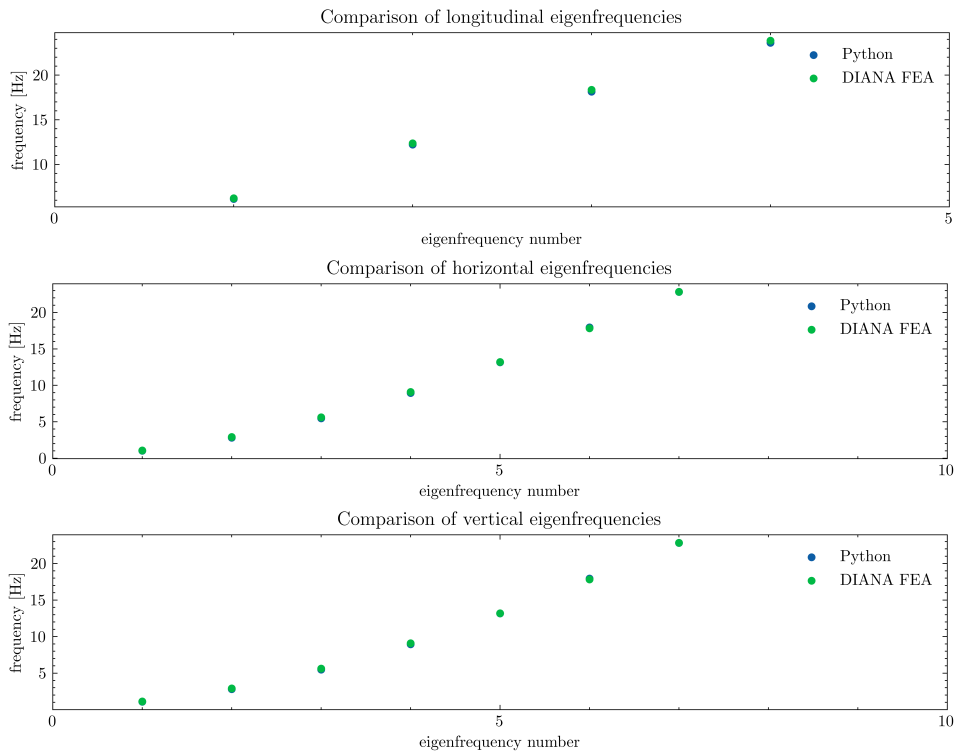


Figure 4.3: comparison of eigen frequencies

The mode shapes of the respective eigen frequencies are plotted in Figure 4.4. These modes are derived in the Python model and have a good correspondence with the shapes from the DIANA model (not displayed here). For the longitudinal modes, relatively large displacements occur at the land tunnels, as the tunnel-soil stiffness ratio is high here. For the transverse modes (vertical and horizontal) it can be seen that hardly any displacements occur in the land tunnels, only in the last 10 to 30 metres, approaching the SFT. The tunnel-soil stiffness ratio is here significantly lower. The (unitless) displacements are greatest in the SFT for all modes, due to the largest flexibility between $x = 100$ and $300m$. The 7th mode allows for relatively large displacements at the transition structure in horizontal and vertical direction. This mode is a result of the soil-structure interaction, that is not seen when the system boundary is set at the SFT end.

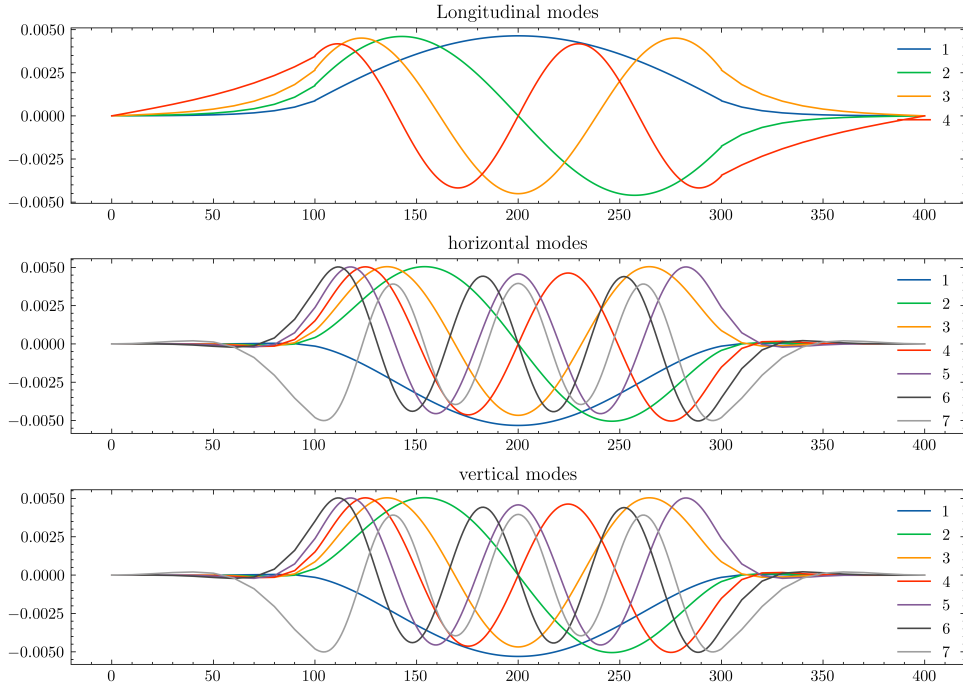


Figure 4.4: Mode shapes of the python validation model

The results of the Python model in the frequency-domain are transformed back to the time-domain to obtain the displacements as function of time in longitudinal (Figure 4.5), horizontal (Figure 4.6) and vertical direction (Figure 4.7). The displacements are compared with the DIANA time-history results at the transition ($x = 100$) and mid node ($x = 200$).

The Python displacements at the transition node in all directions (Figures 4.5, 4.6 and 4.7) have a slight downward offset from the neutral axis. This static displacement presumably originates from the Fourier transform and the chosen method to solve the system. When the system is solved for $\tilde{\mathbf{U}}(\omega)$ as in equations 3.4 and 3.5, the ω^2 term in the inverse creates a peak at the (static) radial frequency of $\omega = 0 \text{ rad/s}$. The displacement is small here, but division by zero lets the displacement be non-zero for the static frequency. This causes an offset for all displacement results. This offset will however not influence the results of the internal forces, since no additional bending or shearing will occur in a rigid body displacement.

The displacement signals of the transition and mid node respond the same when the signal is started (equal acceleration), rise to the same height, and dampen out at equal pace. This means that the Rayleigh damping matrices act similar in the frequency-domain and time history analyses. A slightly large deviation between the results is seen in Figure 4.7, where the vertical DIANA peak displacement at mid node is 4.524% greater than the Python maximum displacement. The vertical transition node deviation is only -0.630% . The horizontal displacements differ -0.884 and -1.889% at the transition node and mid node. In longitudinal direction this is -0.760 & -0.509% respectively.

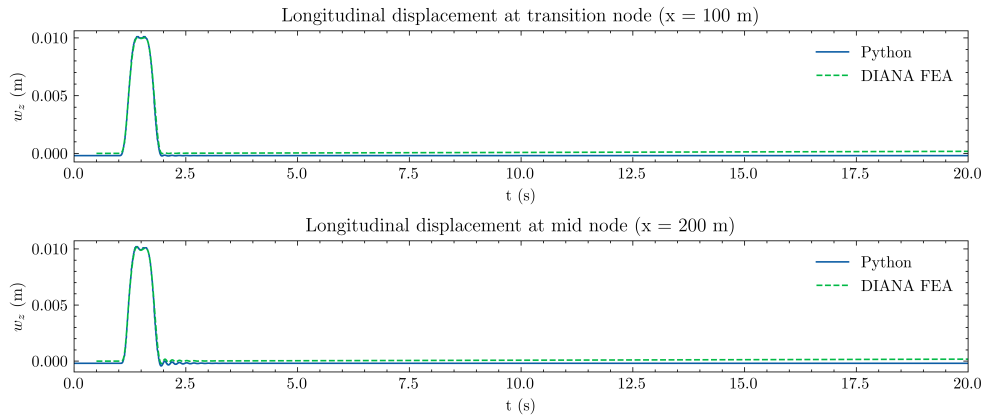


Figure 4.5: Comparison of longitudinal displacements

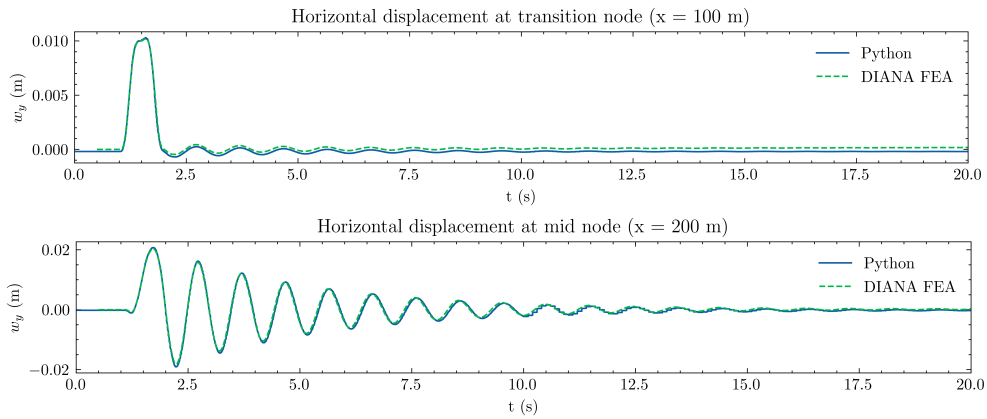


Figure 4.6: Comparison of horizontal displacements

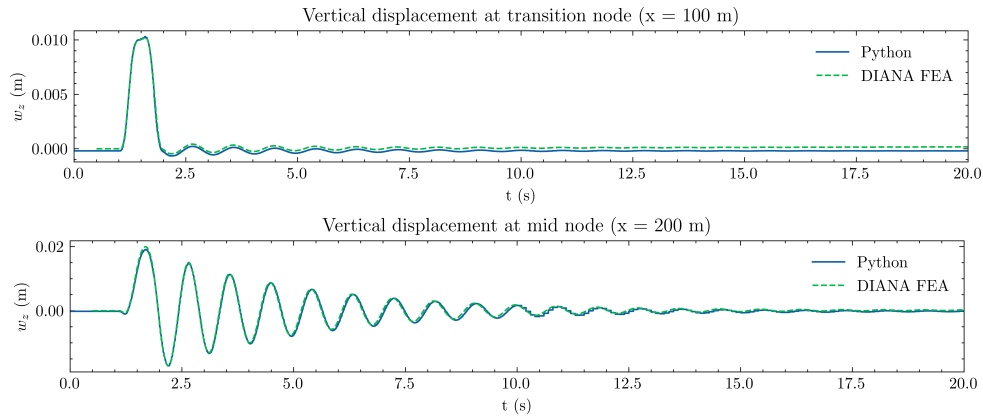


Figure 4.7: Comparison of vertical displacements

The bending moments in horizontal (Figure 4.8) and vertical direction (Figure 4.9) are compared for the transition node ($x = 100m$) and the mid node ($x = 200m$). In horizontal direction, deviations in maximum bending moment M_{yy} at the mid node and transition node are -3.097 and -4.284% respectively. Vertically, the maximum bending moment M_{zz} at the mid nodes are exactly the same (0.000% deviation), whereas at the transition node the deviation maximum vertical bending moment M_{zz} is 1.449%. Minimal deviations can be seen at the startup effect in the vertical mid node signal, while the other signals match very well.

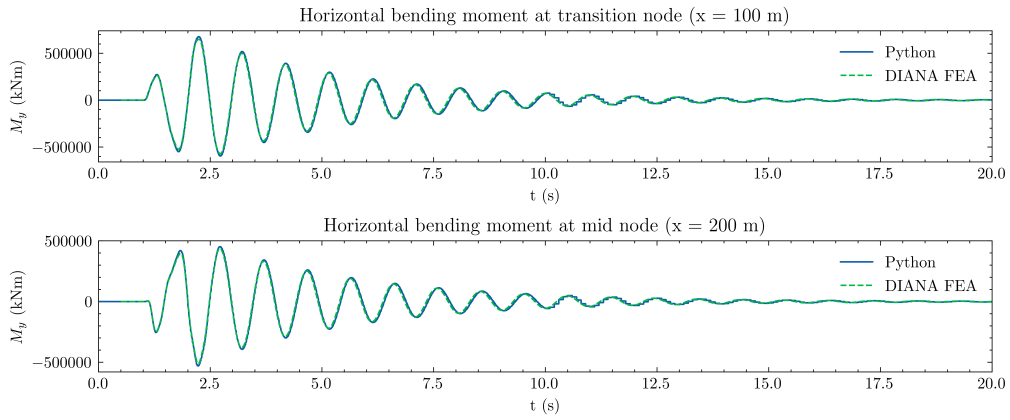


Figure 4.8: Comparison of horizontal bending moments

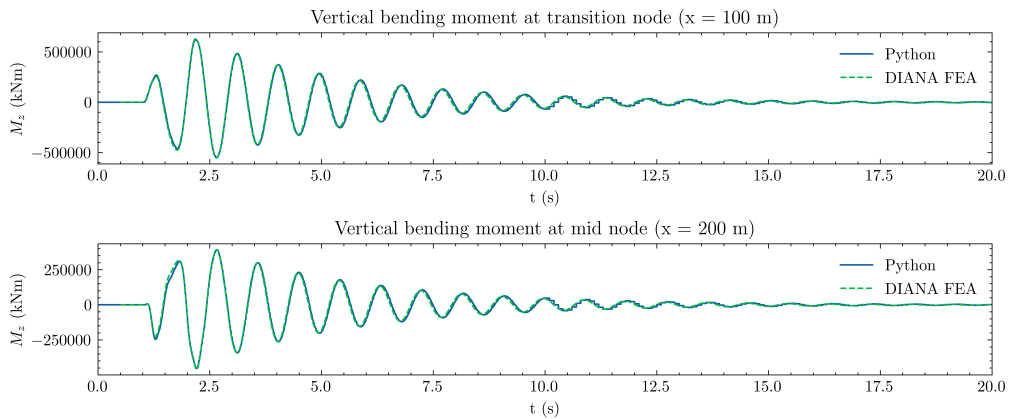


Figure 4.9: Comparison of vertical bending moments

The normal force results are compared for the transition node ($x = 100m$) and the node at quarter SFT length ($x = 150m$) in Figure 4.10. The capricious patterns match quite well, where the startup effect is the same and damping occurs at the same pace. The peak normal forces have a larger deviations of -11.199% for the transition node and -14.420% for the quarter node. This deviation is also visible when the signal dampens out, although it occurs at the same pace. The natural frequencies in longitudinal direction are higher than in both transverse directions, which can be seen in the dynamic response of Figure 4.10: more high frequency vibrations. The response dampens out at a much higher rate in longitudinal direction then in the transverse directions.

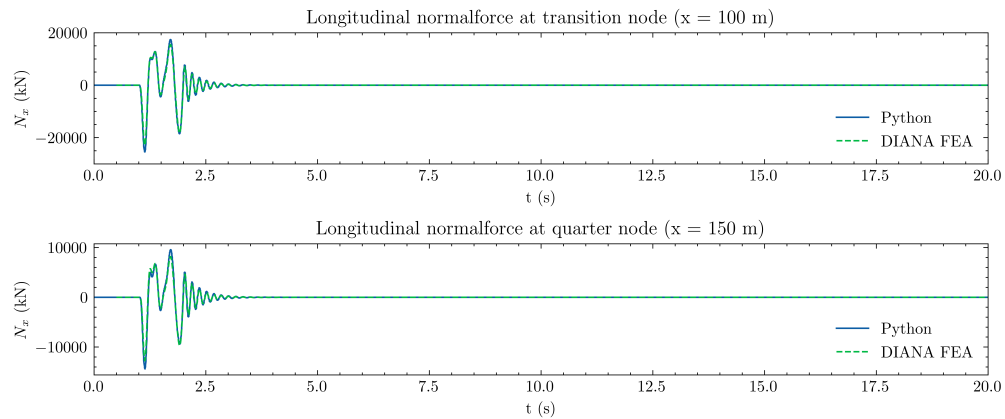


Figure 4.10: Comparison of normal forces

The shear force results in horizontal and vertical direction are displayed in Figures 4.11 & 4.12. These show some deviations at the startup effect. The python model shear force seems to startup not as quick as the DIANA shear force. This is mainly visible at the first whole period

of vibration. At the second peak, the deviations are again reduced, and the two model results converge. The peak shear forces in horizontal direction match well. The deviations between the DIANA and Python results at mid land tunnel ($x = 50m$), transition node ($x = 100m$) and mid node ($x = 150m$) are $-3.539, -4.566$ & 2.430% . The peak shear force deviations in vertical direction have deviations of $-1.647, 1.988$ & -12.202% for the mid land tunnel, transition node and mid node. The large deviation at the mid node shear force is due to the fact that it occurs on the first wave period. For the other signals it occurs on the second wave period, where the signal has converged again. The fact that the deviations are so small, shows that the displacement signal even has good correspondence up to the 3^{th} spacial derivative. The differences in start up effect must be considered, but should be covered by model safety factors within most building codes.

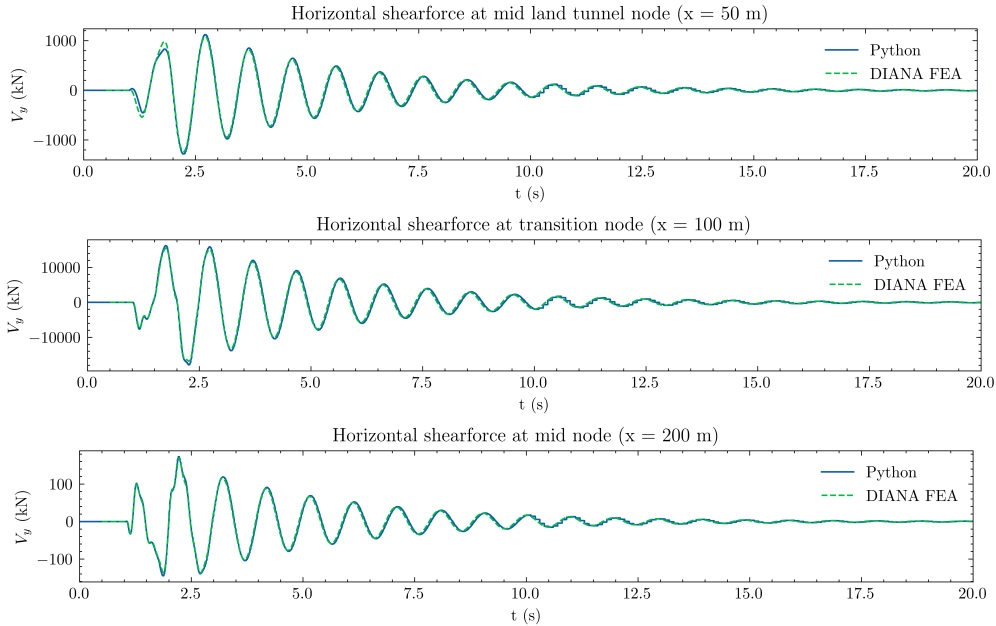


Figure 4.11: Comparison of horizontal shear forces

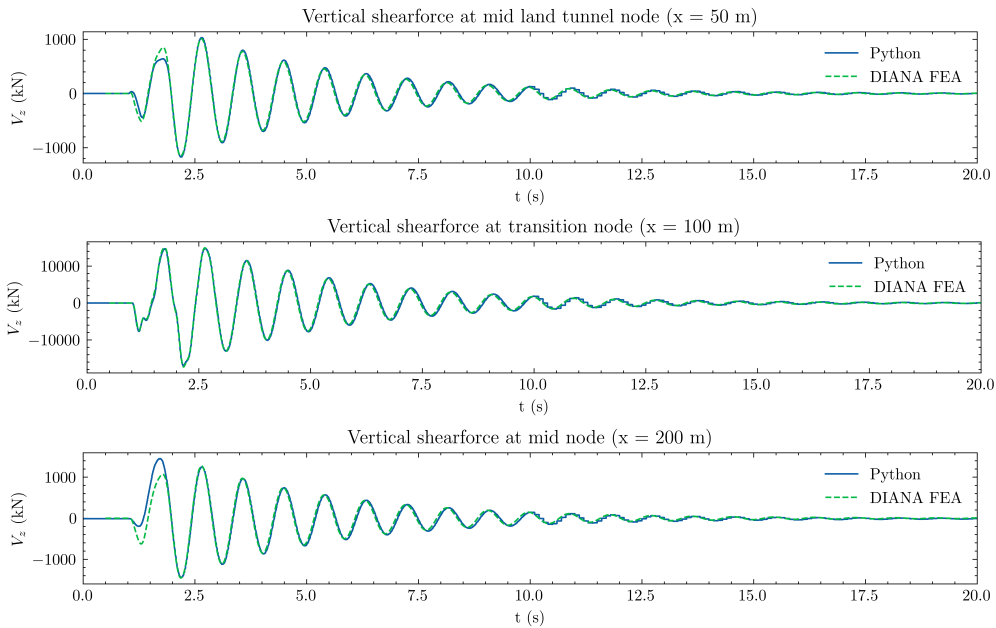


Figure 4.12: Comparison of vertical shear forces

At last, the normal forces in the single tether are studied. It should be noted that the Python tether consists of 30 elements, while the DIANA tether consists of only 1 element (due to limits within the software). The choice for multiple elements in Python was made, such that a wave could pass through the tether. In structural dynamics at the instant that an impulsive load hits a tether,

the reaction force is not felt immediately at the other tether end. This effect of delay within the tether seems to be very small, especially for a short one (50 meters). Differences between Python and DIANA at peak normal forces are 0.834% so the response of both tether systems overlap properly.

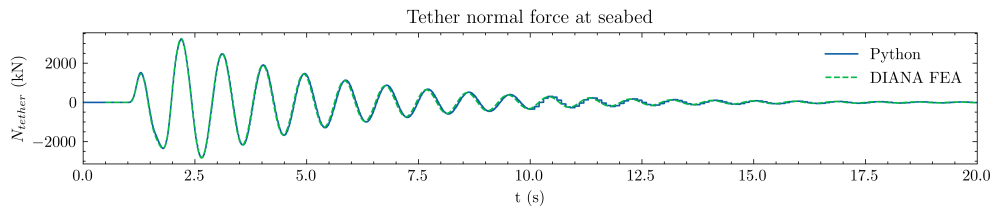


Figure 4.13: Comparison of tether normal forces

Chapter 5

Case study

The method, as established in Chapter 3, is applied in a case that resembles an SFT, the building site and loading as it is expected to take shape in the future. The case is described in this chapter.

5.1 Location

Soil-structure interaction is an important part of this thesis, therefore a reference project is chosen to apply the model in a realistic environment. This location is the basis for finding subsoil conditions and a geological profile for the transition structure and land tunnel.

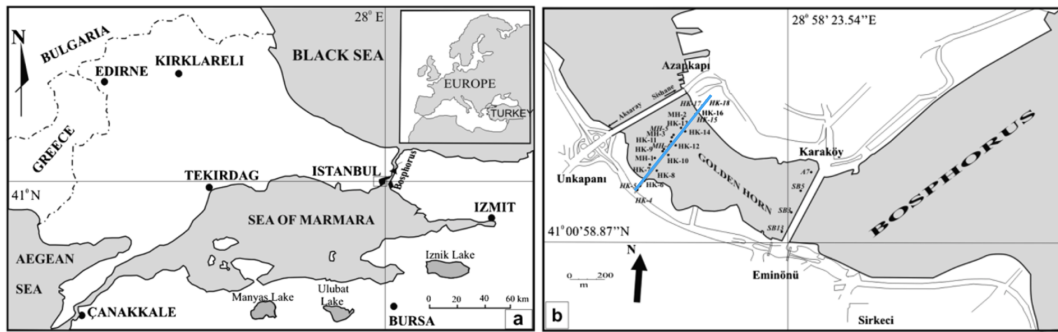


Figure 5.1: Location (in blue): Golden Horn, Istanbul, Turkey (Meriç et. al., 2007)

The case study is based on a previous tunnel project by TEC, located in Istanbul (Turkey), in the Golden Horn estuary (see Figure 5.1, (Meriç, Görmüş, & Avşar, 2007)). The Golden Horn is a major waterway and primary inlet of the Bosphorus. During this project, a connection had to be realized between Unkapani in the south-west and Kasimpaşa in the north-east. According to the trade-offs made by TEC, the most suitable option was an immersed tube bridge: an immersed tunnel on concrete columns to reduce the maximum tunnel depth. A tunnel below or on the river bed was not possible, due to densely populated districts on either sides of the estuary and the need to connect the tunnel to the boulevards. The building site has steep slopes approaching the estuary, and is seismically active, which make the project suitable for a case study.

The magnitude of the span and depth of the Golden Horn, 200 and 40 metres respectively, are not large enough to make a SFT an economical solution. The soil geometry below the canal will therefore be scaled by a factor of 5 to a length of 1000 metres and a depth of 200 metres. The soil geometry and profile around the land tunnels will remain equal to the original (unscaled) building plans. The land tunnel cuts through 100 metres of artificial filling, followed by 120 metres of clay and then transitions into Paleozoic basement, as can be seen in the figure below.

For the derivation of the (coupled) soil bedding stiffness matrix, the Unkapani side of the soil profile is used. This provides a realistic bedding stiffness to be used for both land tunnels in the global model. A symmetrical model is preferred such that inconsistencies in results due to unsymmetrical beddings stiffnesses are avoided.

The soil layers that the tunnel crosses are reduced to three homogeneous soil blocks. For these

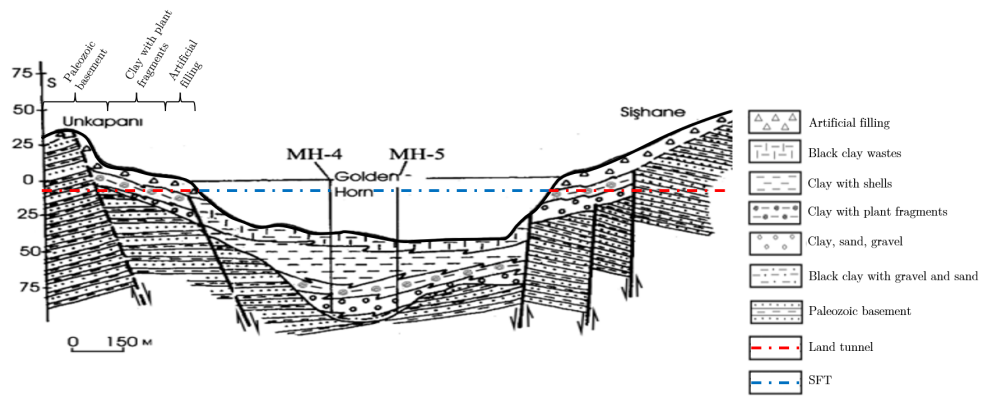


Figure 5.2: Geological profile of building site (modified from Meric et al., 2007)

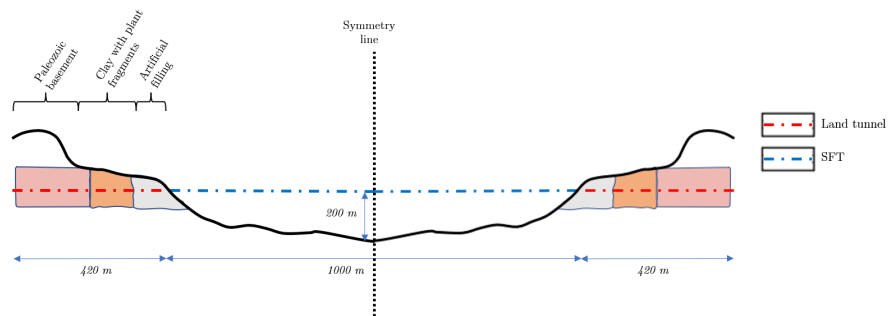


Figure 5.3: Scaled, symmetrical geological profile

blocks, the average soil characteristic of the respective layers on top of the bed rock are used. These are Paleozoic basement (claystone), clay and artificial filling (medium stiff clay). In the next section a description is given of their properties.

Groundwater levels around the Golden Horn coasts are ranging from 1.3 to 4.4 metres below the surface level. As the SFT is build more then 30 metres below the water surface, the land tunnel will be surrounded by saturated soil.

5.1.1 Geological material characteristics

The subsoil material properties that resulted from the site investigation studies by TEC (TEC, 2016) are listed below. These characteristics are used as input for the derivation of the soil stiffness matrix using Comsol.

Layer 1: Claystone (Paleozoic basement)			
E-modulus layer 1	E_1	18,000	[MPa]
Poisson ratio layer 1	ν_1	0.37	[-]
Int. friction angle layer 1	ϕ_1	32	[°]
Saturated specific weight layer 1	$\gamma_{sat;1}$	2,400	[kg/m3]
Layer 2: Clay (with plant fragments)			
E-modulus layer 2	E_2	12	[MPa]
Poisson ratio layer 2	ν_2	0.35	[-]
Int. friction angle layer 2	ϕ_2	25	[°]
Saturated specific weight layer 2	$\gamma_{sat;2}$	1,800	[kg/m3]
Layer 3: Artificial filling			
E-modulus layer 3	E_3	7	[MPa]
Poisson ratio layer 3	ν_3	0.30	[-]
Int. friction angle layer 2	ϕ_3	25	[°]
Saturated specific weight layer 3	$\gamma_{sat;3}$	1,780	[kg/m3]

Table 5.1: Geological material characteristics

5.2 Cross-sectional properties

The SFT and land tunnels are assigned similar cross-sectional properties: a double circular section. The material that is used for the tunnels is reinforced concrete and the tethers and mooringlines are in S355 steel. The water properties used in the Comsol model and for the Morison equation are listed as well.

Parameter		Value		Parameter		Value	
Reinforced Concrete				Steel			
E-modulus concrete	E_c	20,000	[MPa]	E-modulus steel	E_s	200,000	[MPa]
Poisson ratio concrete	ν_c	0.20	[-]	Poisson ratio steel	ν_s	0.30	[-]
Density reinforced concrete	ρ_c	2,500	[kg/m3]	Density steel	r_s	7,800	[kg/m3]
Water							
Density water	ρ_w	1,000	[kg/m3]				
P-wave speed water	c_w	1,500	[m/s]				

Table 5.2: Material properties

The cross-sectional properties of the SFT and tethers are determined in a Buoyancy-Weight-Ratio calculation. The objective was a BWR of 1.20 for the SFT, such that the SFT will float, but the tethers remain under tension at all times to prevent them from slacking. The double circular section (see Figure 5.4) ensures a large horizontal bending stiffness for the SFT, such that the horizontal deformations are limited. The profile of free space is chosen such that both tunnel tubes can accommodate 3 traffic lanes. In the lower area a maintenance corridor is located, together with extra room for ballast concrete, cables and drainage pipes.

The tethers have been designed for a BWR of 1.00 such that no extra weight is added to the SFT. The cross-sectional area is chosen to be $A_{teth} = 0.236m^2$, with a diameter $D_{teth} = 1550mm$, a wall thickness of $t_{teth} = 50mm$ and two tethers every 100m. Mooring lines are given a cross-sectional area of $A_{moor} = 0.100m^2$ with two mooring lines per 200m.

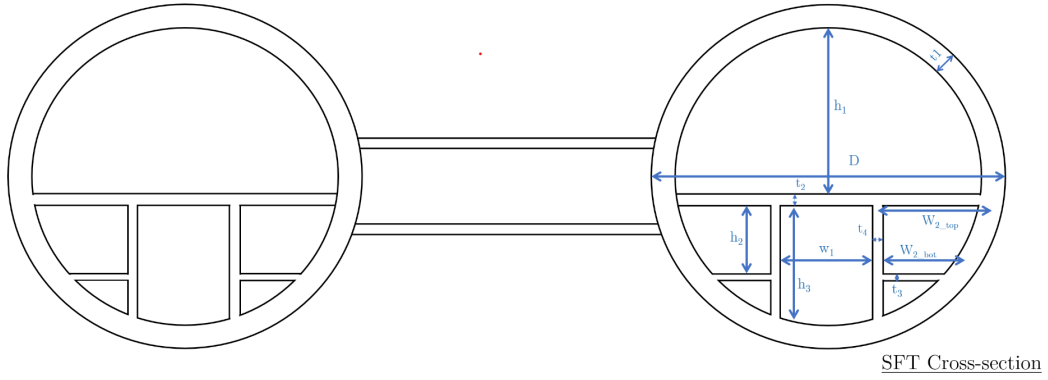


Figure 5.4: Tunnel cross-section

Parameter	Value	Parameter	Value
Outer tube diameter	D 18.0 [m]	Middle corridor width	w_1 5.00 [m]
Traffic area height	h_1 9.00 [m]	Right corridor top width	$w_{2,top}$ 5.50 [m]
Upper inner wall height	h_2 3.50 [m]	Right corridor bottom width	$w_{2,bot}$ 5.39 [m]
Total inner wall height	h_3 6.90 [m]	Outer wall thickness	t_1 1.00 [m]
Profile of freespace height	h_{pfs} 3.50 [m]	Traffic floor thickness	t_2 0.70 [m]
Profile of free space width	w_{pfs} 14.39 [m]	Lower floor thickness	t_3 0.50 [m]
Moment of inertia (vertical)	I_{zz} 3872 [m ⁴]	Inner wall thickness	t_4 0.70 [m]
Moment of inertia (horizontal)	I_{yy} 131328 [m ⁴]	Cross-sectional area	A_{tunnel} 159.32 [m ²]

Table 5.3: Cross-sectional properties

5.3 End-joint properties

In the parameter study in chapter 6 a series of different end-joints is applied in the model to find out the maximum PGA for the structure per joint. In previous research by Speelman (Speelman, 2021), it was found that bending moments in SFTs with seismic loading are generally greatest at the SFT end-joints. One of the recommendations of this study was to further investigate the effect of the land connection joints, as the input motion at these joints most influenced the SFT's dynamic response. Therefore, in this thesis a selection is made of several possible end-joints and extra devices for altering the displacements and internal forces

A selection of the different measures that are taken in this study:

1. Monolithic end-joint
2. Hinged end-joint
3. End-joint with bending capacity
4. Base-isolated end-joint (with/without bending capacity)
5. End-joint with bending capacity and viscous damper

The monolithic end-joint is preferred above other joints, because it ensures water tightness of the joint and has a higher durability, since no moving parts are involved. Due to lack of deformation capacity in monolithic joints, bending moments can grow large. When its capacity is exceeded the structural engineer must look at other alternative joints.

The hinged end-joint can reduce bending moments at the transition structure to zero, but has the risk that gapping (large rotations) become problematic. In that case intermediate solutions as described in the next section become good options.

5.3.1 End-joint with bending capacity

End-joints with bending capacity entail a connection that can mechanically be schematized by a rotation spring. These connections may be constructed using rubber gaskets or pads, that provide a flexible connection between the SFT and the transition structure. Gaskets are used in immersed tunnel construction for creating flexible joints and ensuring a waterproof connections between elements. Rubber pads can be applied similar to those used for bridge supports.

Manufacturers of GINA profiles provide graphs with the respective force-compression relationship as can be seen in figure 5.5 below. This figure is provided by Trelleborg for their TB ETS-320/370 tunnel gasket. At an avarage depth of $h = 39m$ and with a specific water weight of $\gamma_{water} = 10kN/m^3$, the total water pressure on the tunnel cross-section is $F_{water} = \frac{1}{4}\pi D^2 h \gamma_{water} = 99243.3kN$. For a tunnel circumference of $C = 53.4m$ this results in a reaction force per unit length of gasket of $R_{gina} = 1858.5kN/m$.

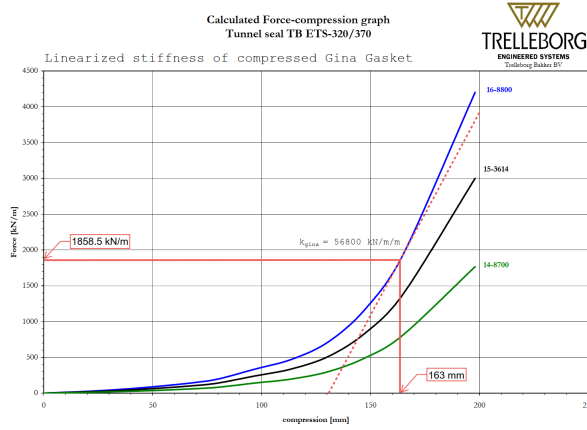


Figure 5.5: Linearized Gina stiffness

For a force of $1858.5 \frac{kN}{m}$ the GINA compresses approximately $163mm$ and linearizing its stiffness around this deformation results in a stiffness of $k_{gina} = 56800 \frac{kN}{m^2}$.

For a SFT cross-section with two tubes and a diameter of $18m$, the longitudinal joint stiffness yields:

$$k_x = 2Ck_{gina} = 6.0670 * 10^6 \frac{kN}{m} \quad (5.1)$$

The vertical rotational stiffness can be found as described by P. Zou (P. Zou, 2022):

$$k_{\theta z} = 2\pi k_{gina} \frac{D^3}{8} = 2.1917 * 10^8 \frac{kNm}{rad} \quad (5.2)$$

The horizontal bending stiffness is found using the following formula below. Here L_{ctc} is the horizontal center-to-center distance between the two SFT tubes and D represents the tube diameter.

$$k_{\theta z} = k_x \int_{\theta=0}^{\theta=2\pi} y^2 dx = 2.646 * 10^9 \frac{kNm}{rad} \quad (5.3)$$

with $y = \frac{L_{ctc}}{2} + \frac{D}{2} \sin(\theta)$;
 $L_{ctc} = 40m$; $D = 18m$.

The GINA profile is used as a benchmark for the spring stiffness parameters in the parameter study in Chapter 6. Two other joints with rotational bending capacity in y and z, and longitudinal flexibility are applied and have been named "GINA x10" and "GINA /10" meaning joints that have a rotational/translational stiffness equal to 10 times more and 10 times less then the GINA joint respectively. These end-joint spring parameters are defined in Table 5.4 below:

	k_u [kN/m]	k_{wz} [kN/m]	$k_{\theta z}$ [kNm/rad]	k_{wy} [kN/m]	$k_{\theta y}$ [kNm/rad]
<i>Monolithic</i>	10^{10}	10^{10}	10^{17}	10^{10}	10^{17}
<i>GINA x10</i>	$6.067 \cdot 10^7$	10^{10}	$2.1917 \cdot 10^9$	10^{10}	$2.646 \cdot 10^{10}$
<i>GINA</i>	$6.067 \cdot 10^6$	10^{10}	$2.1917 \cdot 10^8$	10^{10}	$2.646 \cdot 10^9$
<i>GINA /10</i>	$6.067 \cdot 10^5$	10^{10}	$2.1917 \cdot 10^7$	10^{10}	$2.646 \cdot 10^8$
<i>Hinged</i>	10^{10}	10^{10}	0	10^{10}	0

Table 5.4: End-joint spring stiffness parameters

5.3.2 End-joint with viscous damper

Fluid viscous dampers can be applied at the transition structure in case of a flexible joint with or without bending capacity to prevent large displacements due to resonance. Viscous dampers have been widely applied as a measure to lower displacements due to seismic activity, but also in case of wind or industrial loads. The dampers can be placed around the tunnel circumference and mounted to the transition structure. Preferably, the devices are mounted on top and below the tube for maximum rotational damping in vertical direction. For horizontal rotational damping, these can be applied at half tube height to maximize the lever arm.

In the parameter study (Chapter 6) 2×2 dampers will be applied, one on top of each tube and one below each tube. Dampers can have non-linear force-displacement relationships, but as the global model is linear, also linear viscous dampers are used. The dampers are given values of $C = 8,000 \frac{kNs}{m}$ and the number of dampers is $n_{damp} = 4$. The longitudinal damping parameter c_x can now be determined as:

$$c_x = n_{damp} C = 32,000 \frac{kNs}{m} \quad (5.4)$$

The dampers are applied with a vertical lever arm of $e = 9.00m$ with respect to the neutral axis. This yields a vertical rotational damping parameter $c_{\theta z}$:

$$c_{\theta z} = 4 C e^2 = 2.592 \cdot 10^6 \frac{kNms}{rad} \quad (5.5)$$

5.4 Earthquake signals

A selection of three strong motion earthquake signals has been made within the database of Turkish strong motion signals: AFAD (Disaster and Emergency Management Authority). These signals all originate from Turkey and date from the last 25 years. The main requirement for this selection was that the signals should vary in frequency range, such that the effects on the tunnel could be observed for high, mid and low frequency earthquakes and narrow or broad banded frequency ranges.

The Derince (1999) earthquake (AFAD, 2022) can be characterized as a low frequency, broad banded earthquake. This can be seen from figure 5.6 where peaks are visible in the dominant frequencies at 0.072, 0.12 and 0.29 Hz, which can be found back in figure 5.8, where clearly long periods dominate the displacement signal. However, high frequency content is also present in the Fourier spectrum with medium sized peak up to 6 Hz. The peak ground acceleration (PGA) of the original signal is $2.63m/s^2$ or $0.26g$ in the north-south direction with a moment magnitude of $M_w = 7.6$.

A clear contrast is visible with The Van (2011) earthquake (AFAD, 2022), which is a narrow banded mid range frequency signal (see Figure 5.6), where frequencies between 0.2 and 2 Hz are most present, but the high and low frequencies are absent. The frequency content can be clearly recognized in the displacement signal, due to its capricious pattern. The PGA of the original signal is $1.71m/s^2$ or $0.17g$, with the strongest motions in the north-south direction. The original moment magnitude scale is $M_w = 7.0$.

Finally, there is the Bingol (2003) earthquake (AFAD, 2022), which is wide banded, but with its characteristic frequencies between 0.4 and 10 Hz. Therefore, it is the signal with the most high frequency content within this selection of signals. Its original PGA is found to be $5.01m/s^2$ or $0.50g$ in the north-south direction as well. Its original moment magnitude scale is $M_w = 6.3$, which is the lowest of the selected original signals.

The three signals are linearly scaled to a PGA of $0.1g$, resulting in identical patterns with lower amplitudes in the acceleration and displacement signals. Equal PGA's however do not mean that results from the analysis in terms of displacements and internal forces will be of the same magnitude, as the Fourier spectrum of all three signals is significantly different. A good indicator for large displacements are the structure's fundamental eigen frequencies. In case these align with the earthquakes strong motion frequencies, this can point towards a strong magnification of the internal forces and displacements due to resonance phenomena.

For the parameter study in Chapter 6 all signals are scaled down to a PGA of $0.1g$ ($0.981 \frac{m}{s^2}$), as displayed in Figure 5.6.

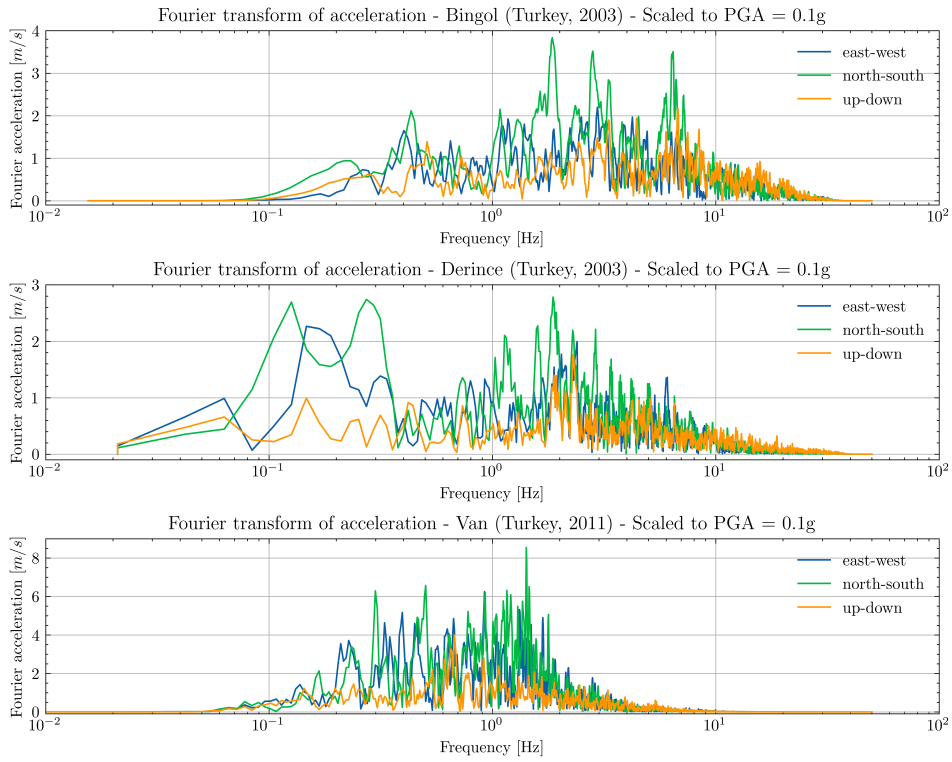


Figure 5.6: Fourier spectrum of Acceleration signals

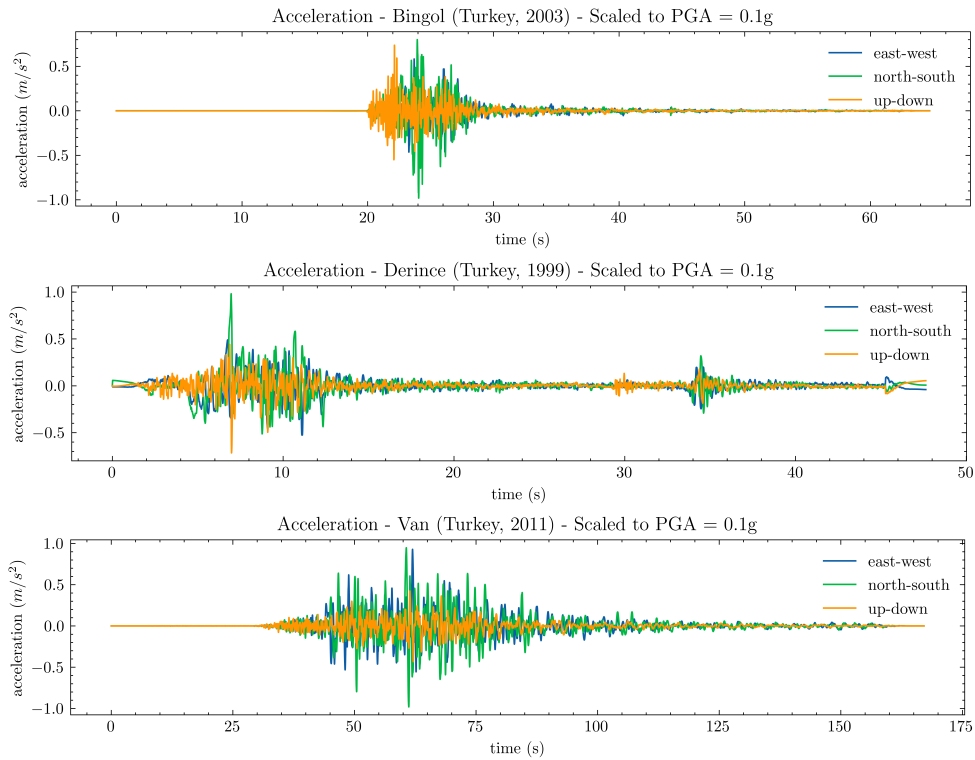


Figure 5.7: Acceleration signals (scaled to 0.1 g)

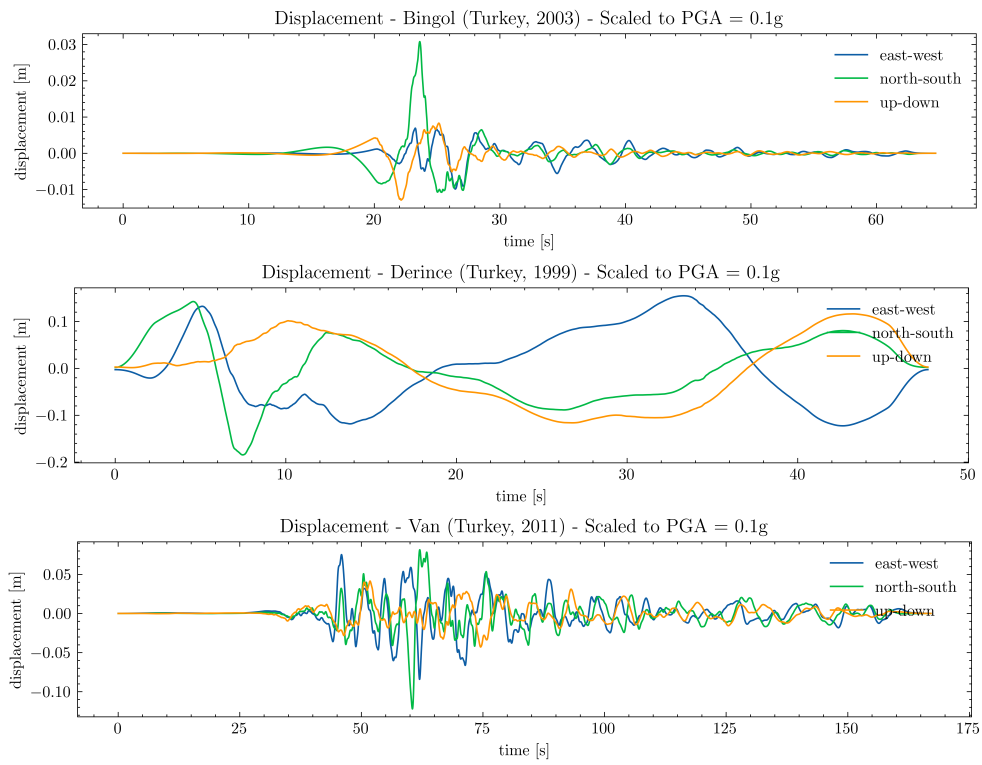


Figure 5.8: Displacement signals (scaled to 0.1 g)

Chapter 6

Parameter study

This chapter covers the static and dynamic parameter study that is performed by applying the global model described in this thesis. In section 6.1 the most common static loads are applied on the model and its displacements and stresses are checked for several limit states. In section 6.2 the dynamic (seismic) behavior is studied by applying 3 different earthquakes scaled a PGA of 0.1 g. Moreover, several end-joints are applied at the transition structure to find its influence on the maximum peak ground acceleration the SFT can bear.

6.1 Static behavior

6.1.1 Static loading

Static loads are applied in the form of self weight, dead loads, the upward buoyant force and traffic loading. The ratio between the upward permanent force ($G_{k,buoy}$) and downward permanent forces ($G_{k,self}$, $G_{k,SDL}$ and $G_{k,util}$) should be greater or equal to 1.20 to realize the buoyancy weight ratio as stated in subsection 2.1.1.

For the purpose of self weight, a tunnel cross-section is assumed as described in Figure 5.4. It has a cross-sectional area of $A_{tunnel} = 159.32m^2$, with a concrete unit weight of $\rho_c = 25.96 \frac{kN}{m^3}$. This includes a material safety factor of 1.038. The resulting self weight is a line load of $G_{k,self} = 4,135.94 \frac{kN}{m}$. The superimposed dead load (SDL) in the tunnel accounts for asphalt, traffic barriers and fire protection on walls and ceiling. The SDL is assumed as $G_{k,SDL} = 59.8 \frac{kN}{m}$ for two traffic tubes. Extra utilities, together with mechanical, electrical and plumbing systems (MEP) are taken into account as well. The load is estimated based on previous TEC projects. The extra dead weight is assumed as $G_{k,util} = 29.6 \frac{kN}{m}$ for two traffic tubes.

The upward buoyant force can be found as the weight of the water that is displaced by the tunnel body. The total area of the tunnel body is $A_{displ} = \frac{1}{4}\pi D^2 = 508.94m^2$ and the unit weight of water is $\rho_w = 9.99 \frac{kN}{m^3}$, to account for a low salinity (this would decrease the BWR, which is not desirable). The product is a buoyancy load of $G_{k,buoy} = -5089.40 \frac{kN}{m}$ (negative, as it is in upward direction). The BWR is found to be 1.229, and thus satisfies the requirements ($BWR \geq 1.20$).

Finally, the traffic load is assumed as a uniformly distributed load (UDL) as described in Eurocode 1 ([NEN-EN 1991-2, 2021](#)). This document is assumed to be best applicable to the SFT type of structure, because in terms of structural behavior, it is most comparable to the behavior of a bridge. However, a bridge which is supported by very flexible intermediate supports and submerged in water. In the future possibly a more suiting code will be released.

For this preliminary study LM1 is presumed to cover most of the effects of the traffic of lorries and cars. LM1 consists of a tandem load (double axle concentrated load), combined with a uniformly distributed load. For SFT-structures, the tandem load is considered negligible, due to the enormous length of the structure (1000 meters or more). The tandem load consists of 2×12 point loads, equal to a total of $2400kN$. The self weight of the SFT however is $4,135.94 \frac{kN}{m}$, which

is applied over the full length. The tandem load is thus considered of minor importance for the structures global behavior.

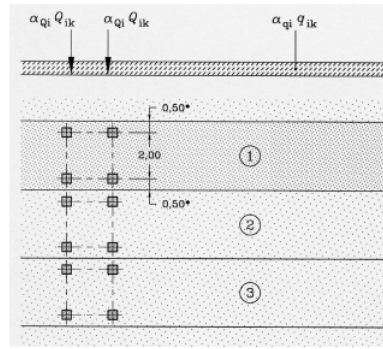
Tabel 4.2 – Belastingsmodel 1: karakteristieke waarden

Positie	Tandemstelsel TS	Gelijkmatig verdeelde belasting (GVB)
	Aslast Q_{ik} (kN)	q_{ik} (of q_{ik}) (kN/m ²)
Rijstrook nummer 1	300	9
Rijstrook nummer 2	200	2,5
Rijstrook nummer 3	100	2,5
Overige rijstroken	0	2,5
Resterende oppervlakte (q_{ik})	0	2,5

Figure 6.1: Load Model 1 (NEN-EN-1991-2 table 4.2)

The UDL of LM1 is applied over the full length of the land tunnel and the SFT, with a distributed load $q_{1,k} = 9 \frac{kN}{m^2}$ and $\alpha_{q1} = 1.15$ for traffic lane 1 and $q_{i,k} = 2.5 \frac{kN}{m^2}$ and $\alpha_{qi} = 1.40$ for traffic lanes 2 and 3 with all a width of $b_{lane} = 3.50m$. The total assumed traffic load is thus:

$$Q_{k,traf} = n_{tubes} \times (b_{lane} \alpha_{q1} q_{1,k} + 2 \times b_{lane} \alpha_{qi} q_{i,k}) = 121.45 \frac{kN}{m} \quad (6.1)$$



Verklaring

- (1) rijstrook nummer 1 : $Q_{1k} = 300 \text{ kN}$; $q_{1k} = 9 \text{ kN/m}^2$
 - (2) rijstrook nummer 2 : $Q_{2k} = 200 \text{ kN}$; $q_{2k} = 2,5 \text{ kN/m}^2$
 - (3) rijstrook nummer 3 : $Q_{3k} = 100 \text{ kN}$; $q_{3k} = 2,5 \text{ kN/m}^2$; tussenafstand assen in tandemstelsel = 1,2 m
- * Voor $w_l = 3,00 \text{ m}$

Figuur 4.2a – Toepassing van belastingsmodel 1

Figure 6.2: Load Model 1 (NEN-EN-1991-2 figure 4.2a)

The balancing pretension forces in the tethers keep the system in a state of equilibrium. They are found as:

$$P_{k,teth} = \frac{(G_{k,buoy} + G_{k,self} + G_{k,SDL} + G_{k,util})}{L_{cc} \times n_{teth}} = 45,182.43kN \quad (6.2)$$

Where the center to center distance of the tethers is $L_{cc} = 100m$ and the number of tethers per section is $n_{teth} = 2$.

The loads are combined for Serviceability Limit State (SLS) with unit safety factors and for Ultimate Limit State (ULS) using the combination rules from NEN-EN 1990 table 6.10a and 6.10b. This results in the following combinations:

$$SLS = 1.00G_{k,self} + 1.00G_{k,perm} + 1.00G_{k,buoy} + 1.00P_{k,teth} + 1.00\psi_{0,sls}Q_{k,traf} = -773.99kN/m + P_{k,teth} \quad (6.3)$$

$$ULS_{6.10a} = 1.00G_{k,self} + 1.40G_{k,perm} + 1.40G_{k,buoy} + 1.00P_{k,teth} + 1.50\psi_{0,ULS}Q_{k,traf} = -667.26kN/m + 1.00P_{k,teth} \quad (6.4)$$

$$\begin{aligned}
ULS_{6.10b} &= 1.00G_{k,self} + 1.25G_{k,perm} + 1.00G_{k,buoy} + 1.00P_{k,teth} + 1.50Q_{k,traf} \\
&= -654.33kN/m + 1.00P_{k,teth}
\end{aligned}
\tag{6.5}$$

With $\psi_{0,SLS} = 0.7$ & $\psi_{0,ULS} = 0.8$. From the two ULS load combination rules (6.10a & 6.10b) the normative combination must be used. In this case $ULS_{6.10b}$ gives the largest downward load (causing the largest internal forces at the end-joint).

6.1.2 Static results

In case the SLS loads are applied without the traffic loading, the SFT is in a state of equilibrium. The tether pretension forces then balance the system and cause the displacements at tether numbers 2 up to 8 to approach zero. In Figure 6.3 this can be observed for 4 types of end-joints, where the hinged joint causes the largest displacements near the transition structure and the monolithic joint the smallest. The upward displacement is caused by the buoyant force which is the dominant line load. Displacements at the first and last tether are 3.5 (monolithic) upto 5.5 (hinged) times as large as the middle displacements. This is caused by the lack of a downward force at the transition structure ($x=250$ and $x=1250$ m), as is present at every tether due to the pretension forces, but not at the end-joint.

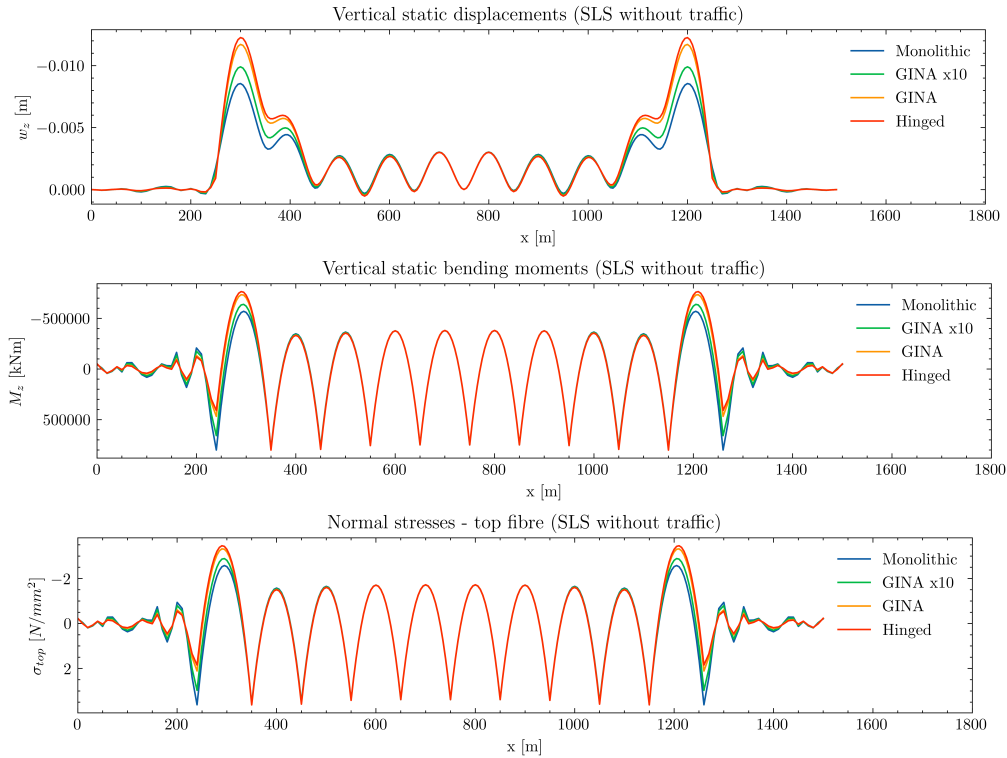


Figure 6.3: Static displacements, bending moments and stresses - SLS without traffic

When the full SLS load is applied, displacements increase downward. The line load is still aimed upward, but is decreased due to the traffic loading. The downward pretension forces at the tethers dominate the displacements in this load case. The monolithic end-joint again causes the lowest upward displacements near the transition structure, followed by the GINA x10, GINA and hinged end joints. The type of end-joint has no influence on displacements between $x = 400$ and 1100 meters.

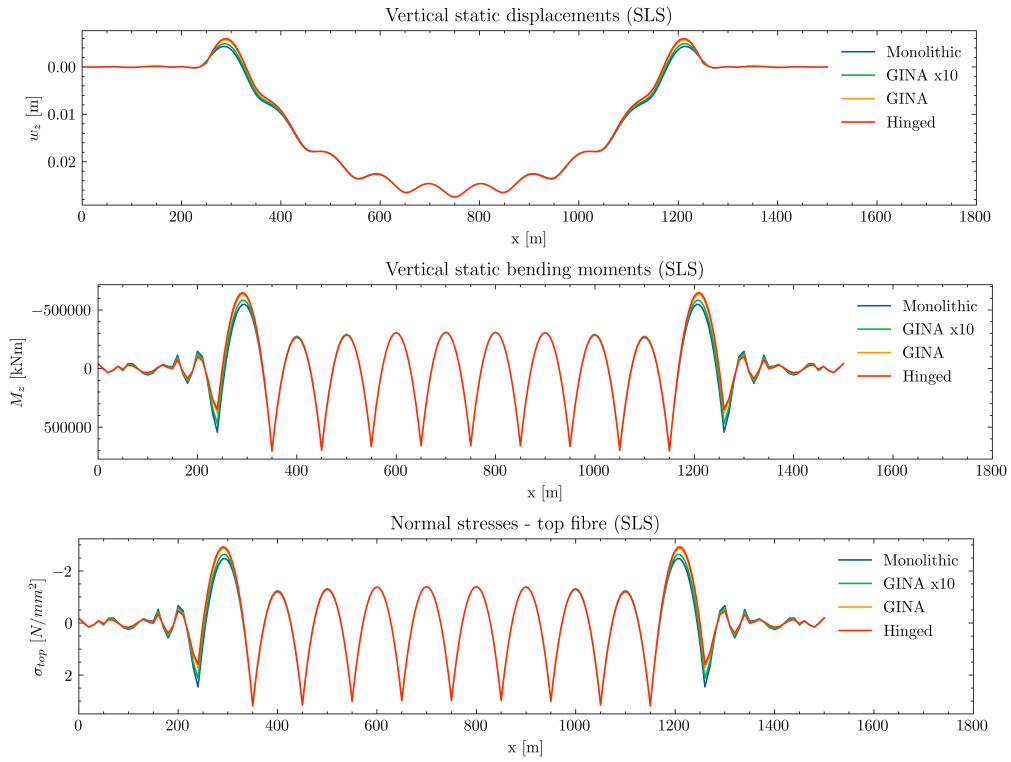


Figure 6.4: Static displacements, bending moments and stresses - SLS

Applying the ULS load ($ULS_{6.10b}$) further decreases the upward line load, causing even larger vertical deflections downward. The peak deflection (at $x=750$ m) reads 52.8 mm for all end-joints. The differences between the end joints are negligible, because for the monolithic and GINA end-joints the curvature approaches zero. The result is that the bending moments are near zero at the transition structure for all joints. Hence, the bending moment and shear force lines are similar, as can be seen in Figure 6.5. It is remarkable that static stresses in ULS (2.8MPa) are below the SLS (without traffic) stresses (3.5 MPa). This is caused by a reduced upward line load in ULS compared to SLS without traffic.

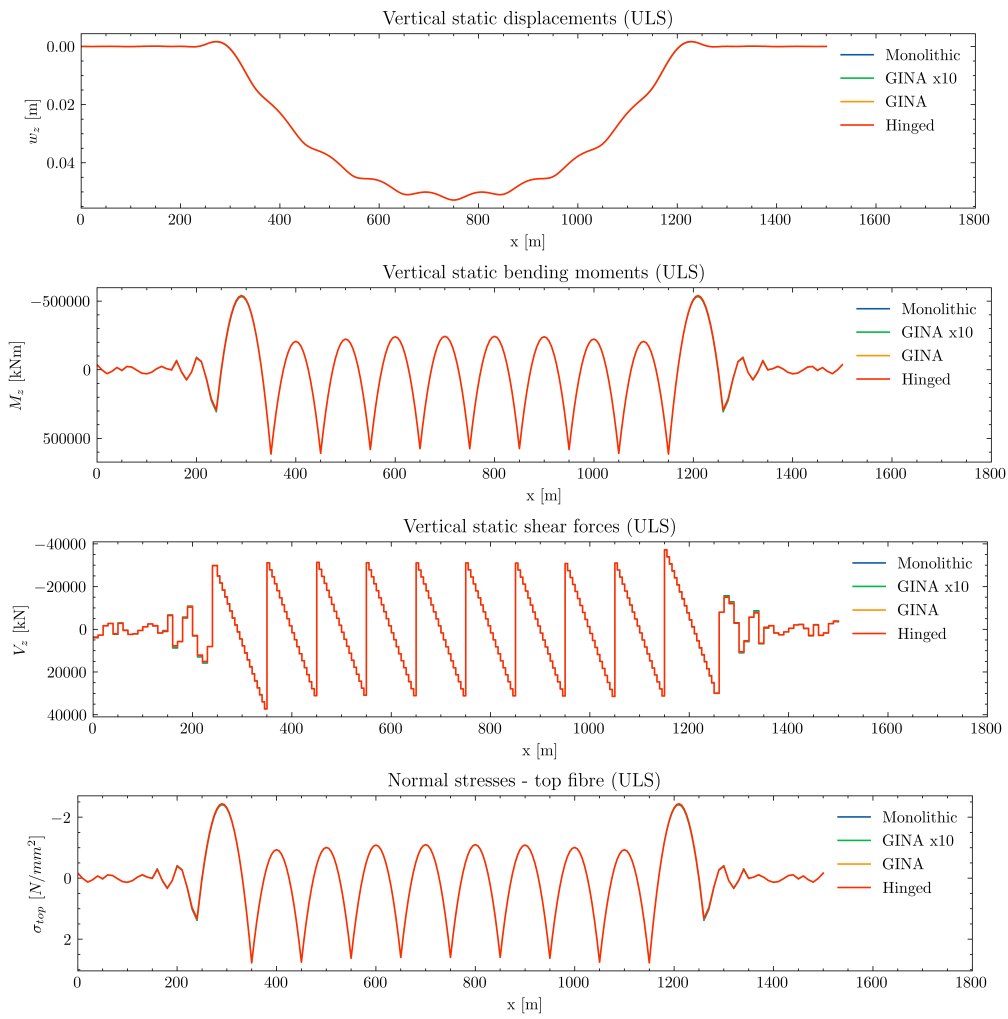


Figure 6.5: Static displacements & internal forces - ULS

6.2 Dynamic behavior

Where the static behavior in the previous section was governed by loading in only one direction (vertical), dynamic behavior differs in all 3 directions inside the SFT: longitudinal, horizontal (transverse) and vertical (transverse). In this section, the structural dynamic characteristics are clarified per direction. For every direction first the Fourier spectra of the 3 earthquake signals are presented, together with the natural frequencies for 2 different end-joints and the eigen modes. From these figures it will become clear if the natural frequencies overlap with the earthquakes most relevant frequencies. If so, this will amplify the vibrations of the SFT. Next, the results of the analysis of the 3 different signals and 5 joints are presented for the load case where all supports are excited in a synchronous manner. Finally, the study of each direction ends by exciting the structure as if it was hit by a longitudinally passing earthquake.

6.2.1 Longitudinal dynamic behavior

In the x-direction the tunnel and SFT act relatively stiff compared to the transverse directions. This is due to the rod action, which acts stiffer than the transverse beam in y and z. The land tunnel longitudinal motion is partially restricted by the soil, while at the SFT it can move freely. The water has no influence on the tunnel in x-direction, but the soil is modelled as a continuous spring along its length and only allows small displacements.

6.2.1.1 Natural frequencies & modes (longitudinal)

The stiff rod action results in relatively high natural frequencies, especially when the structure has rigid end-joints in longitudinal direction. This is the case with the monolithic and hinged joint. With a rigid connection the fundamental natural frequency is $1.2Hz$, causing it to be near the peak of the Van and Derince spectrum (Figure 6.8). A flexible connection (a form of seismic base isolation) can be added at the transition structure by means of a GINA profile. Other more or less flexible profiles can be developed as well, to adapt the stiffness to the desired amount. It should be noted that the profile must be in compression at all times, such that no gapping can occur at the end-joint. In this experiments, other profiles have been used that are 10x more or 10x less rigid than the GINA profile (see GINA x10 and GINA /10 joints). This can alter the natural frequencies in a desirable way. In Figure 6.9 it can be observed that the fundamental natural frequency has shifted down to $0.2Hz$ by applying a GINA /10 joint. This is of a positive influence as the fundamental eigen period shifts past the dominant earthquake periods.

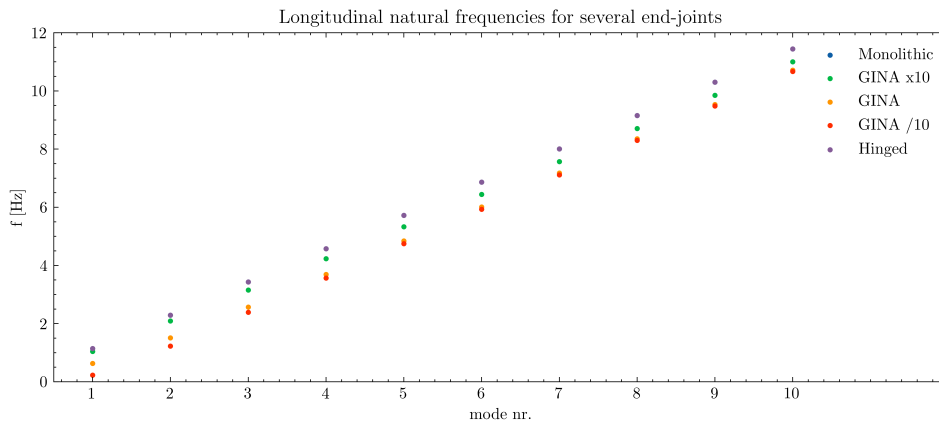


Figure 6.6: Longitudinal eigen frequencies for several end-joints

The first 7 eigen modes are displayed in Figure 6.7. These modes are of the global type, where the (dimensionless) displacements are greatest at the SFT inbetween $x=250$ and $x=1250m$. The shapes at the SFT are a half sine (mode 1) uptil 3.5 full sines (mode 7), while the shape at the land tunnel matches the these shapes and the boundary and interface conditions. For all first 7 modes, the shape at the landtunnel exists of 1.5 full sines. For the hinged end-joint, the rotations are not similar at left and right side and displacements are non-zero.

In Figures 6.8 and 6.9 the natural frequencies of the rigid and flexible end-joints are plotted over the Fourier transform of the primary horizontal acceleration spectrum. Here is visible that for the Bingol spectrum, the fundamental eigen frequency is in front of the strong earthquake frequencies

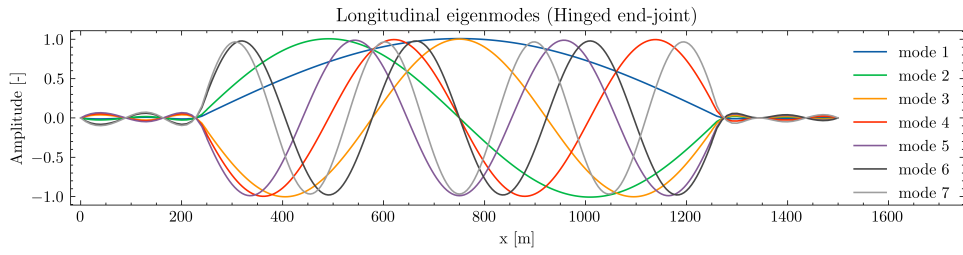


Figure 6.7: Longitudinal eigen modes (hinged end-joint)

at all time. For the Van spectrum, the shift has (presumably) a significant impact, as ω_1 is in front of the dominant frequencies. However for the Derince spectrum, the low frequencies have a higher contribution in terms of the total seismic energy. Here, shifting down the fundamental frequency by means of a flexible joint, lets it still intersect with the most dominant earthquake frequencies around $\omega = 1 \text{ rad/s}$.

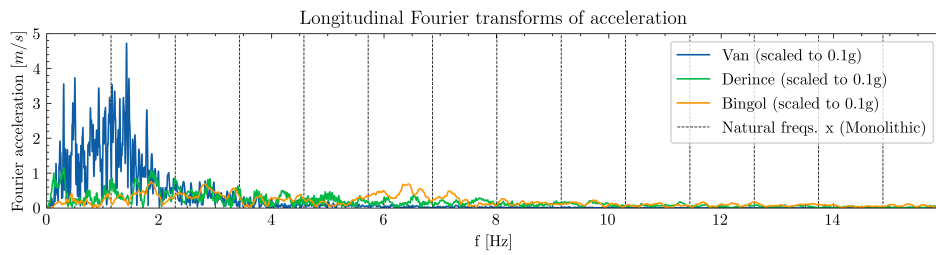


Figure 6.8: Longitudinal Fourier transform & Natural frequencies of horizontally rigid joints

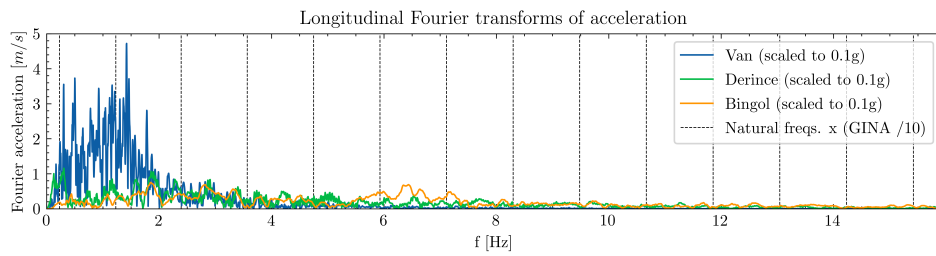


Figure 6.9: Longitudinal Fourier transform & Natural frequencies of horizontally flexible joint (GINA/10)

6.2.1.2 Results - Longitudinal synchronized support excitation

In this subsection the results of the longitudinal synchronized support excitation are presented for the Bingol, Derince and Van spectra (scaled to 0.1g). In this and following sections, the results are displayed in the form of surface plots with the spatial coordinate x (m) on first horizontal axis, time (s) on the second horizontal axis and the presented parameter on the vertical axis. All displacement results are displayed for $0 \leq x \leq 1500m$ (the full land-tunnel and SFT system), whereas the force results are displayed for $250 \leq x \leq 1250m$ (SFT system only). The forces in the land-tunnels are several factors higher than those in the SFT, due to the stiff soil springs that interfere with the even stiffer land tunnels. Besides this the main interest of this thesis is the behavior of the transition structure, which can be described based on the forces and displacements at $x = 250$ and $1250m$. Thus, for the sake of readability it is chosen to present the force results at the SFT only.

In Figure 6.10 below, the longitudinal displacements are presented for the Bingol (a), Derince (b) and Van (c) earthquake signals. As can be seen for all three signals, the displacements are greatest at the outer ends ($x = 0$ and $x = 1500m$) where the boundary conditions are set to have displacements equal to the prescribed earthquake (equivalent) displacements. The dynamic soil springs on the other hand, are much less rigid ($k_{xx} \sim 10^7 kN/m$). This causes the displacements of the land tunnel to decrease towards the transition structure, as the tunnel-soil stiffness ratio is much higher here than at the outer ends. Near the SFT mid span another, much lower peak can be observed in the longitudinal displacements of all signals. Van has the largest longitudinal displacements at mid span of 6.54 mm, while the Bingol and Derince displacements are below 1 mm.

It is remarkable that while all signals have an equal PGA of 0.1g, Bingol shows significantly lower displacements (10.61mm) than the Derince (64.00mm) and Van signal (41.70mm). This result can be explained by the much lower longitudinal Fourier acceleration peaks in the Bingol spectra that intersect with the structures natural frequencies (see Figure 6.8). The Derince Fourier spectrum has lower peaks, but many dominant earthquake frequencies that intersect with natural frequencies. The Van Fourier spectrum has fewer intersections but a very large peak intersecting with first natural frequency for the monolithic end-joint. This causes Van and Derince to have a greater impact on displacements than Bingol.

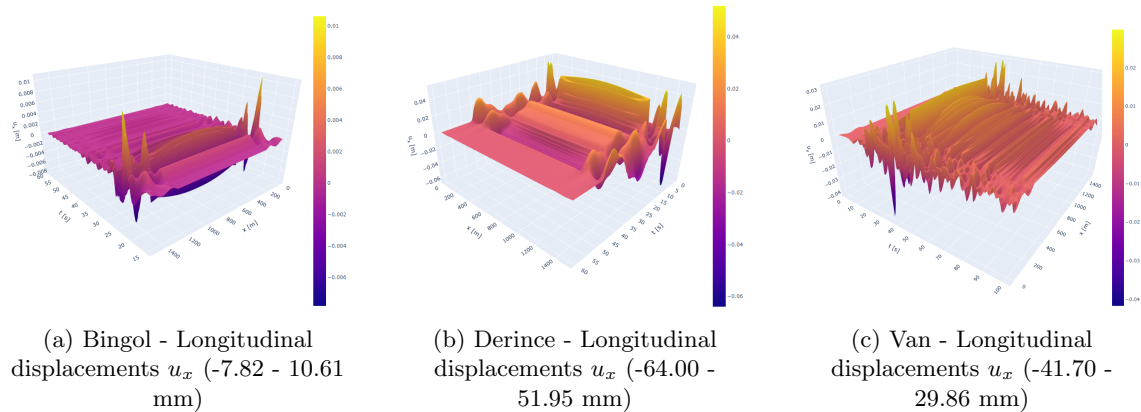


Figure 6.10: Longitudinal displacements of Bingol (left), Derince (middle) & Van (right) - monolithic end-joint - synchronized loading

Normal forces are presented in Figure 6.11 for Bingol (a), Derince (b) and Van (c). The normal forces can be seen to be zero at midspan for all synchronized support excitations. This is to be expected when a longitudinal symmetric structure is excited with a load applied symmetrically as well. The peaks occur at the transition structures, with Van showing the largest Normal forces (175, 247.3kN), followed by Derince (59, 558.7kN) and Bingol (33, 615.1kN). The transition structure and first 100 m of SFT thus carry the heaviest load in terms of normal forces.

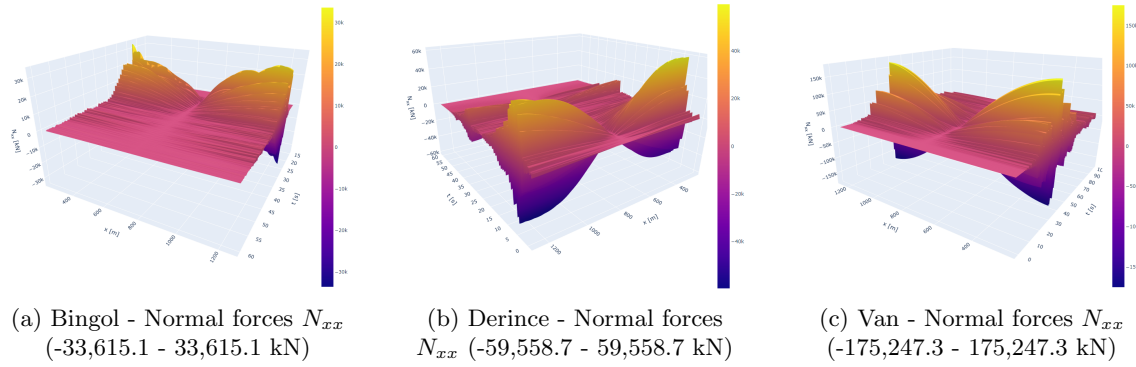


Figure 6.11: Normal forces of Bingol (left), Derince (middle) & Van (right) - monolithic end-joint - synchronized loading

6.2.2 Vertical dynamic behavior

In z-direction, the SFT behaves more flexible than in x-direction, but less flexible than in y. The beam action allows for moderate size displacements, as the structures displacements are restricted by the relatively stiff tethers. The soil limits the displacements at the land tunnels in a more rigorous manner and the water causes an increased inertia (added mass) for the SFT, which shifts the natural frequencies down. The damping effect is not visible in the modes or natural frequencies, but is taken into account in the Frequency domain analysis.

6.2.2.1 Natural frequencies & modes (vertical)

The tethers have a distinct influence on the SFT, as the increase in vertical natural frequencies is significant compared to the situation without tethers. In Figure 6.12 the natural frequencies have been plotted for 5 different end-joints, varying in rotational stiffness. Here it can be observed that the type of end-joint is of minor importance for the vertical natural frequencies. Differences between end-joints however increase at higher frequencies. Where the longitudinal eigenfrequencies had a linear relationship between the mode nr and the eigen frequency, this relationship is exponential for the vertical and horizontal natural frequencies. The mode shapes in Figure 6.13 are different of those of a beam with "hinged-hinged" boundary conditions (in case of no tethers). The first mode shape is not a half sine, but of a more "pointy" shape, caused by the increased tether stiffness near the land-connection. In the 4th until 7th mode shape, an increased amplitude near the end-joints is visible. This will cause larger amplitudes near the transition structure in case their respective frequencies are excited.

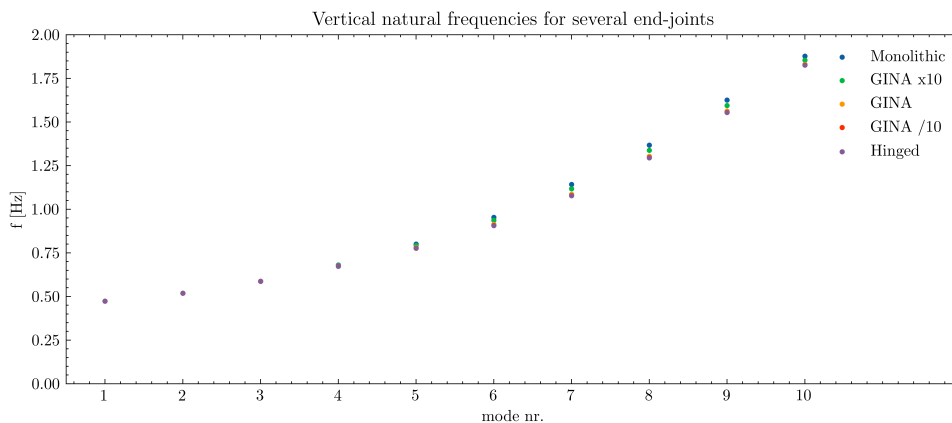


Figure 6.12: Vertical natural frequencies for several end-joints

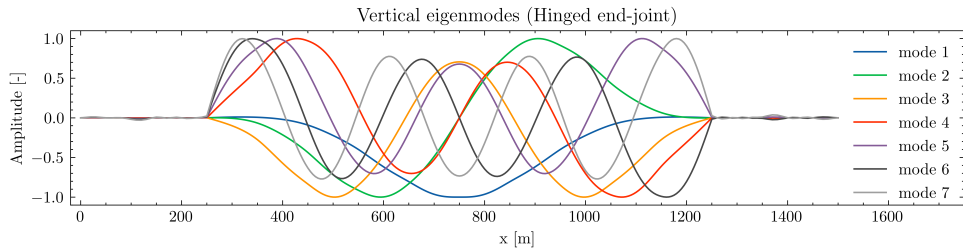


Figure 6.13: Vertical eigenmodes (hinged end-joint)

In Figures 6.14 and 6.15 the Fourier transforms of the 3 vertical earthquake signals is plotted together with the vertical natural frequencies of the SFT. Here it is again visible that the choice of joint is of minor importance for the values of the natural frequencies. However, the fundamental frequency is very close to peaks in the Van spectrum, so possibly other measures must be taken in case of large displacements or internal forces.

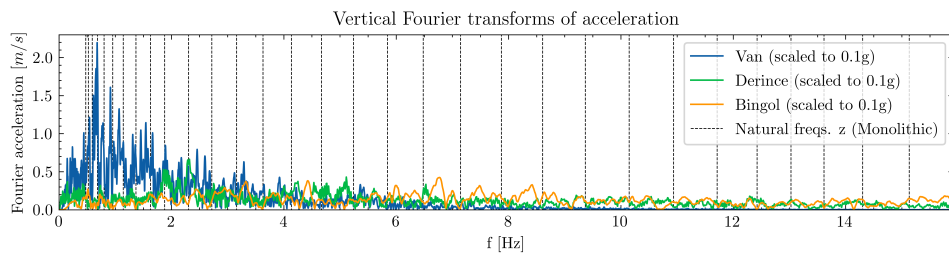


Figure 6.14: Vertical Fourier transform & Natural frequencies of monolithic end-joint

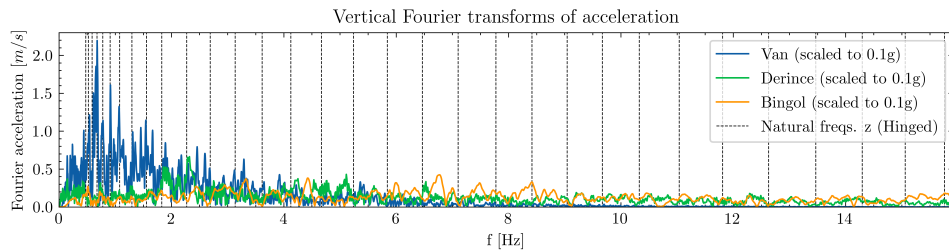


Figure 6.15: Vertical Fourier transform & Natural frequencies of hinged end-joint

6.2.2.2 Results - Vertical synchronized support excitation

In this subsection the results of the vertical synchronized support excitation are presented for the Bingol, Derince and Van spectra (scaled to 0.1g). In Figures 6.16 (Bingol), 6.17 (Derince) and 6.18 (Van) the results are presented in the order from left to right: vertical displacements w_z (m), vertical bending moments M_{zz} (kNm) and vertical shear forces V_{zz} (kN).

The displacements are all excited in different spatial patterns, depending on the modes that are excited by the earthquakes Fourier spectrum. Bingol and Van show the largest displacement at mid span, however Van has also has peaks (only slightly lower) at the 3th and 8th span. Derince is clearly excited by the higher modes as well, that increase the amplitude near the transition structure. This causes the largest displacement to occur at the 1th and last span for Derince (73.10 mm). Bingol and Van show peak displacements at mid span of 9.38 and -50.00 mm.

Vertical bending moments M_{zz} are displayed in Figures 6.16(b) (Bingol), 6.17(b) (Derince) and 6.18(b) (Van). All vertical bending moment diagrams have in common that the peaks occur at the end-joint when a monolithic joint is applied. On the other hand the patterns are very different, as the displacement patterns as described in the previous paragraph have many differences as well. Derince shows relatively low bending moments between the 2th and 9th span, caused by the large displacements that occur especially at the 1th and 10th span, where the stiffest (and shortest)

tethers are located and near the the rigid monolithic joint. Bingol and Van show peaks in bending moments at the tether connections or amid the tethers. All field moments however are below the support bending moment caused by the monolithic joint, with -297.3, 3362.0 and -1520.7 MNm for Bingol, Derince and Van respectively. For other more flexible joint types the support moments decrease and field bending moments become normative.

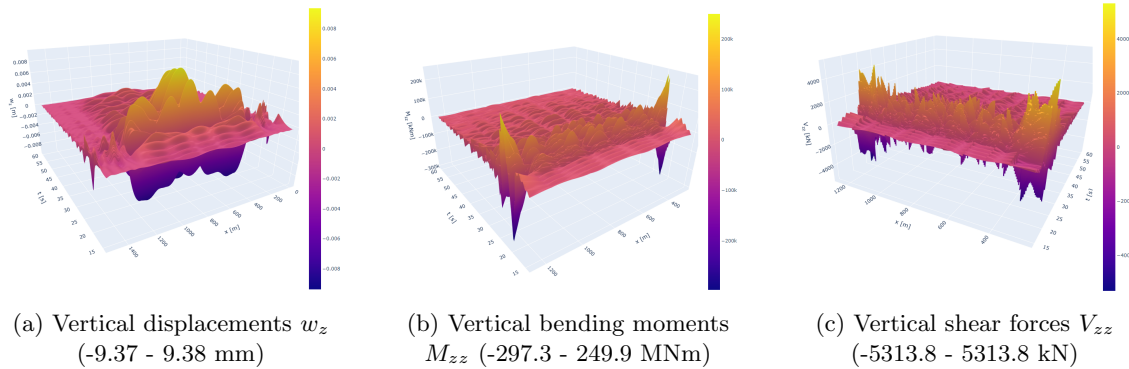


Figure 6.16: Vertical results (Bingol) - monolithic end-joint - synchronized loading

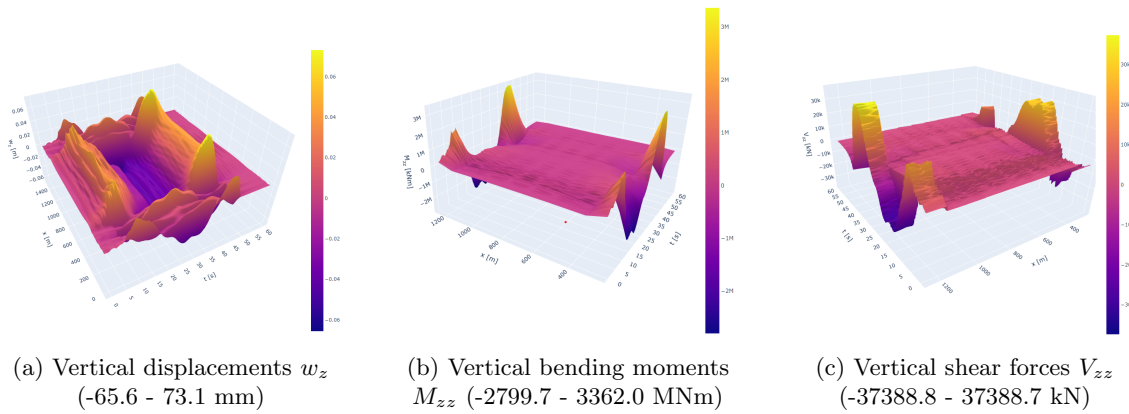


Figure 6.17: Vertical results (Derince) - monolithic end-joint - synchronized loading

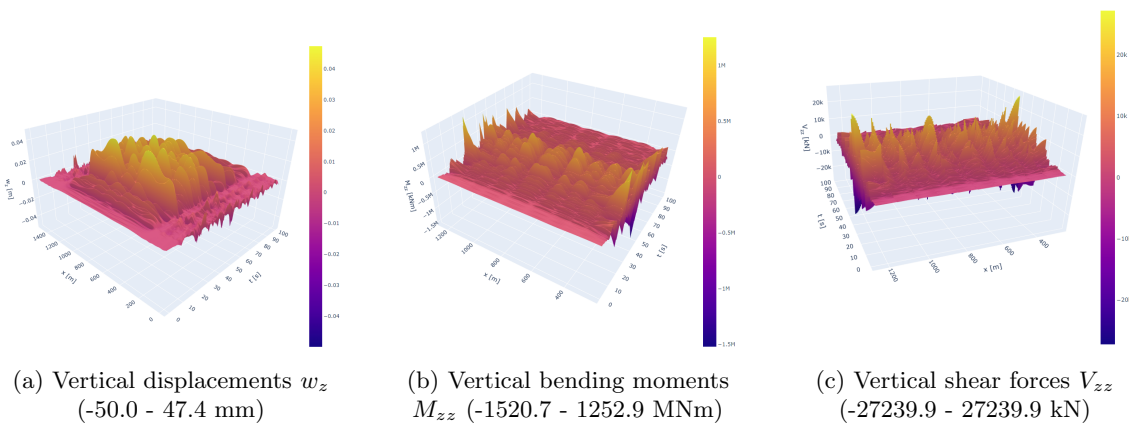


Figure 6.18: Vertical results (Van) - monolithic end-joint - synchronized loading

The shear forces as displayed Figures 6.16(c) (Bingol), 6.17(c) (Derince) and 6.18(c) (Van), show peaks at the tether supports and have the largest peak at the monolithic end-joint. The shear forces at the Derince tether supports are relatively low compared to those at the end-joints at the 1th and last tether. The rigidity of these connections is so high that when the large displacement at the 1th and 10th span occur, it extremely amplifies the magnitude of the shear force. For the other signals (Bingol and Van) the displacements near the end-joints are lower than at mid span,

while the rigidity of the tethers grows towards the mid span. This causes the shear force peaks to be more evenly distributed over the length. The largest values however occur at the (monolithic) end-joint with 5,313.8, 37,388.7 and 27,239.9 kN for Bingol, Derince and Van respectively.

6.2.3 Horizontal dynamic behavior

The last direction to discuss is the horizontal transverse y -direction. This is the most flexible direction, because the SFT is only secured diagonally by means of relatively flexible mooring lines. These lines start to add more stiffness when displacements grow larger, since the lines have a sag of several meters. The non-linear stiffness is linearized for small displacements ($w_y \leq 0.5m$) and will have a low stiffness. Hence, the mooring lines are of minor influence for the dynamic behavior of the SFT. The land tunnels are restricted by the soil in horizontal direction, as the soil adds stiffness in the form of distributed springs. The effect of the water is taken into account by the added mass, which lowers the natural frequencies. The damping effect of the water (accounted for using the Morison equation), is not used for calculating the natural frequencies and eigen modes, but is of large influence for the results of the frequency domain analysis.

6.2.3.1 Natural frequencies & modes (horizontal)

The natural frequencies are displayed in Figure 6.19, and are rather similar for all end joint-types. The choice of the end-joint thus has little influence on the horizontal eigen frequencies, similar to the effect that has been observed for the vertical eigen frequencies. The horizontal modes of the SFT are similar to the modes of a hinged-hinged Euler-Bernoulli beam (without mooring lines), with a half sine for mode 1, upto 3.5 full sines for mode 7 (see Figure 6.20). In other words, the mooring lines hardly alter the mode shapes. The type of end-joint on the other hand, does influence the mode shape continuity at the transition between SFT and land tunnel.

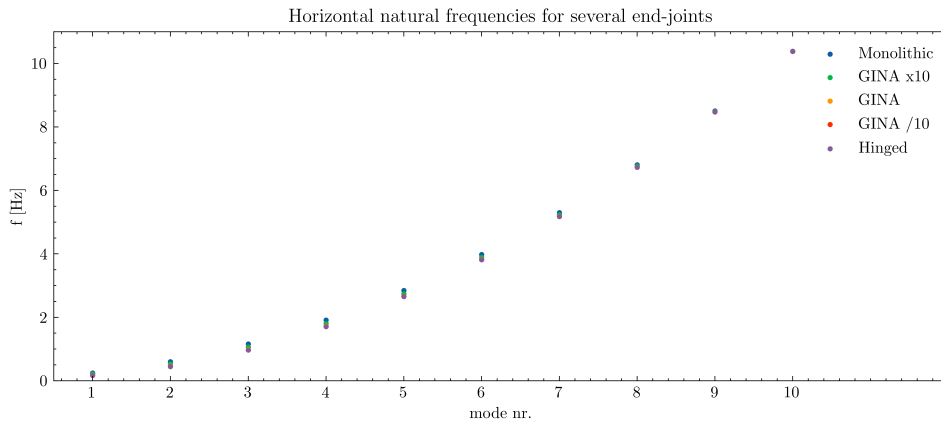


Figure 6.19: Horizontal natural frequencies for several end-joints

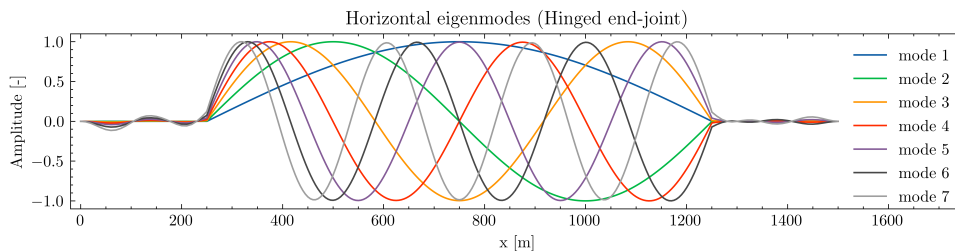


Figure 6.20: Horizontal eigenmodes (hinged end-joint)

The fundamental natural frequency is intersecting with the dominant frequencies of the secondary horizontal Van and Derince Fourier spectra. The rotational stiffness of the end-joint has little influence on the natural frequencies, as can be seen in Figures 6.21 and 6.22. Other possibilities to shift the fundamental natural frequency will be discussed later.

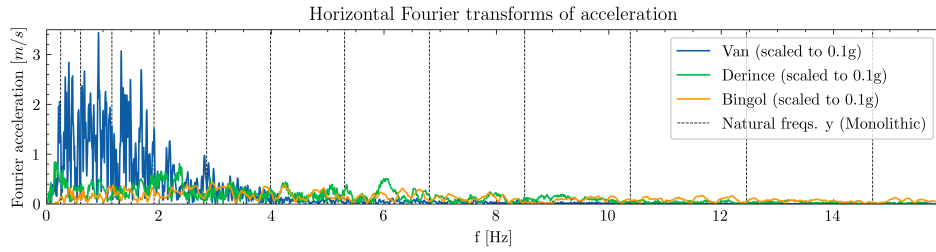


Figure 6.21: Horizontal Fourier transform & Natural frequencies of monolithic end-joint

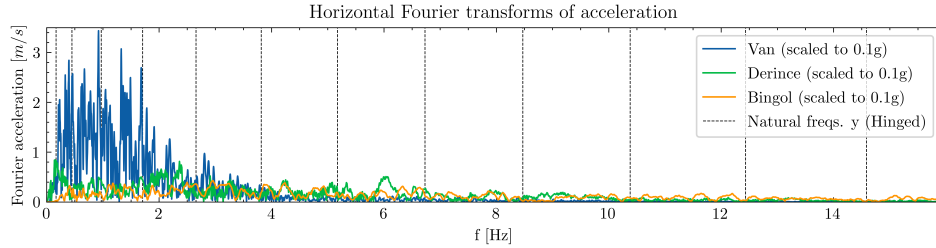


Figure 6.22: Horizontal Fourier transform & Natural frequencies of hinged end-joint

6.2.3.2 Results - Horizontal synchronized support excitation

In this subsection the results of the horizontal synchronized support excitation are presented for the Bingol, Derince and Van spectra (scaled to 0.1g). In Figures 6.23 (Bingol), 6.24 (Derince) and 6.25 (Van) the results are presented in the order from left to right: horizontal displacements w_y (m), horizontal bending moments M_{yy} (kNm) and horizontal shear forces V_{yy} (kN).

The horizontal displacement diagrams of Bingol, Derince and Van show many similarities, due to displacements mainly occurring in the 1th (half sine) mode shape. In the Bingol displacement diagram (Figure 6.23(a)), also some signs of the 3th mode shape can be found, but other than that, the 1th mode is dominant for all horizontal displacements. This can be explained by the fact that the mooring lines add very little stiffness horizontally, so the SFT can move with less restraints in horizontal than in vertical direction. The 1th mode shape needs the least amount of bending energy, and therefore the structure is prone to move in this mode. The magnitude of the horizontal displacement is greatest for Derince (554.2mm), followed by Van (-528.1mm) and lowest for Bingol (-40.0 mm).

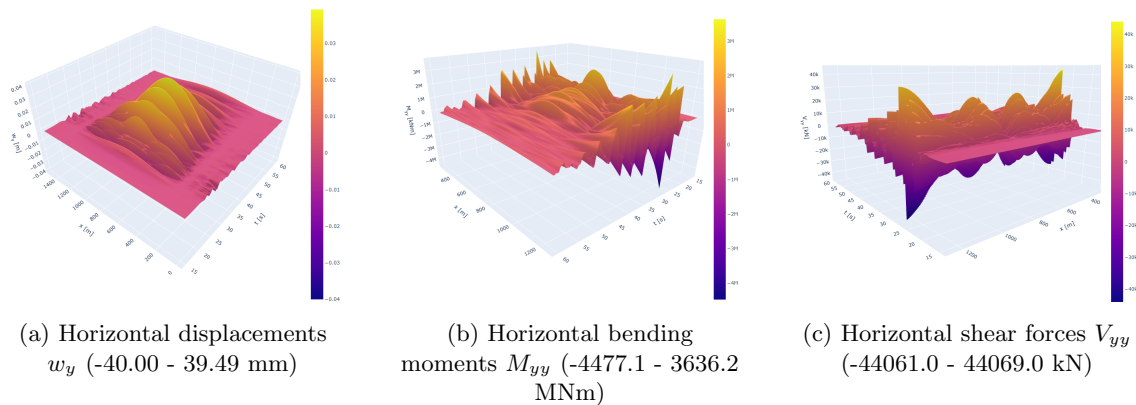


Figure 6.23: Horizontal results (Bingol) - monolithic end-joint - synchronized loading

The horizontal bending moments in Figures 6.23(b) (Bingol), 6.24(b) (Derince) and 6.25(b) (Van) show the largest values at the transition structure ($x = 250$ and $1250m$) in case of the monolithic end-joint. The peaks at the end joint are -44,771.1, 17,793.7 and 28,255.4 MNm for the Bingol, Derince and Van signals respectively. The field bending moments at mid span occur at approximately $\frac{2}{3}$ of the end-joint moment for Bingol and Van. For the Derince signal the field bending moment appears at 16,516.1 MNm, thus only -7.18% below the end-joint moment.

The horizontal shear forces in Figures 6.23(c) (Bingol), 6.24(c) (Derince) and 6.25(c) (Van) are all zero at mid span (for the synchronized support excitation) and increase towards their maximum values at the end-joints. The peak shear forces at the end-joints are 44069.0 kN for Bingol, 85863.5 kN for Derince and 154044.1 kN due to the Van signal. At the mooring lines ($x = 450, 650, 850$ and $1050m$) small jumps in the shear-force diagram can be seen due to the tensile forces the mooring lines add to the system. In the Derince shear force diagram (Figure 6.24(c)) larger jumps in the shear forces are observed near the land-connection, as the displacements at the first two spans are here relatively larger compared to the max displacement at mid span. This large displacement at the more rigid 1th mooring line results in larger jumps in the shear forces.

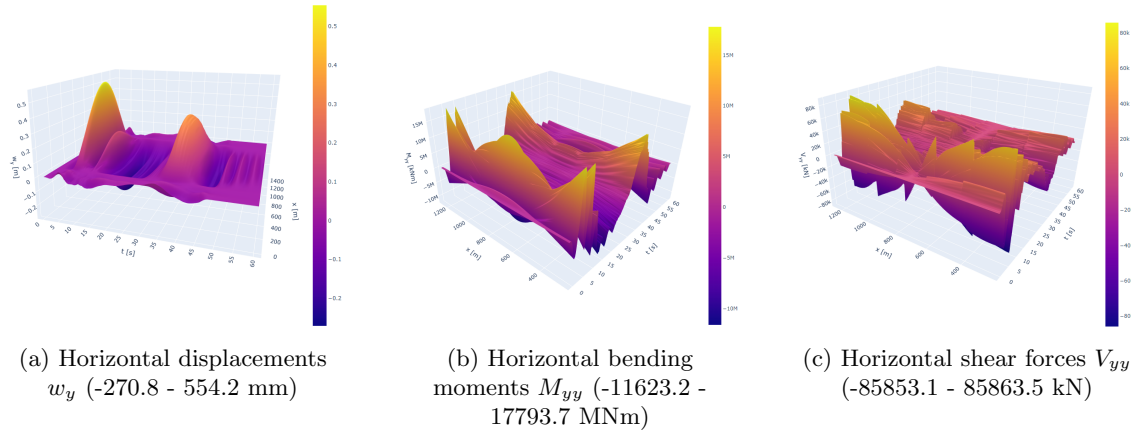


Figure 6.24: Horizontal results (Derince) - monolithic end-joint - synchronized loading

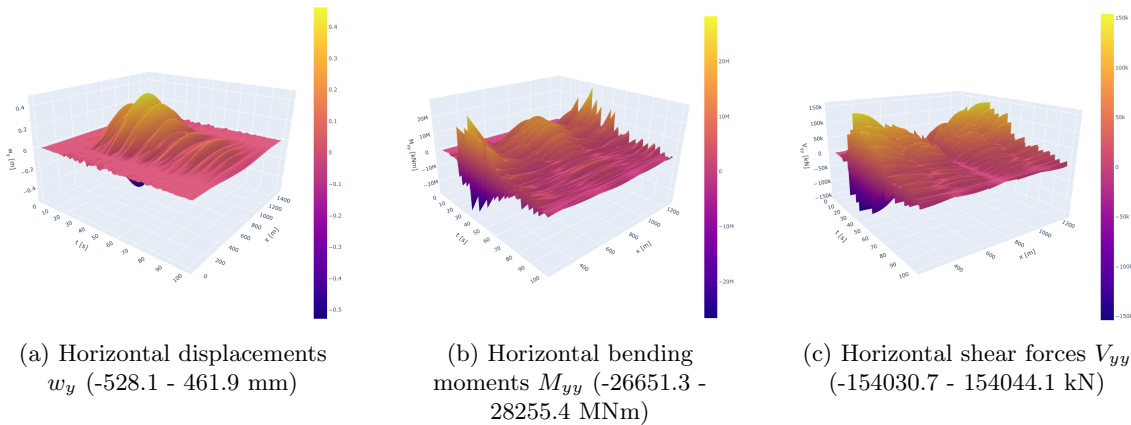


Figure 6.25: Horizontal results (Van) - monolithic end-joint - synchronized loading

6.2.4 Evaluation of the synchronized results

In this section the results of the synchronized analyses are presented.

6.2.4.1 Effect on modes

The variation of the end-joint characteristics changes the mode shapes in all directions. In this subsection the most flexible end-joint mode shape is compared to the most rigid mode shape for the x, y and z direction.

In Figure 6.26 it can be seen that for the vertical and horizontal transverse modes there is continuity of rotation at the end-joint. Comparing this to the vertical and horizontal hinged modes in Figure 6.27, it is visible that the rotation is discontinuous. The curvature of the modes in Figure 6.26 is slightly different compared to the flexible modes in Figure 6.27 and slightly more displacements are visible at the land tunnels. For the longitudinal modes of the hinged & monolithic end-joints there is continuity of displacements for all joint types. For the longitudinal modes with seismic base isolation discontinuities can be observed in displacements at the end-joint in Figure 6.27(a). These are the only mode shapes that are cosine shaped, whereas all other modes have sine shaped modes.

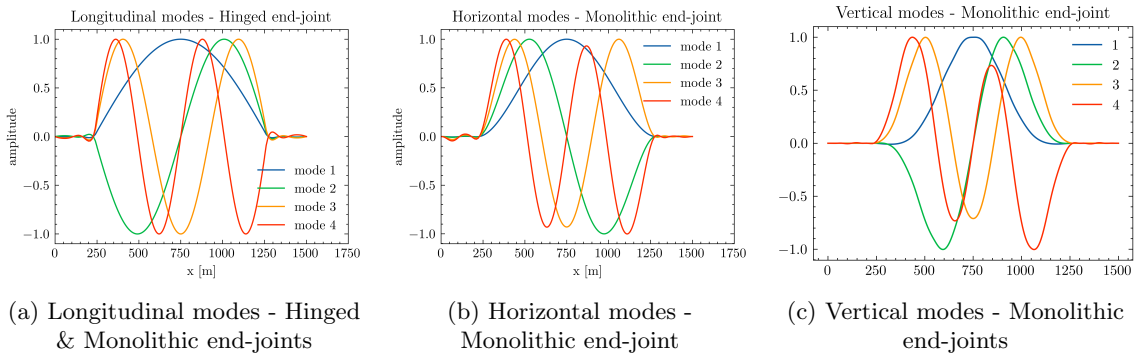


Figure 6.26: Modes of most rigid end-joint types in longitudinal, horizontal and vertical direction

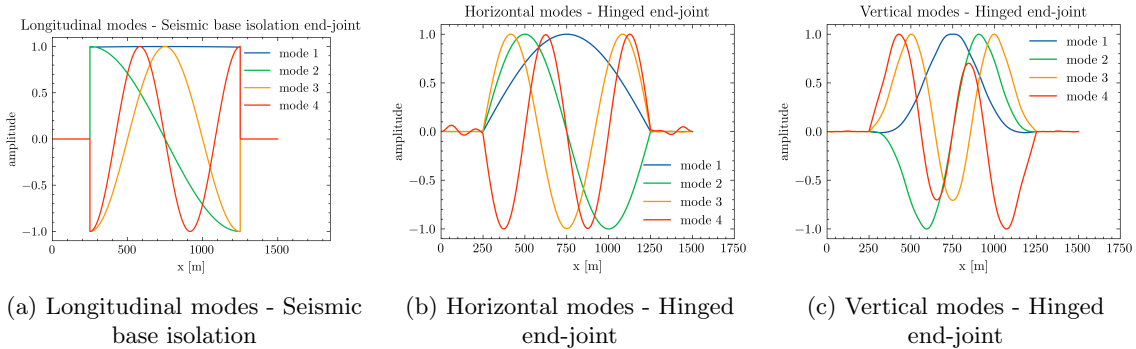


Figure 6.27: Modes of most flexible end-joint types in longitudinal, horizontal and vertical direction

6.2.4.2 Effect on SFT displacement

Derince is the normative signal for SFT displacements, with largest displacements in vertical as well as in horizontal direction. For the monolithic connection, vertical displacements are found between $-65.6 \leq w_z \leq 73.1\text{mm}$ (see Figure 6.17) and horizontal displacements between $-270.8 \leq w_y \leq 554.2\text{mm}$ (see Figure 6.24). Displacements can drastically be reduced by applying a hinge or rotation spring in y and z direction at the transition structure. Reductions of displacements in vertical direction of 37.1% and 83.9% in horizontal direction are obtained with the GINA/10 and hinged joints. This is due to a shift in the natural frequencies (see Figure 6.28). The shift of horizontal natural frequencies causes the 4th natural frequency to no longer intersect with the peaks of the spectrum. The first natural frequency does shift to a peak, but at a (almost static) frequency of 0.2 Hz approximately. This does not seem to cause too large displacements. In vertical

direction the 7th and 10th natural frequency move away from peaks in the acceleration spectrum as well.

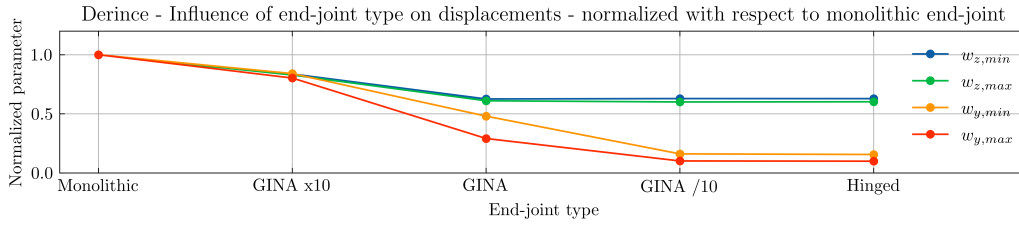


Figure 6.28: Derince - Influence of end-joint on displacements (relative to the monolithic joint)

The reduced displacement in the Derince spectrum is not a guarantee that a GINA/10 end-joint will always induce lower displacements. In horizontal direction the response to all signals was reduced with 75% or more, although in vertical direction the GINA/10 and Hinge joints cause up to 10% higher vertical displacements for the Van and Bingol earthquake. In Figure 6.29 it is visible that a slight shift of the natural frequencies can let the structure be excited with considerably lower Fourier accelerations. But this is very much dependent on the Fourier spectrum of a signal, and these have a large amount of randomness for earthquakes.

According to Eurocode 2 ([NEN-EN 1992-1-1, 2011](#)) the serviceability of a structure is no longer guaranteed when vertical and horizontal displacements are greater than $\frac{L}{250}$. Here L is the span, which for the SFT can be taken as the distance between tethers for vertical displacements and distance between mooring lines for horizontal displacements. To obtain $w_{z,max,Rd}$, the maximum vertical SLS displacement at midspan $w_{z,sls} = 0.026m$ is subtracted from $w_{z,max}$ (see equation 6.7).

$$w_{z,max} = \frac{L_{cc,teth}}{250} = \frac{100}{250} = 0.400m \quad (6.6)$$

$$w_{z,max,Rd} = w_{z,max} - w_{z,sls} = 0.400 - 0.026 = 0.374m \quad (6.7)$$

$$w_{h,max} = w_{h,max,Rd} = \frac{L_{cc,moor}}{250} = \frac{200}{250} = 0.800m \quad (6.8)$$

The Derince earthquake (scaled to 0.1g) causes vertical displacements of $w_{z,max,Ed} = 73.1mm$. This means that the maximum allowed earthquake for this would be $w_{z,max,dyn}/w_{z,max} \times 0.1g = 0.547g$ for the monolithic joint and $0.547g/0.629 = 0.869g$ for the hinged and GINA/10 joint. In horizontal direction the maximum allowed earthquake is $w_{y,max,dyn}/w_{y,max} \times 0.1g = 0.144g$ for the monolithic joint and $0.144g/0.156 = 0.923g$ for the hinged and GINA/10 joint.

All in all, for the 3 signals that are analyzed, the displacements become a problem if the earthquake is more than 0.144g. Then a hinge or flexible GINA/10 profile should be applied. When this is done, the maximum earthquake allowed with respect to displacements is 0.869g.

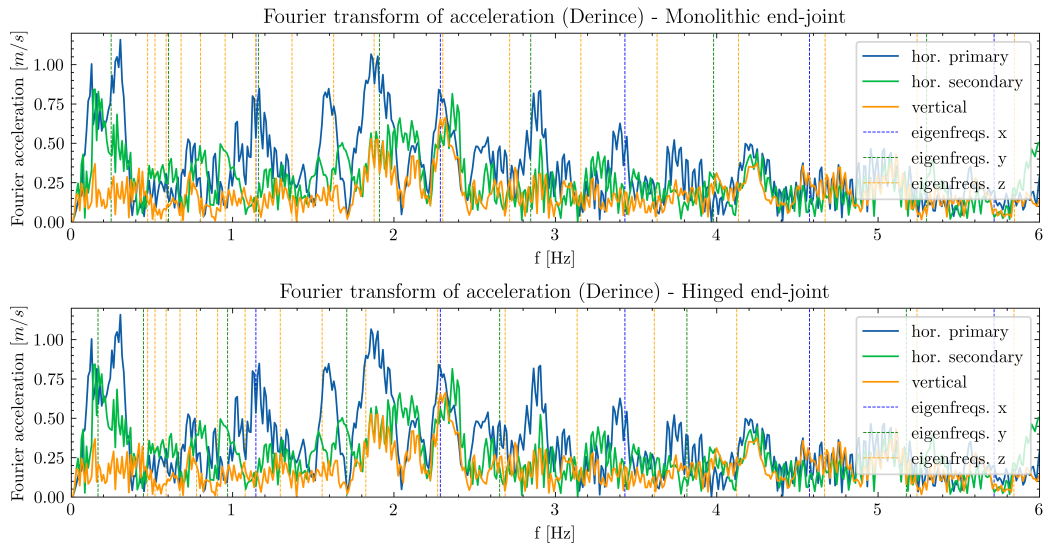


Figure 6.29: Comparison of monolithic and hinged natural frequencies with the Derince acceleration spectrum

6.2.4.3 Effect on SFT stresses

The cross-sectional performance of the SFT must be evaluated to assess if maximum stresses are not exceeded. The normal stresses are dependent on the cross-sectional forces in the three separate axes (x, y and z), which must be evaluated using Equation 6.9 to find the maximum stresses in the outer fibres.

$$\sigma_{sft} = \frac{N_{xx}}{A} + \frac{M_{zz}r_z}{I_{zz}} + \frac{M_{yy}r_y}{I_{yy}} \quad (6.9)$$

For these stresses, the surrounding stress lines are evaluated over 2 separate axes of the SFT cross-section. $\sigma_{sft,1}$ is evaluated over the line $r_y = 20m$; $-9 \leq r_z \leq 9m$, and $\sigma_{sft,2}$ is evaluated over the line $-29 \leq r_y \leq 29m$; $r_z = 0m$ (see Figure 6.30).

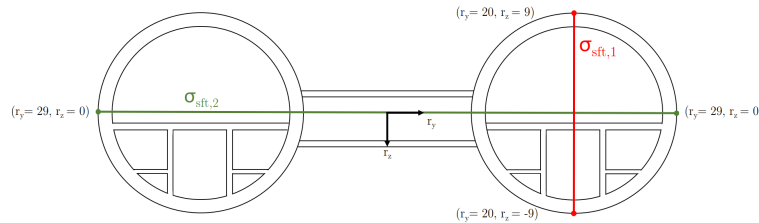


Figure 6.30: $\sigma_{sft,1}$ & $\sigma_{sft,2}$ definitions

For the 3 earthquake signals that are analysed, the Van spectrum is the normative signal with respect to normal stresses. It shows the least reduction of normal stresses after applying other types of end-joints. This can be seen in Figure 6.31(a), where $\sigma_{sft,1}$ is the normative stress parameter with peak stresses at -8.561 and 8.562 MPa.

For the seismic stresses to not exceed the cross-sectional resistance, a limit stress must be defined. The maximum amount of prestress possible in a concrete cross-section is about 11 MPa and for this study it is assumed that no tension can arise in the structure. The prestress is reduced with the maximum static stress found in Section 6.1, which is 3,5 MPa. The maximum allowed tensile stress in the structure is thus $f_{c,t} = 11 - 3.5 = 7.5 MPa$.

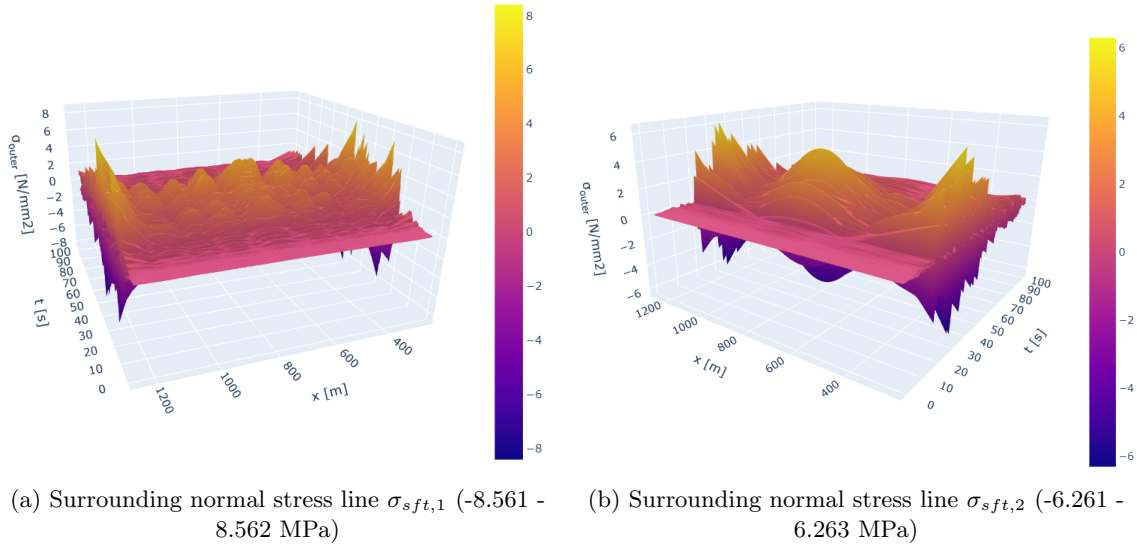


Figure 6.31: Surrounding normal stress lines (Van) - monolithic end-joint - synchronized loading

Although Van is normative after applying the best type of end joint, Derince has the highest stresses for the monolithic joint (see Figure A.1(a)), but these can be reduced with 91.3 % by applying hinged joints, as can be seen in Figure A.1(b). The stresses of the Derince spectrum show the largest peaks near the transition structure ($250 \leq x \leq 450m$), with peaks of -16.933 MPa, compared with stresses around 3 MPa in the middle of the SFT. The monolithic end-joint is not applicable in seismic areas, as the normal stress is above the maximum pre-stress limit (7.5 MPa), and the maximum PGA would be 0.044g. Applying hinged end-joints let the stress peaks still occur near $x=100m$, but at the end-joint these approach zero (as bending moments are zero there).

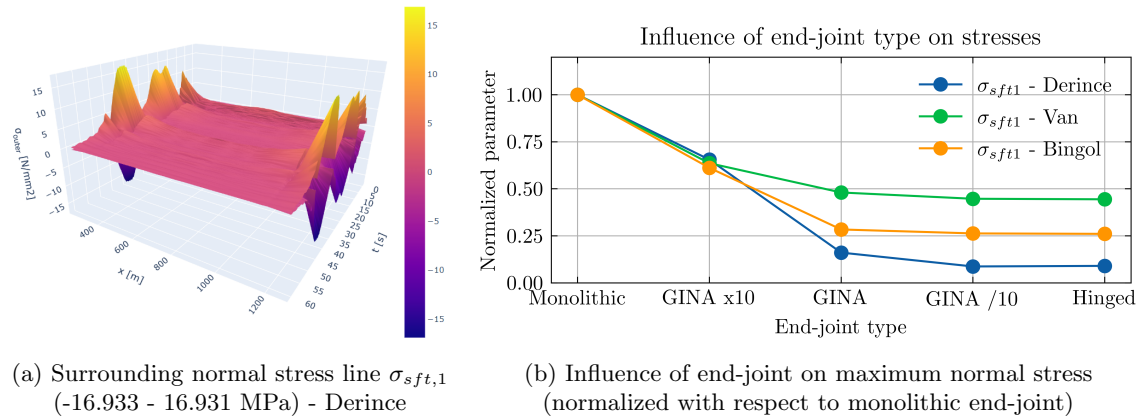


Figure 6.32

In contrast to the Derince stress results (with peaks at the end-joints), the Van $\sigma_{sft,1}$ stresses show stress peaks scattered over the length of the SFT. This means that the cross-sectional resistance should be able to resist large stresses over the full 1000 meters of SFT, instead of only over the first 200 meters (as for Derince). For the monolithic end-joint the largest stresses are located at the end-joint, while for the hinged end-joint the largest stresses occur near SFT mid span. Dependent on the choice of end joint, local high stresses can be withstand by adjusting these cross-sections. This can be done by adding extra pretension steel in the concrete tunnel cross-section or applying cross-sections out of steel or steel-concrete "sandwich" sections. However, if the stress peaks occur every 100 meters, the expensive high resistance elements must be used over the full length. This will drive up the building cost significantly.

The maximum PGA that is allowed to occur (within the three earthquake spectra with synchronized support excitation) will be based on the the earthquake that causes the largest stresses in the SFT. Next, the best performing joint will be used to calculate the maximum PGA. This is

the Van earthquake with hinged end-joint. The maximum stress that occurs for the Van spectrum (scaled to 0.1g) is $\sigma_{sft,1} = 3.734MPa$. If the tensile stress limit is set on 7.5 MPa (prestress limit reduced with static stress). Then a maximum PGA of 0.201g would be allowed. For higher PGA's a different end-joint or other cross-section (steel or steel-concrete) are the only economic solutions.

Reinforced concrete sections have a tensile stress limit of $f_{c,Rd} = 2MPa$, but stresses of 3.5 MPa are found for the static SLS loadcase. Whereas for prestressed concrete structures an additional compressive stress of 2 up to 11 MPa can be applied on the whole cross-section. This increases the tensile capacity up to 11 MPa. An amount up to 5 MPa is regularly applied for prestressed structures, whereas 11 MPa is highly exceptional and very costly. It is therefore likely that SFTs will be prestressed. A cost-benefit analysis is not part of this thesis, so the feasibility of a tunnel design that requires that much high strength steel is unclear. In case of high PGA's, alternatively full steel cross-sections and steel-concrete sandwich sections become attractive options. The steel outer shell would then be able to resist tensile stresses and offer a water proof lining for the tunnel.

6.2.4.4 Effect on tether stresses

The last prerequisite for the synchronized analysis is that the stresses in all tethers must remain in tension, and that the maximum stress remains far under the yield limit (circa 50% of $f_{y,d}$). For the Bingol and Van spectra this is feasible, since the stress differences $\Delta\sigma_{teth}$ for the 0.1g earthquakes were 42.025MPa and 220.578MPa respectively for the monolithic joint. For Derince this was $\Delta\sigma_{teth} = 378.425MPa$. In all cases the hinged end-joint causes the largest stress fluctuations in the 1th and last tether, while the monolithic end-joint allows for the lowest stress fluctuations. This is presumably caused by the fact that the monolithic connections adds more stiffness to the system near the end-joint, which causes higher bending moments there, but spares the tethers as they are less utilized. Whereas for the hinged connection, no bending moments can arise at the end-joint, so the stiffness in the first and last 200 meters of SFT must originate from the tethers. Therefore the tethers are more utilized in a SFT configuration with vertical rotation flexibility at the end-joint, then for a rigid connection.

The minimum stresses of the 0.1g Derince spectrum (Figure 6.33) show negative stresses in tether 1 for all end-joints, meaning the tethers are loaded in compression. These compressive stresses are unrealistic, because the tether will buckle when loaded in compression, causing undesirable damage to tether. Therefore another design will be chosen later in this section, such that no slack of the tethers will occur.

The results do give a good insight in which tethers have the largest stress fluctuations and what type of end-joint gives the least fluctuations. The monolithic end-joint performs best, and the hinge performs worst. The stress differences are largest near the land-connection, since the tethers act stiffer there than at mid span. This is caused by the reduced tether lengths near the land connection (72m for the 1th tether versus 200 meters at middle tether).

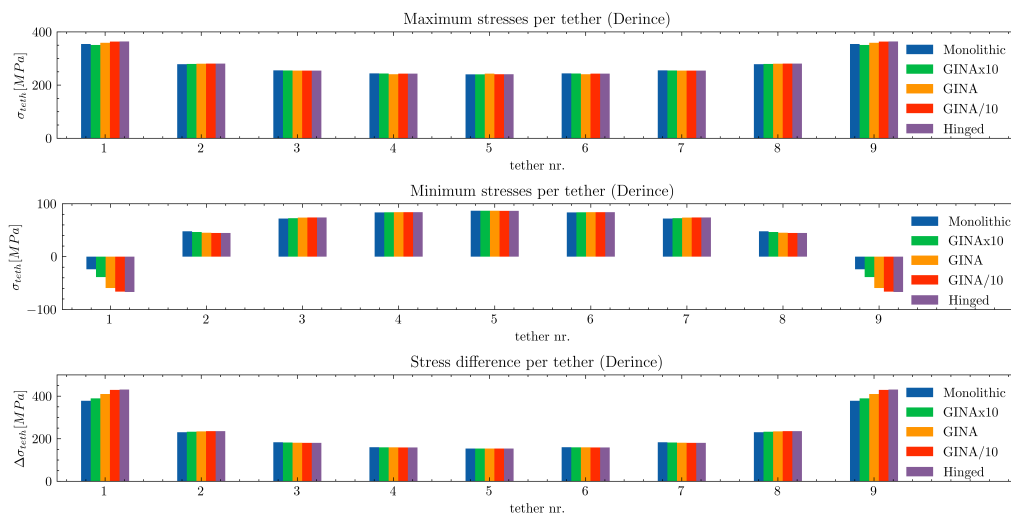
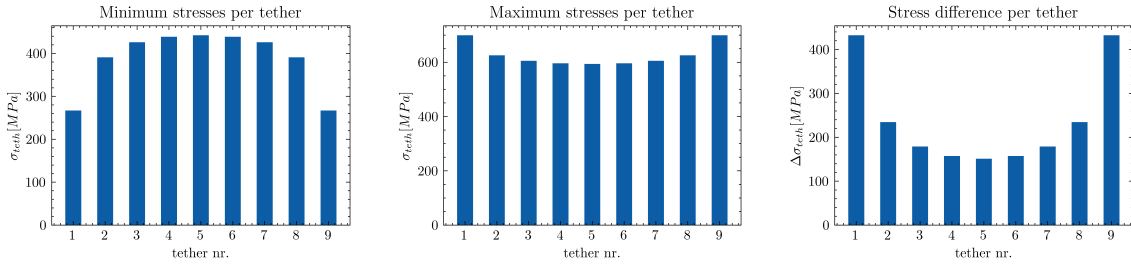


Figure 6.33: Maximum, minimum and difference of stresses per end-joint (Derince)

The configuration chosen for the parameter study does not fulfill the requirement of no com-

pressive stresses in the tethers. The stress fluctuations that occur during earthquakes can be resisted by applying a smaller tether cross-section with an equal pretension force per tether. This induces higher (pre)stresses due to the reduced cross-section, but the smaller cross-section lowers the stiffness of the tether, causing lower normal forces due to dynamic loads in the tethers. The steel quality can be increased up to values of $f_{y,d} = 1860 \frac{N}{mm^2}$ to resist the high stresses. The reducing and stimulating effects of this approach can balance, such that the stress difference stays constant, but the maximum stress will strongly increase, due to the larger static pretension force needed to support the structure.

The reduced tether approach is applied on the Derince 0.1g spectrum with the GINA/10 end-joint, since this joint has the best performance with respect to displacements and SFT stresses. For the analysis the tether cross-section is reduced for all tethers from $A_{teth} = 2 \times 0.236m^2$ to $A_{teth} = 0.150m^2$. Other parameters are kept as defined in the Case Study (Chapter 5).



(a) Minimum stresses per tether (b) Maximum stresses per tether (c) Stress difference per tether

Figure 6.34: Tether stress results of Derince 0.1g with reduced tether stiffness ($A_{teth} = 0.150m^2$)

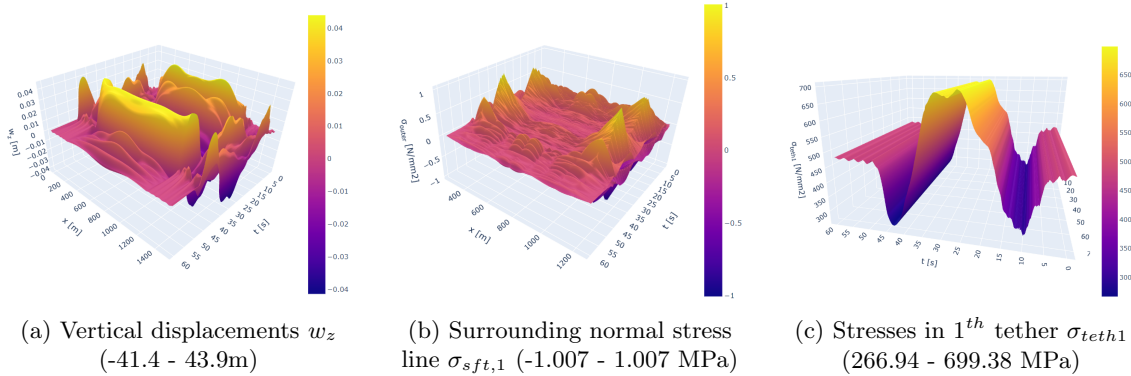


Figure 6.35: Influence of reduced tether stiffness on key parameters

The results of the "reduced tether" analysis show good performance for the key parameters compared to the original rigid tether (with GINA/10) results, as can be seen in Figure 6.35. Maximum vertical displacements remain the same with 43.9 mm max deflection for both analyses. Maximum SFT stresses for $\sigma_{sf,1}$ decrease from 1.456 to 1.007 MPa, due to decreased bending moments at the tether supports. Finally the maximum stresses in the tethers are increased (as expected) from 363.55 to 699.38 MPa, see Figure 6.34. The stress difference in the tethers has only increased slightly from 429.61 to 432.44 MPa. This adjustment comes at the cost of more expensive high strength tethers, but decreases the SFT stresses with 30.84% for this case. This indicates that less pretension steel can be applied in the SFT cross-section, and that the reduced tether (mechanically speaking) a good method to improve the SFT performance. Its economical feasibility should be investigated more in depth.

The maximum PGA for the "reduced tether" analysis is 0.181g for the chosen configuration. For higher PGA's more flexible tethers should be applied with equal pretension forces, or the tethers should be placed under an angle.

The increased vertical flexibility can also be acquired by placing the tethers in an angle with the vertical line. Here it is possible to use larger cross-sections, since the flexibility will then be

derived from the tethers ability to rotate at the seabed (instead of a reduced cross-section). This option is not elaborated up on in this thesis.

The above mentioned ways to reduce the tether stiffness do not (by definition) have to be applied at every tether. As can be seen in Figure 6.33, the largest stress differences occur at tethers 1 and 9, so optionally the tethers are only adapted at these locations. It should be noted that this problem only occurs in shallow seas, since for very long tethers the stiffness decreases with length, causing lower stresses.

The large stress fluctuations make the tethers sensitive to fatigue damage. A check for fatigue performance is not part of the scope of this thesis, because earthquake loading is a phenomenon with a low amount of loading cycles. Therefore it is normally not accounted for in a fatigue analyses. The flexible tethers will however also effect the hydrodynamic performance, which should be accounted for in fatigue analysis. I.e. wave loading cycles are above the range of 10^6 loading cyles.

6.2.5 Effect of multi-support excitation

Structures with multiple supports can be sensitive to a delay in arrival time of seismic waves to the substructure. Especially long span structures, such as suspension bridges, can be sensitive to multi-support excitation (MSE) effects. The structure is then not excited as a rigid body, but supports are excited out-of-phase, possibly causing significant internal stresses. SFTs meet the characteristics of a structure sensitive to these effects: long-span & supported by cables. The phenomenon of MSE can occur when earthquakes travel horizontally (angle of attack $\alpha = 0$) and hits a SFT or tunnel in line with its longitudinal axis, this is studied in subsection 6.2.5.1. Other angles of attack can occur as well, where the wave approaches the structure sideways ($\alpha = 90^\circ$) or diagonally ($0 < \alpha < 90^\circ$) in the horizontal plane, as studied in subsection 6.2.5.2. Later also an experiment is performed where a vertical traveling earthquake approaches the tunnel-system, in subsection 6.2.5.3. This imitates a situation where the epicenter is below the structure.

For the multi-support excitation analysis, the SFT configuration with best performance in the synchronized analyses is used: the SFT with a GINA/10 end-joint profile, equal to a tenth of a GINA profiles stiffness. It is excited with the normative earthquake spectrum for displacements and tether stresses: Derince (Turkey, 1999) scaled to a PGA of 0.1g. The signal is applied with a delay on the supports of the land tunnel and SFT. This delay is dependent on the location in the SFT x and the shearwave speed $v_{s,30}$ of the top 30 meters of soil and the angle of attack α . The tunnel is located in a clay soil, where according to Eurocode 8 (([NEN-EN 1998-1, 2005](#)), table 3.1, ground type C) shear waves occur with wave speeds between $v_s = 180$ and $360m/s$. For this study, wave speeds between $v_s = 100$ and $1000m/s$ have been studied to explore the effect for other soil types as well. The synchronized support excitation load case can be interpreted as a shear wave velocity approaching infinity ($v_s \rightarrow \infty$), causing all supports to be excited at the same instant.

The delay t_0 (in seconds) is dependent on x , $v_{s,30}$ and α . Its relationship is visualized in Figure 6.36 below:

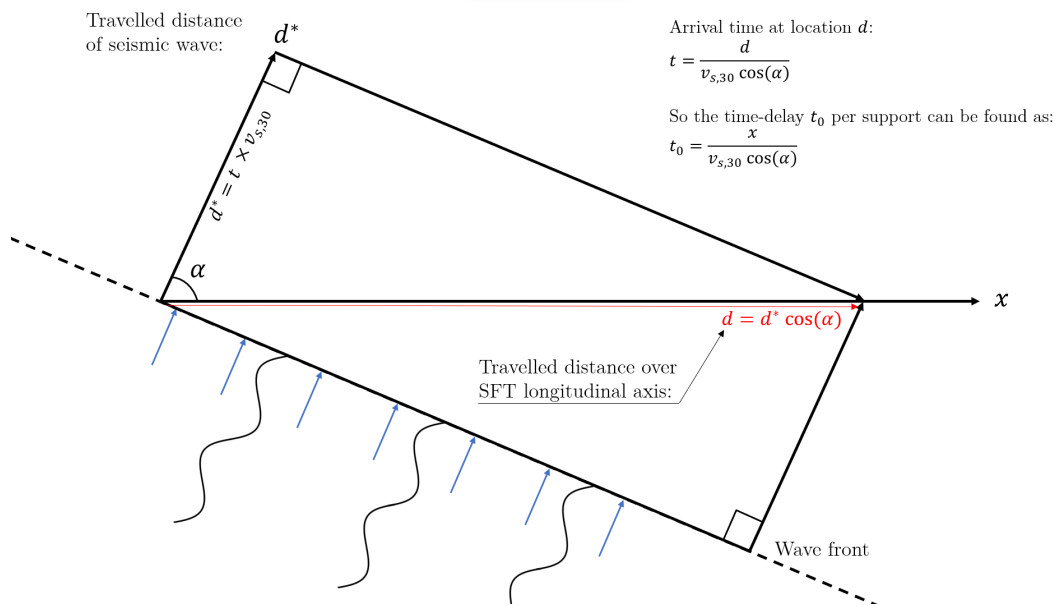


Figure 6.36: Derivation of time delay t_0 due to angle of attack α

The angle of attack rotates the ground accelerations applied on soil springs. Below the longitudinal, horizontal and vertical new ground accelerations are found with the * superscript.

$$\begin{aligned}
 a_{g,x}^*(x, t, \alpha) &= a_{g,x}(x, t) \cos(\alpha) + a_{g,y}(x, t) \sin(\alpha) \\
 a_{g,y}^*(x, t, \alpha) &= a_{g,x}(x, t) \sin(\alpha) + a_{g,y}(x, t) \cos(\alpha) \\
 a_{g,z}^*(x, t, \alpha) &= a_{g,z}(x, t)
 \end{aligned} \tag{6.10}$$

The rotated acceleration signals and time delay's yields the shifted Fourier displacement signal $\tilde{W}_{g,i}$:

$$\begin{aligned}\tilde{W}_{g,i}(x, \omega, \alpha) &= \frac{-\int_{-\infty}^{\infty} a_{g,i}^*(x, t - t_0) e^{-i\omega t} dt}{\omega^2} \\ \tilde{W}_{g,i}(x, \omega, \alpha) &= \frac{-\int_{-\infty}^{\infty} a_{g,i}^*(x, t) e^{-i\omega t} dt}{\omega^2} e^{-i\omega t_0} \\ &\text{with : } i = x, y, z ; t_0 = \frac{x}{v_{s,30} \cos(\alpha)}\end{aligned}\quad (6.11)$$

$\tilde{W}_{g,i}$ is then used as input for the multi-support excitation analysis.

6.2.5.1 Results of in-line MSE with various shear wave velocities

In this subsection, the results of the in-line MSE analysis ($\alpha = 0$) are presented for shear wave velocities in the range $100 \leq v_{s,30} \leq 1000$ m/s. This is done by comparing maximum and minimum values of the characteristic parameters with the results of the synchronized support excitation analysis. Tabulated results of the multi-support excitation analyses can be found in Appendix C.

In Figure 6.37 the normalised maximum and minimum displacements are plotted against shear wave velocities v_s . The parameters are normalized with respect to the results for the same parameter in the synchronous support excitation analysis. It can clearly be seen that the influence of the MSE is limited for the difference in displacements. Maximum displacements are found for $v_s = 100$ m/s with 7.354% increase in longitudinal, 6.92% in vertical and 3.27% increase in horizontal direction. In vertical and longitudinal direction the displacements are greater than the synchronized results for all values of v_s , although the amplifying effect is more present for the low velocities around 100 m/s.

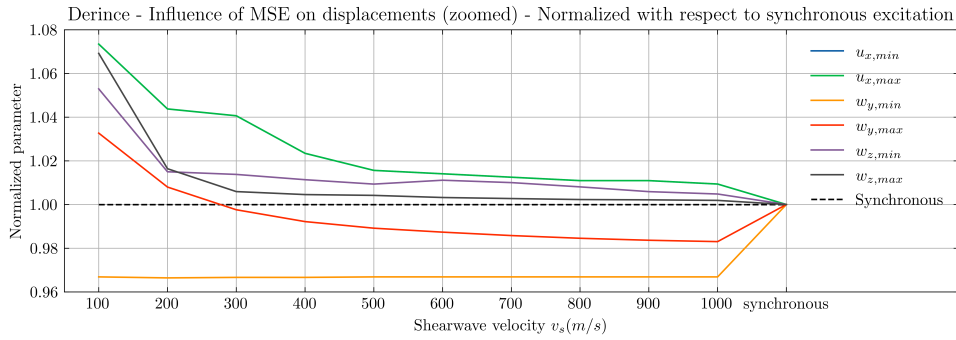


Figure 6.37: Maximum displacements for various shear wave speeds, normalized with respect to synchronized results

In Figure 6.38 the relationship of the internal forces with the applied shear wave velocity is displayed. An increase in normal force of 32.38% compared to the synchronized results are visible for the $v_s = 400$ m/s considered in the analysis. For velocities below 200 and above 500 m/s the normal forces are below the synchronized results.

The bending moments and shear forces (Figure 6.38) in vertical direction shows increments as well, with the largest increments for low values of v_s , with a peak increment of 61.92% for M_{zz} and 38.38% for V_{zz} at the far left of the plot ($v_s = 100$ m/s). The horizontal bending moments and shear forces show peaks of 5.10% for M_{yy} and 28.46% for V_{yy} at $v_s = 300$ m/s, and are below the synchronous result for other shear wave velocities.

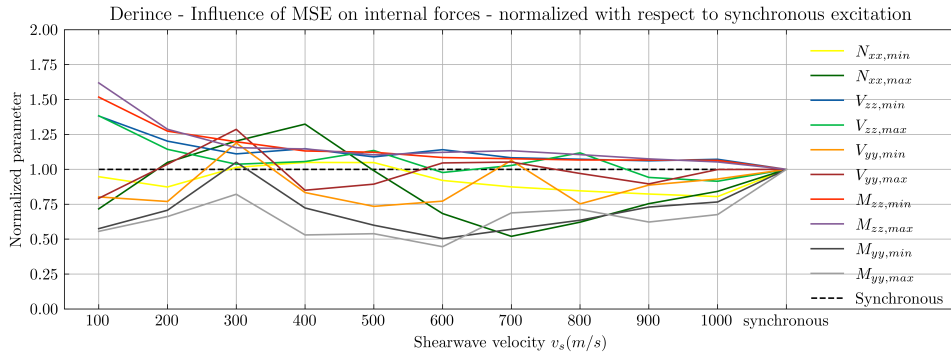


Figure 6.38: Maximum internal forces for various shear wave speeds, normalized with respect to synchronized results

Although the Normal force shows the second largest increase (32.38%) due to the multi-support excitation, its share in additional stresses is limited, compared to the stresses that bending moments cause. For the largest normal force found at $v_s = 400\text{m/s}$ (-9249 kN) an additional stress of 0.178 MPa is found. This is caused by the choice of end-joint, that allows for a large flexibility and displacement capacity at the transition structure. The longitudinal displacements of the land tunnel are therefore not directly transferred to the SFT. This causes a strong reduction of the normal forces and their share in maximum stresses. For the monolithic joint, the normal forces would therefore cause a significant increase of normal stresses, unlike the GINA/10 end-joint.

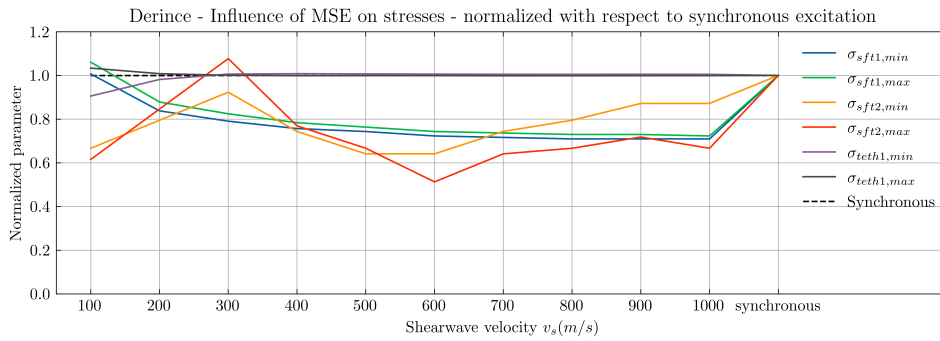


Figure 6.39: Maximum stresses for various shear wave speeds, normalized with respect to synchronized results

The normal stresses in the SFT cross-section (see Figure 6.39) are governed by the bending moment distributions. $\sigma_{sft,1}$ is governed by the vertical bending moments M_{zz} and $\sigma_{sft,2}$ is governed by the horizontal bending moments M_{yy} . Their respective relations with the shear wave velocity have similar patterns as can be seen by comparing Figures 6.38 & 6.39. The normative stress parameter $\sigma_{sft,1}$ is largest when M_{zz} peaks at $v_s = 100\text{m/s}$. It shows an increase in normal stresses of 6.08% at max. The second cross-sectional stress parameter $\sigma_{sft,2}$ is for the MSE analysis mostly lower than in the synchronized analysis, with a max at 7.69% increase at $v_s = 300\text{m/s}$. For other shear wave velocities it shows lower stresses. This pattern can also be seen in the M_{yy} parameter.

The stresses in the tethers (Figure 6.39) are influenced most at low shear wave speeds near 100 m/s. This is presumably caused by the fact that the seabed is then not vibrating in sync with the land-tunnels. When the seabed is kept restraint, while the SFT is being excited, larger stresses will arise in the tethers. The maximum increase in tether stresses at $v_s = 100\text{m/s}$ the increase is greatest at a minor 3.35%. This effect becomes negligible when v_s increases, as at $v_s \geq 300\text{m}$ the tether stresses of the MSE analysis approach the synchronized results. The tether stresses are hardly influenced by the multi-support excitation.

It must be noted that the effects of the MSE analysis can differ strongly per earthquake signal. MSE results for one earthquake signal should not be interpreted as to be applicable on all other signals. To obtain a better understanding, the same experiment should be applied on more signals.

6.2.5.2 Results of in-line MSE with various angles of attack

In the previous subsection the shear wave velocity of 100 m/s, applied in-line ($\alpha = 0^\circ$), turned out to have the greatest impact on the SFT. An earthquakes epicenter can however be located at every imaginable angle with respect to the SFT. Different angles in the horizontal plane as well as in the vertical plane are possible. For this reason, an experiment has been conducted where the angles of attack α , in the horizontal plane, have been varied between 0 and 90° , at the normative velocity of the previous section $v_s = 100\text{m/s}$. This implies that for a 0° angle, the results will be similar to the $v_s = 100\text{m/s}$ results of the previous subsection. For 90° , all support are excited simultaneously, since the incident wave reaches every node of the structure at the same instant, but with a 90° rotated signal.

Displacements in longitudinal and horizontal transverse direction both grow to a maximum in Figure 6.40 when $75 \leq \alpha \leq 90^\circ$. The influence on the vertical displacements is minimal, as the difference is not caused by a rotation, but only by an increase of the velocity of application from 100 m/s to ∞ .

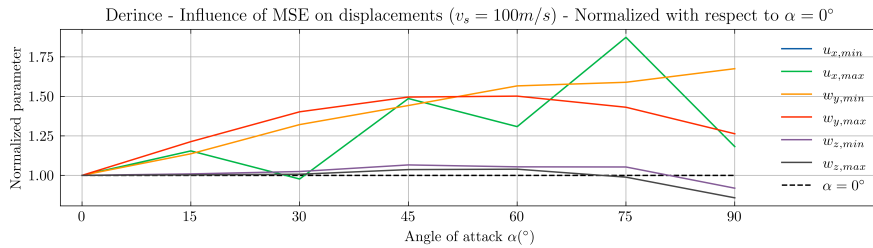


Figure 6.40: Normalized maximum displacements for various angles of attack

The internal forces in Figure 6.41 show the largest increment of results for $60 \leq \alpha \leq 90^\circ$. Horizontal bending moments peak at 60° , whereas normal forces peak at 75° and vertical bending moments at 90° . It can thus be expected that stresses will peak in this range as well.

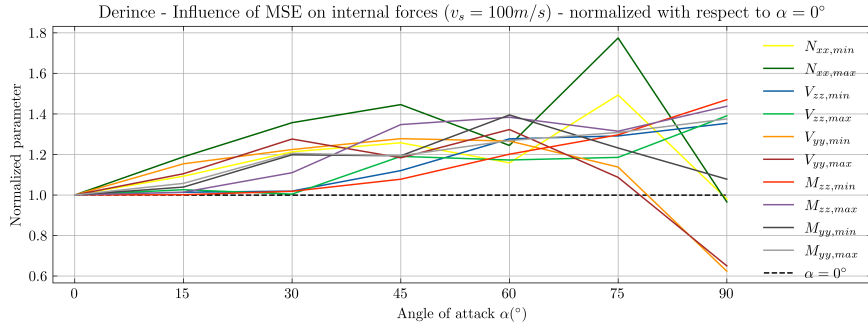


Figure 6.41: Normalized maximum internal forces for various angles of attack

This effect can indeed be observed in Figure 6.42, where $\sigma_{sft,2}$ (horizontal outer fibre) peaks at 60° and $\sigma_{sft,1}$ peaks (vertical outer fibre) at 90° . Earlier in the parameter study it was already found that normal forces are of minor importance for normal stresses compared to bending moments. Hence, a peak due to normal forces can not be observed in the stress diagram in Figure 6.42 below.

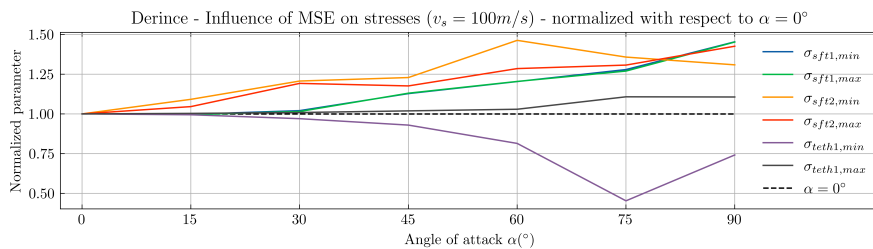


Figure 6.42: Normalized maximum stresses for various angles of attack

6.2.5.3 Results of MSE due to vertical traveling wave

Earthquakes often have an epicenter at depths many kilometres below the surface. In a worst case scenario a seismic event can occur exactly below one's property, causing seismic waves to travel exactly vertically through various layers of rock and soil towards the structure. In this case the composition of the substrate influences the travel time for the wave between initiation at the epicenter and arrival at the structure. For loose cohesionless soils (sand) this can start at 100 m/s and vary up to 1000+ m/s for rock substrates. A variation in soil composition over the length of a long span structure can cause large variations in arrival times.

To simulate this situation an experiment is performed on the GINA/10 end-joint configuration subject to the 0.1g Derince signal with a time delay t_0 varied over the x-coordinate. The high earthquake amplitude at the epicenter is neglected, as a PGA of 0.1g is applied and only the MSE effect is studied. Here it is assumed that for the first traveled kilometres inside the earth, the composition is equal on average, and over top 1000 m of substrate, the composition changes over the SFT length. The outer 30 meters of land tunnel is located in rock ($v_s = 1000$ m/s), the mid 120 meters of land tunnel is located in a clay type of soil ($v_s = 500$ m/s) and the last 100 meters of land tunnel are situated in a loose type of sand ($v_s = 200$ m/s). The SFT is build in softer soil type with $v_s = 100$ m/s. These variations of wave velocities let the arrival times t_0 vary over the length of the SFT as can be seen in Figure 6.43) below:

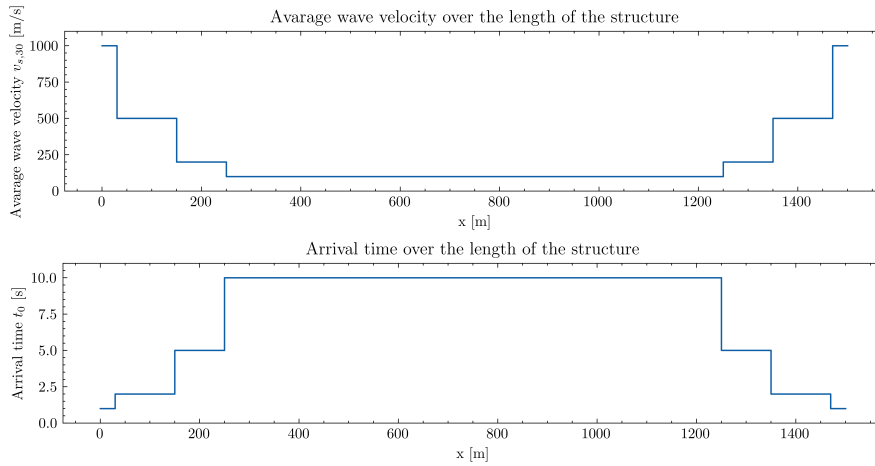


Figure 6.43: Wave velocity and arrival time of seismic wave

The results of the vertical traveling wave are compared to the synchronized support excitation in Figure 6.44 below. The parameters are normalized with the synchronized result above 1.0 means increased results due to the vertical delay, and below 1.0 means the opposite. It can be seen that the influence on displacements is moderate ($-20 - 10\%$) and larger influences are observed for internal forces. Especially the vertical internal forces show large increments ($80 - 100\%$), and the increments in other directions are significant as well ($0 - 30\%$). These same factors are visible in the stress increments in the vertical and horizontal outer fibres ($\sigma_{sft,1}$ & $\sigma_{sft,2}$).

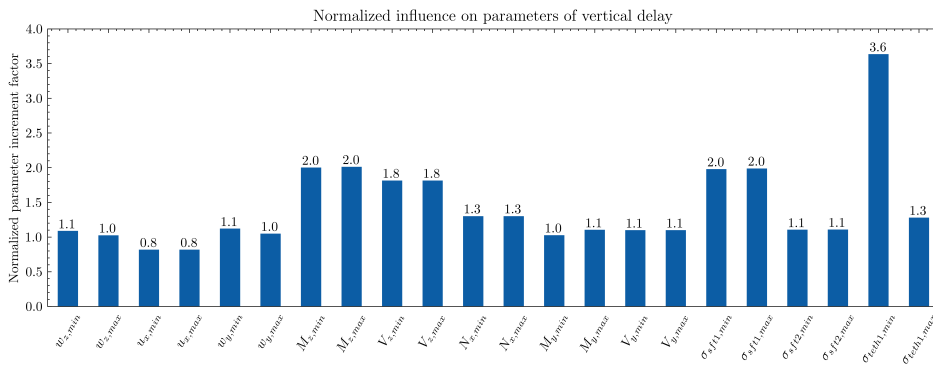


Figure 6.44: Increment of various parameters due to vertical traveling wave compared to synchronous support excitation

The following question arises: what is the cause of the large increments in vertical direction? The frequency content between the spectra is equal, however the phase shift in time of arrival is the varying factor. The vertical direction is the only direction where forcing is applied on the SFT. Forcing is applied through the tethers, whereas no forcing is applied through the mooring lines (horizontal direction) and the longitudinal SFT has no interface with the soil. The time delay results in an application of the seismic load outside-in, combined with a delayed tether load application. This seems to have a magnifying influence on the vertical displacement amplitudes.

It can be concluded that the effect of this vertical traveling Derince earthquake has a great impact (+100%) on internal stresses. The probability that this situation arises will nonetheless be very small, as the epicenter is not likely to occur exactly under the building site. In reality a situation between horizontal and vertical traveling waves is more likely. It is advisable to study both the vertical and horizontal passing waves with various angles of attack in the process of a SFT design, as the results are case dependent.

6.2.6 Alternative closure joints

In this subsection 2 alternative joint configurations are tested and compared to the results of the SFT with GINA/10 end-joint and reduced tether cross-section ($A_{teth} = 1 \times 0.150m^2$) as discussed in subsection 6.2.4.4. Their performance is compared and a trade-off is made to discuss in which loading conditions they are most appropriate. Finally, an increased number of tethers is applied near the transition structure. Its purpose is to experiment with the influence on the stiffness transition between land tunnel and SFT.

6.2.6.1 Base isolation & structural fuse

For SFTs, base isolation can be applied in longitudinal direction to reduce normal forces and longitudinal displacements in the structure. If applied correctly, base isolation lets the structure move in a rigid body mode, instead of it undergoing large internal strains. The GINA profile, as described in subsection 5.3.1, can be interpreted as a kind of base isolation, since it is modelled as a translation spring between the land tunnel and the SFT. If a more flexible type of base isolation is desired to further shift the structures eigen periods, it can be combined with a structural fuse. This fuse keeps the longitudinal end-joint rigidly connected in non-seismic situations. At a certain threshold stress it can break and activate the base isolation system. The system can then move with more longitudinal flexibility.

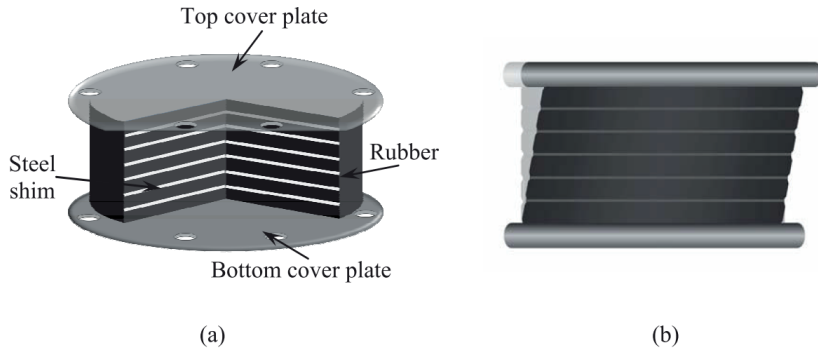


Figure 6.45: Laminated Rubber Bearing (a) & schematized displacement (b)

For a proper examination of the fuse in a SFT a time-history analysis should be performed. The fuse acts as a rigid connection before the threshold normal force is reached and acts completely flexible afterwards. At that moment the base isolation or flexible GINA profile can take over. The model described in this thesis cannot turn off the fuse after the threshold is reached, so instead an experiment is performed with the global model where the fuse is broken before the earthquake hits (assuming a very low threshold force).

In Figure 6.9 it could be seen that although a relatively flexible joint was applied (GINA/10), the longitudinal fundamental frequency of the structure was still overlapping with the first peaks in the longitudinal Derince and Van spectrum. If this fundamental natural frequency could hypothetically be shifted more to the left, normal forces can be reduced even more.

The fundamental natural frequency of the longitudinal system can be determined by evaluating the SFT as a single-mass-spring-system. From Figure 6.9 it can be seen that if the fundamental frequency would be 0.1 Hz, no intersections with Acceleration peaks in the longitudinal Fourier spectra would occur. The fundamental period would then be $T_1 = 10s$, with a total mass of the SFT: $M_{sft} = A_{sft} \rho_c L_{sft} = 159.32 \times 2.5484 \times 1000 = 406014.27 \text{ Ton}$. The relation between the fundamental longitudinal period, the SFT mass M_{sft} and end-joint longitudinal stiffness k_u is presented below:

$$T_1 = 2\pi \sqrt{\frac{M_{sft}}{2k_u}} \quad (6.12)$$

Rewriting equation 6.12 and solving for k_u yields: $k_u = 80144.00 \frac{kN}{m}$. $k_{\theta,z}$ and $k_{theta,y}$ are set to zero, as a hinge is applied in vertical and horizontal direction. Applying these values in the

global model yields the desired shift in natural frequencies displayed in Figure 6.46 below:

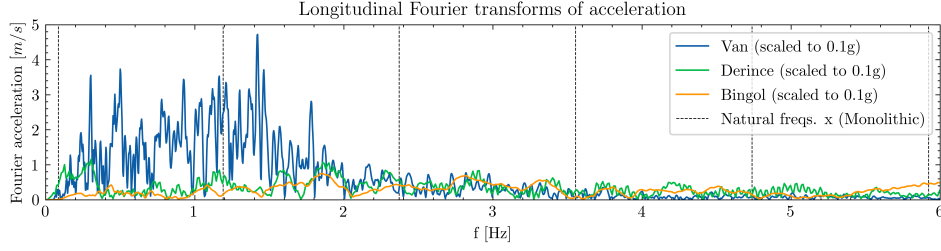


Figure 6.46: Longitudinal natural frequencies with base isolation and Fourier acceleration spectra

The first natural frequency according to the global model is 0.0843 Hz instead of 0.1000 Hz. This shift is presumably caused by the system not actually being a rigid body (as accounted for in equation 6.12), but a semi-flexible rod in longitudinal direction.

The SFT is modelled with a reduced tether cross-section of $A_{teth} = 1 \times 0.150m^2$, the end-joint as a vertical and horizontal hinge, and as a longitudinal spring with spring stiffness $k_u = 80144.00 \frac{kN}{m}$. This yields the following results for the Derince 0.1g synchronized support excitation:

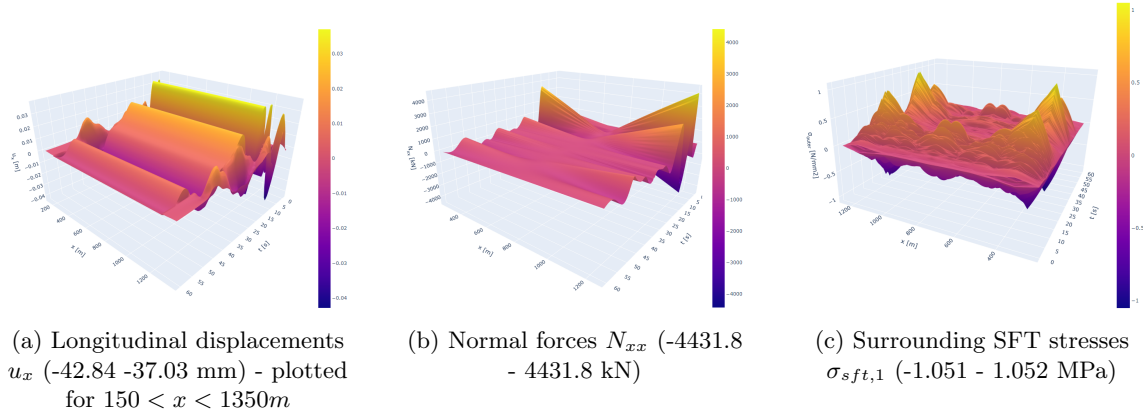


Figure 6.47: Result of base isolated end-joint - Derince (PGA=0.1g)

The maximum normal force in the SFT is $N_{xx} = 4431.8kN$ and the maximum displacement is $u_x = -42.84mm$ (see Figure 6.47). Comparing this to the SFT with GINA/10 end-joint and reduced tether cross-section, the reduction is -79.432% in normal force ($N_{xx} = 976.64kN$ previously) and the longitudinal displacement in the SFT reduced with -33.10% (-64.04 mm previously). While the reduction in normal forces is large, in terms of maximum normal stresses in the SFT cross-section not much changes. The maximum normal stresses are $\sigma_{sft,1} = 1.052MPa$ and have decreased with -28.46% (1.4705 MPa previously). This decrease of stresses is caused by a lower stiffness together with a decrease of longitudinal displacements.

It can be concluded that applying base isolation is a very good manner to reduce normal forces and stresses induced by them. Especially when combined with a vertical and horizontal hinge, such that maximum flexibility is created in all three directions. For stresses due to bending a hinge causes the most reduction, but for stresses due to normal force, a translation spring has the best performance. This flexibility creates lower stiffness (and thus lower stresses), but also reduces the displacements, what reduces stresses even more. The hinge with base isolation and structural fuse configuration can be applied in regions with a PGA of 0.713g, based on the Derince spectrum.

6.2.6.2 Viscous damper

The viscous damper as described in subsection 5.3.2 is applied at the transition structure to create longitudinal damping and rotational damping at the end-joint. For optimal exploitation of the damper capacity it must be used in combination with an end-joint with longitudinal and rotational flexibility. The GINA/10 end-joint with reduced tether ($A_{teth} = 1 \times 0.150m^2$) will be used as a reference ("no damping", in table 6.1). Damping coefficients $c_x = 32,000 \frac{kNs}{m}$ (longitudinal) and $c_{\theta z} = 2.592 \cdot 10^6 \frac{kNms}{rad}$ (vertical rotational) are applied for the analysis "with damping".

Damping is a velocity dependent force, thus if velocities in a signal are rather low (as for Derince), damping action will be less. The analysis is therefore performed with the Van 0.1g spectrum, since this signal has more high frequency (and high velocity) vibrations compared to the Derince signal. See Figure 6.48 for a visualisation of the displacement, normal force and surrounding normal stress patterns for the "With damping" analysis. The results of the analysis with and without damping, as well as the damping parameters x3 and /2 are displayed in Table 6.1 below.

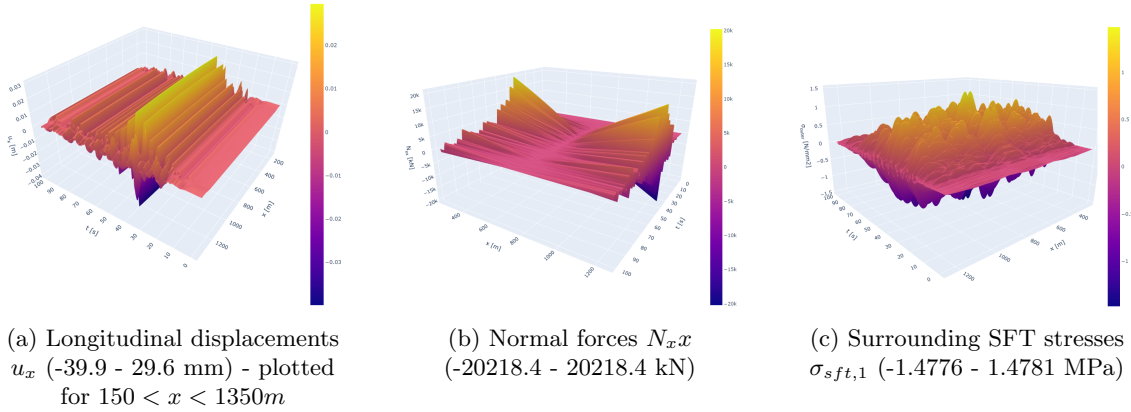


Figure 6.48: Result of GINA/10 end-joint with viscous damper - Van (PGA=0.1g)

Results end-joint with viscous damping - Van (scaled to PGA=0.1g)					
Param.	No damping	With damping	Damping x3	Damping /2	Unit
c_x	0	$3.20 \cdot 10^4$	$9.60 \cdot 10^4$	$1.60 \cdot 10^4$	$\frac{kNs}{m}$
$c_{\theta z}$	0	$2.60 \cdot 10^6$	$7.79 \cdot 10^6$	$1.30 \cdot 10^6$	$\frac{kNms}{rad}$
$u_{x,max}$	45.129	29.562	29.776	33.048	mm
$u_{x,min}$	-45.129	-39.863	-41.696	-42.257	mm
$w_{y,max}$	41.86	41.86	41.86	41.86	mm
$w_{z,max}$	56.08	41.07	41.12	41.05	mm
$N_{xx,max}$	23092.6	20218.4	19011.5	21515.3	kN
$M_{yy,max}$	3233.9	3233.9	3233.9	3233.9	MNm
$M_{zz,max}$	761.9	314.9	311.1	315.9	MNm
$\sigma_{sft,1,max}$	3.761	1.478	1.466	1.482	Mpa

Table 6.1: Results end-joint with viscous damping - Van (scaled to PGA=0.1g)

Table 6.1 shows that the longitudinal displacements reduce a bit (-6.36 up to -11.67%), due to the viscous dampers, and vertical deflections reduce even more (-26.8%). The normal forces decrease with -6.83 up to -17.673% dependent on the configuration.

The viscous dampers drastically reduce vertical bending moments $M_{zz,max}$ and displacements $w_{z,max}$. A reduction of -58.67% is found for $M_{zz,max}$ and -26.76% for $w_{z,max}$. The result is that the stresses are decreased with 60.70% due to the decrease of normal forces and bending moments. Here, the bending moments cause the largest drop in normal stresses. It is remarkable that the amount of damping hardly influences the bending moments and deflections, so a lower amount of damping suffices.

It can be concluded that viscous dampers can have big impact on the normal forces and bending moments found in a SFT. The stress reduction compared to the normal GINA/10 joint is -60.7% at maximum, and this surpasses the reduction of stresses found with seismic base isolation (-28.4%). It seems that even though the system is already considerably damped by the surrounding water, viscous damping (at the end joint) can still cause a performance increase. One can imagine that the combination of a damper with base isolated joint would result in even better performance. The GINA/10 + damping x3 configuration can be applied in a region with a PGA of 0.519g, based on the Van spectrum.

6.2.6.3 Increased number of tethers near end-joint

Monolithic end-joints are an ideal solution considering the manufacturability of the end-joint. Previous analyses showed that the rigid connection is inferior to more flexible ones, as their displacements and internal forces are both considerably larger. The problem with the monolithic end-joint might be the sudden transition from a "stiff bedding" at the land tunnel to "no bedding" at the SFT. This causes peaks in bending moments, especially at the end-joint end tether supports. These support moments have the potential to be decreased by gradually decreasing the bedding stiffness to zero over a certain length.

This can in theory be done on the land tunnel side or on the SFT side, but in practise it is labor intensive and uneconomical to apply ground improvement around the land tunnel. A better solution would be to apply a number of larger tethers over the first 100 m of SFT to gradually decrease the bedding stiffness to zero. Potentially the same can be done in horizontal direction by increasing the number of mooring lines near the end-joint. To accomplish a gradient in the support stiffness, the tether center-to-center distance or cross-sectional area can be varied.

This concept is applied in vertical direction on the configuration with monolithic end-joint subjected to the 0.1g Van spectrum. Tethers are applied with an interval of 10m over the first 100 m of SFT after the transition structure. The tether stiffness starts at the end-joint with $k_{teth} = 5 \cdot 10^6 kN/m$ and decreases linearly to zero over a length of 100 m. Forcing is applied here as well in the form of a prescribed displacement at the tether seabed connection.

Results obtained by this analysis show a decrease of vertical displacements by -3.78% in Figure 6.49. This effect is of minor importance, and thus it can be concluded that the measure hardly influences the displacements in the middle region of the SFT.

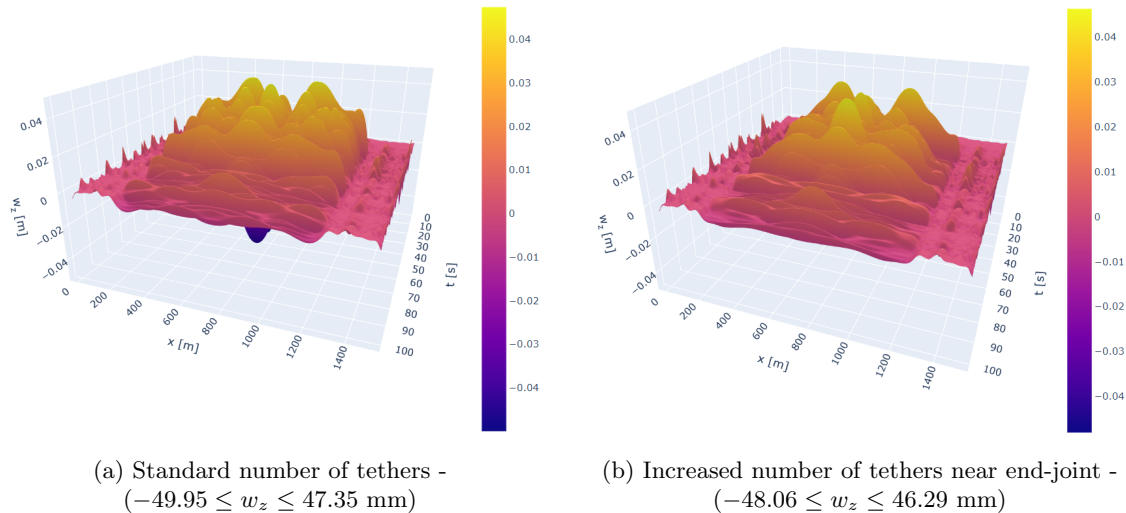
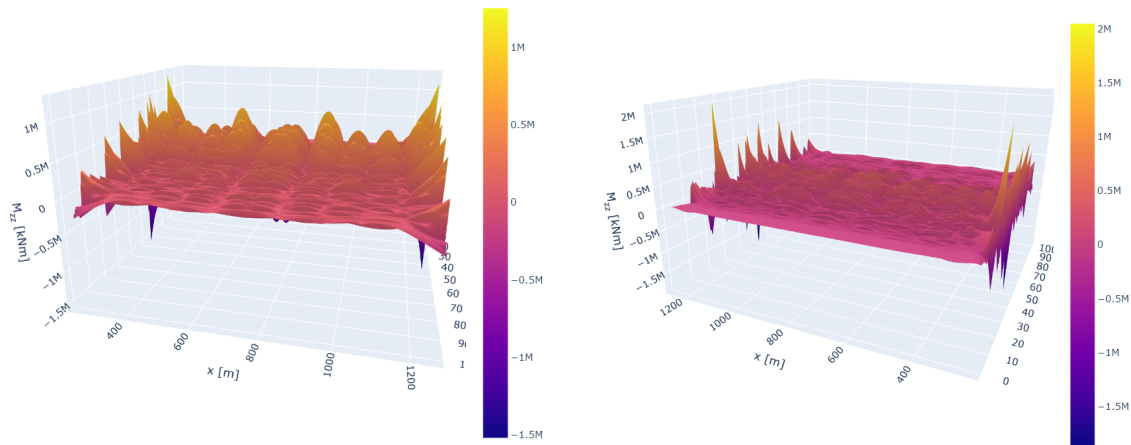


Figure 6.49: Vertical displacement w_z - Monolithic end-joint - Van 0.1g

Bending moments on the other side, show a reduction between $300 \leq x \leq 1200$ of -41.83% and an increase of the support bending moments with 63.6% in Figure 6.50. The increased stiffness causes larger bending moments at the end-joint, but lower over the remaining part of the SFT. This means that the a large saving of high strength steel and building costs can be obtained over the largest SFT span, and the only at the end-joint more prestress is needed. The stiffness of the

tethers is not varied here, so in case the tether stiffness is better tuned to the frequency dependent soil stiffness, a better performance can be reached.



(a) Standard number of tethers - $(-1520.6 \leq M_{zz} \leq 1252.8 \text{ MNm})$ (b) Increased number of tethers near end-joint - $(-1861.1 \leq M_{zz} \leq 2049.6 \text{ MNm})$

Figure 6.50

A change of the number of tethers will obviously influence the natural frequencies. In Figure 6.51 its influence is studied for the first 11 natural frequencies and compared for to the standard monolithic end-joint, and is plotted over the vertical Van spectrum. A shift is visible for natural frequency number 4 and higher. Presumably, the difference is higher for modes that have large relative displacements over the first 100 m of SFT, causing the increased tether stiffness to positively influence the respective natural frequency.

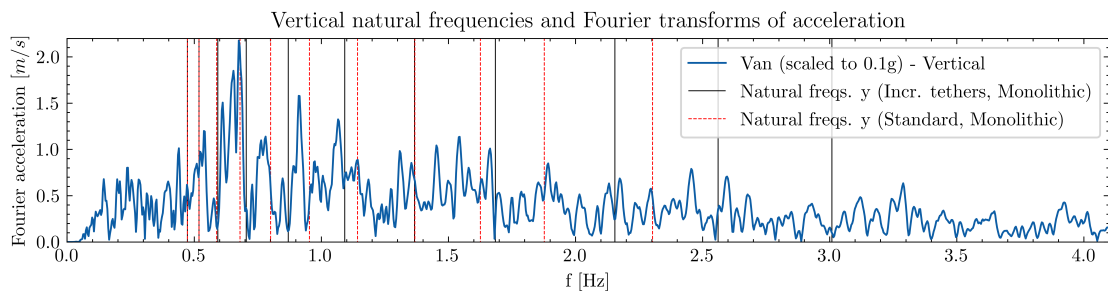


Figure 6.51: Vertical natural frequencies for standard and increased number of tethers

By creating a gradient transition between the stiff bedding and the SFT, one can thus decrease bending stresses in the SFT. In horizontal direction a similar principle can be applied by increasing the number of mooring lines. The two transverse directions cause the vast majority of the normal stresses in the SFT, therefore it is likely that the monolithic end-joint becomes more attractive with this method.

In the longitudinal direction, the method could be applied with prestressed diagonal tethers in the x-z plane. Further research needs to show to what degree this increases the support stiffness in x-direction and its influence on normal stresses.

6.2.7 Evaluation of the Effect of SSI

In all analyses mentioned previously in this chapter, the effect of Soil-Structure Interaction has been incorporated. This is done by means of the frequency-dependent bedding springs, applied at the land tunnel. However, in most previous studies on submerged floating tunnels, the land tunnel is not taken into account and the earthquake loading is applied directly in the form of accelerations at the SFT end-joint boundary. The following question arises: to what degree did the SSI alter the results of this study?

In this subsection, the bedding stiffness of the soil is increased to create an "infinitely rigid" land tunnel, to imitate the situation of "no SSI". A distributed spring stiffness is assumed of $\bar{k}_{soil,ii} = 10^{14} kN/m/m$ with $i = x, y, z$ (equal in all directions, independent of ω). For this value, the land tunnel displacement approaches the ground displacements and the land tunnel rotation at the transition structure approaches zero.

To demonstrate the effect, the monolithic end-joint configuration is subjected to the 0.1g Van spectrum. The influence on the natural frequencies is compared with and without SSI in Figure 6.52 below. It can be seen that the horizontal natural frequencies decrease when SSI is turned on. This is to be expected since the stiffness of the structure and the natural frequencies are proportional to each other. A lower bedding stiffness therefore causes lower natural frequencies. The influence on the first natural frequency is limited, but the difference increases for higher natural frequencies. Figure 6.52 shows that the shift lets the different modes be excited with higher peaks in the horizontal Fourier spectrum, causing larger displacements in horizontal direction.

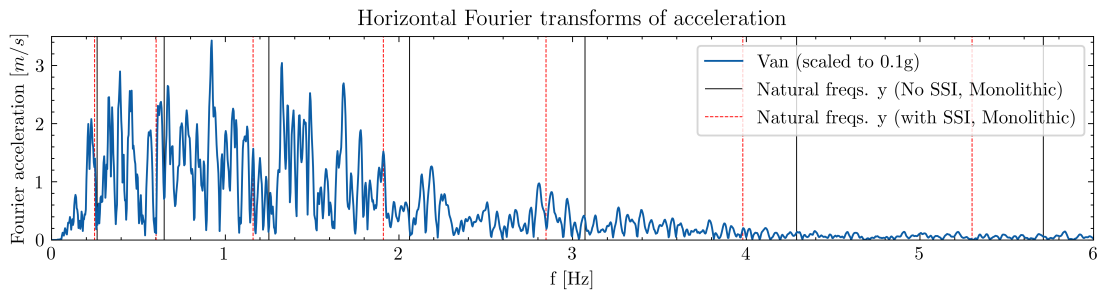


Figure 6.52: Influence SSI on horizontal natural frequencies with Van Fourier transform - Monolithic end-joint

This increment in horizontal displacements can indeed be seen in Figure 6.53, where the influence of SSI on various parameters is expressed in terms of a normalized influence factor. The capricious earthquake Fourier spectrum however makes the effect of SSI rather unpredictable. Small changes in stiffness or mass parameters can shift the natural frequencies and every earthquake spectrum is different. Hence, SSI has a large influence on the response, but if its effect is positive or negative depends on the structure, the soil and the chosen earthquake signal.

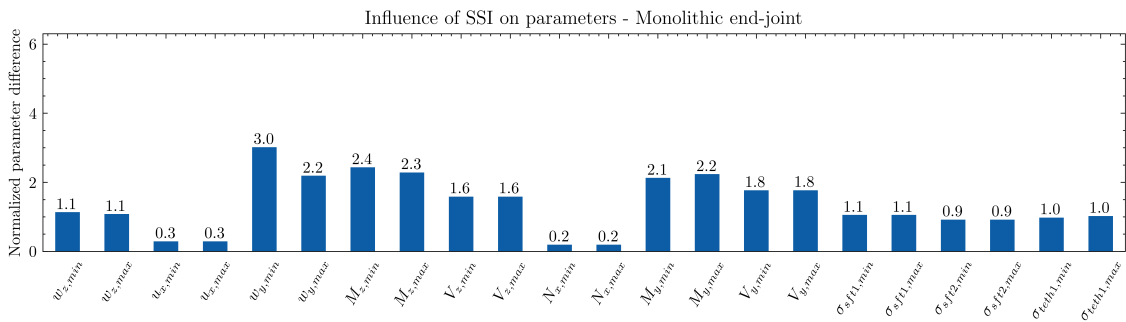


Figure 6.53: Normalized influence of SSI on parameters - Monolithic end-joint

In Figure 6.53 the longitudinal displacements and normal forces can be seen to be reduced by the SSI effect. The displacement that is applied on the land tunnel at $x = 0$ and $x = 1500m$ is not directly transferred to the SFT, but is highly damped and restrained by the bedding springs. This

causes considerably lower displacements at the end-joints than when the earthquake acceleration would be directly applied here.

On the other side, it is imaginable that ground displacements are not transferred 1:1 from the soil to the structure. This added flexibility might give a better representation of the actual displacements and forces at the transition structure. Moreover, soil has only a limited shear stress capacity, after which a plastic limit is reached and shear stresses no longer increase at larger displacements. The chosen linear-elastic model therefore overestimates the maximum soil shear stresses and thus normal forces transferred from the soil to the land tunnel. With this in mind, one can say that the model with SSI is more likely to overestimate the normal forces in the structure, and that safety and overcapacity in longitudinal direction is build in to the model of this thesis. The reduced longitudinal displacements and normal forces are therefore in line with the expectations.

6.2.8 Evaluation of the effect of soil coupling

The SSI in the global model does not account for coupling between directions x-y, x-z and y-z, while for instance a vertical force on the land tunnel will result in a small longitudinal displacement. In this subsection its influence on the results is discussed.

To build the Comsol model, a modeling assumption has been made to model the land tunnel tube as a hollow cylinder. This allowed for local displacements and made the displacements at the centroidal axis unknown. For the Substructuring method, the displacements are measured in the lower outer fibre of one of the land tunnel tubes, whereas it later turned out that these can better be searched for at the centroidal axis of the tunnel. This is where the line-model discussed in this thesis is virtually located. Out-of-plane deformations were later found to be unevenly distributed over the cross-section, due to rotations around the y- and z-axis and local deformations in the cross-section (circular section deforms into an oval shape). Due to a shortage in time, it is chosen to not adapt the Comsol model but visually check the out-of-plane deformations due to a vertical harmonic load.

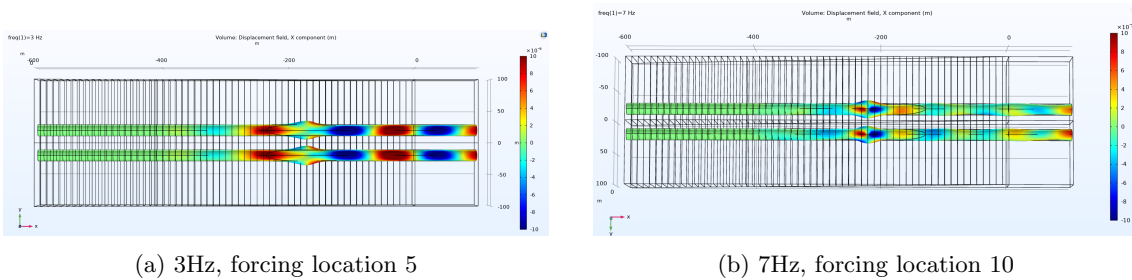


Figure 6.54: Comsol results: longitudinal displacement u_x due to vertical harmonic load

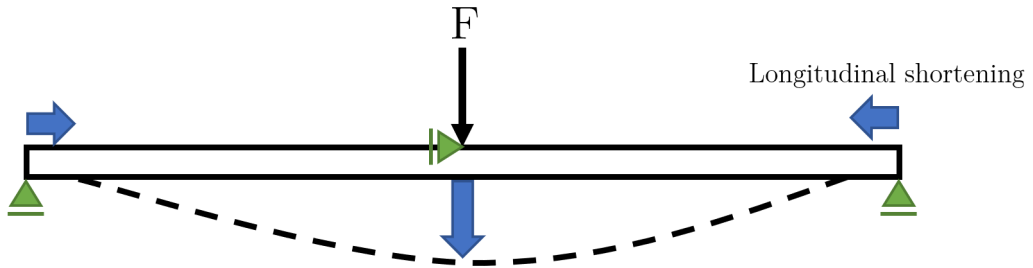


Figure 6.55: Longitudinal shortening (simplified)

The results of vertical harmonic loads at various locations and forcing frequencies show similar patterns in terms of displacement modes. The longitudinal displacement (Figure 6.57) of the neighboring elements are moving towards the load location, under the effect of longitudinal shortening due to an out-of-plane load. This is a different effect than the SSI coupling that was aimed to capture. It seems that the coupling effect is only of a very local nature (within one wavelength). Longitudinal shortening is an effect that is seen in every beam with out-of-plane loading. This

effect is neglected in the global model, since the chosen element type is of the non-linear Euler-Bernoulli type, which does not account for axial deformations. All in all, it seems justified to neglect the longitudinal coupling in the soil model, as is done in the global model.

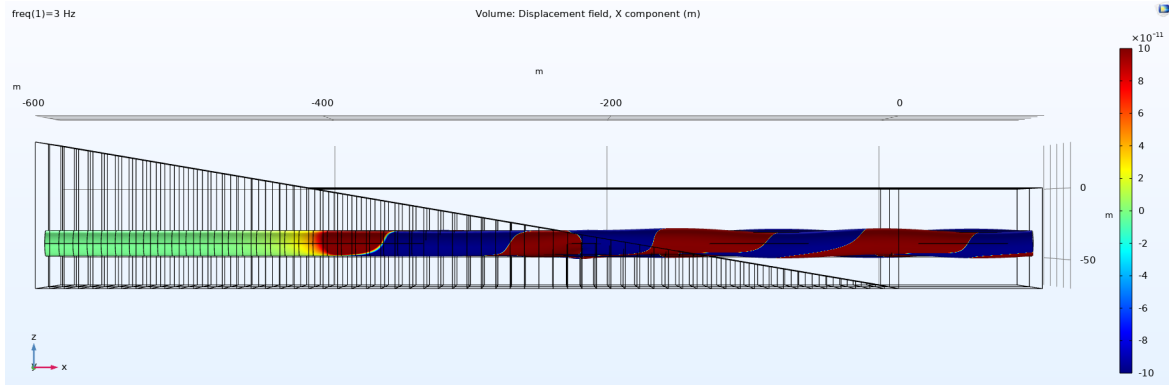
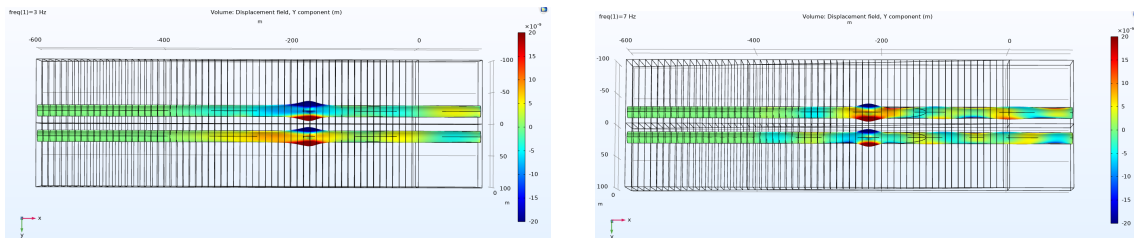


Figure 6.56: Comsol results: longitudinal displacement u_x due to Horizontal harmonic load at location 10

For the coupling between x-y a similar effect can be seen in Figure 6.56, where the longitudinal deflection is plotted due to a horizontal harmonic load of 3Hz at location 10. The coupling displacement that can be seen is of the "longitudinal shortening" type, and no additional rotations of the land tunnel are observed.



(a) 3Hz, forcing location 5

(b) 7Hz, forcing location 10

Figure 6.57: Comsol results: horizontal displacement w_y due to vertical harmonic load

The horizontal displacements due to a vertical harmonic load (Figure 6.57) show symmetrical deformation patterns along the x-axis. These deformations are of the local type and cause the cylinder to deform into an ellipse shape. The inner walls move inward and outer walls outward equally on either sides of the centroidal axis. It can be reasoned that interpolation of these outer fiber displacements to the centroidal axis would result in zero displacements in the horizontal direction and no coupling between y and z.

For future research purposes where a similar model **with coupling** is desirable, it is noted that it is a better option to choose a solid cylinder shape with an equivalent bending and axial stiffness. It will have a lower vulnerability for local deformations, so the obtained out-of-plane deformations are not distorted and only show the global deformations. Ideally, it will have nodes on the centroidal axis, so the displacements can be found there to calculate the flexibility and bedding stiffness matrices. However, for the situation studied in this thesis, it can be said that the influence of soil coupling on the land tunnel is small.

Chapter 7

Discussion

This chapter presents a discussion of the modeling assumptions and results of the parameter study. The modeling assumptions are discussed in section 7.1, where the results of the parameter study (Chapter 6) are checked to be in-line with the assumptions mentioned in the methods (Chapter 3). Moreover, the results from the parameter study (Chapter 6) are discussed in section 7.2, to see what lessons can be drawn from them.

7.1 Discussion on assumptions

In this section the impact of modelling assumptions on the results from Chapter 6 is discussed.

7.1.1 Geometrical Non-linearity's

Geometrical non-linearity's have been neglected in this thesis, because small displacements are expected. The largest displacements are found in the horizontal direction. For the monolithic configuration (with PGA of 0.1g) , displacements are found around 40cm in the $SLS_{seismic}$ load case. For the infinitesimal strain theory* to be applicable, the horizontal displacements δ_h should meet the following inequality:

$$\delta_h \leq \frac{\Delta L_{moor}}{100} = \frac{200}{100} = 2m \quad (7.1)$$

Hence, horizontal displacement should be less then 2 meters, implying a maximum PGA of 0.5g. Other end-joints with more rotational flexibility (hinge, GINA, etc.) have smaller horizontal displacements proportional to 4cm at a PGA of 0.1g. This makes these analyses applicable up to a PGA of 5.0g. The assumption of no geometrical non-linearity is thus justified for most seismic areas.

The geometrical non-linear behaviour of the mooring lines is linearized as well using the method described by (Peters, 1993). Its stiffness seemed to have a small influence on the horizontal behavior, but should be taken into account using non-linear springs for a more detailed design study.

*theory of small displacements used for the Euler-Bernoulli beam theory

7.1.2 Material Non-linearities

Material non-linearity's are neglected as well, since the displacements and stresses are checked in SLS. In this limit state no plasticity is allowed, and the stress-strain relations in the structure are linear. At every analysis, checks are made if the observed stresses remain below the stress limit and the maximum PGA is mentioned at which this requirement is met (see subsection 6.2.4.3 on effects on SFT stresses). Hence, the assumption of no material non-linearity's is justified.

7.1.3 Land tunnel element size

The element size of the land tunnel is chosen such that the land-tunnel correctly represents the physics of the structure, as described in subsection 3.1.2. The rule-of-thumb says that the meshsize of a finite element model should be no less then $\frac{1}{8}$ of the minimum wavelength in a structure. This

assumption implies that using this mesh, the mass and stiffness of the structure should be correctly modelled and the displacements in the land-tunnel should give good correspondence with the results of a finer mesh.

For a correct representation of internal forces however, a finer mesh should be chosen. Every land tunnel node is connected to a bedding spring with unique stiffness. The variation of stiffness from node to node induces singularities in the internal forces, causing an overestimation in their values. For the sake of readability of figures, the land tunnel forces have not been presented in this thesis, as their scale is in a different order of magnitude than the SFT internal forces.

7.1.4 Coupling

The 3 separate directions of this thesis are treated as if they are uncoupled. In reality there is some degree of coupling through the soil and the mooring lines. In subsection 6.2.8 it is shown that soil coupling between y and z creates local deformations, but these approach zero at the centroidal axis. Soil coupling in x-z and x-y causes a geometrical non-linear effect, where axial shortening due to out-of-plane loading is seen. As this effect is neglected in the global model it is found appropriate to neglect this in the soil submodel as well.

Mooring lines couple the SFT transverse displacements (y and z) with the torsional DOF (rotation around x). Mooring lines are several orders of magnitudes more flexible than tethers and rotation around x is not incorporated in the model DOFs. Hence, coupling through the mooring lines could not be incorporated in this thesis, but for a more detailed study it is advised to take this extra DOF with mooring coupling into account.

7.1.5 Rayleigh Damping

Rayleigh damping is applied to account for structural damping of 5% as is advised for concrete. It is tuned to the 1th and 10th vertical natural frequency. The chosen amount of Rayleigh damping has a large influence on the results. To be on the safe side, a relatively low amount of Rayleigh damping ($\alpha_R = 0.241$ & $\beta_R = 0.006$) is used, based on the chosen frequency range that should be damped. It is combined with the Morison damping, which effect dominates the damping behaviour. Therefore, the material damping can be slightly underestimated. The Rayleigh damping cannot be set to zero for a frequency domain method, because for the Fourier transform to work properly, the response should start and end at a zero-valued amplitude. This can only be achieved by means of enough damping over the whole structure.

7.1.6 Morison Damping

The linearization of the Morison damping force is another important assumption. The linearized force should have good correspondence with the largest Morison force in the original (non-linear) equation. In other words, if the (linear) frequency domain model described in this thesis would be compared with an identical time-integration model with non-linear Morison force, the region of the peak forces should show good agreement. Elsewhere in the time-history, the internal forces will show significant differences and the Morison force will be overestimated. This model is thus qualified to predict the maximum internal forces and displacements, but will not reproduce the exact time-history results. Due to a shortage in time the Morison damping model could not be validated, as the DIANA model of Chapter 4 (Validation of the model) could not account for the velocity dependent damping force.

Application of Morison damping implies several secondary assumptions:

1. The flow acceleration should be more-or-less uniform at the location of the body. This assumption is met, since the flow of water is left outside the scope of this theses. The water therefore has a zero velocity.
2. The inertia and drag force contributions in the Morison equation are valid for very small and very large Keulegan–Carpenter numbers respectively. The Keulegan–Carpenter numbers in

this study approach zero (as can be seen in Equation 7.2). This indicates that the drag and inertia contributions can be added to describe the force fluctuations

$$K_C = \frac{VT}{D} = \frac{< 1 \text{ m/s} \times < 1 \text{ s}}{18 \text{ m}} \sim < 0.0556 \quad (7.2)$$

7.2 Discussion on results

In this section several findings from the parameter study are repeated and discussed.

7.2.0.1 Tether stiffness

In subsection 6.2.4.4, it became apparent that stress fluctuations in tethers become very high, which increases the likelihood of tether slack. This effect can especially be seen near the shore (shorter tether length) and is amplified when A_{teth} is increased.

In the parameter study of Chapter 6 this is solved by lowering A_{teth} and increasing the amount of tether prestress, together with a higher steel quality. Alternatively inclined tethers can be used, which reduces the tether stiffness without a reduction of the tether cross-section. This solutions seems more economic then high strength steel, but can not be examined using the vertical tether sub-model used in this thesis.

7.2.0.2 Diversity in Earthquake spectra

The earthquake spectra used for the parameter study are not scaled to the same response spectrum, but only to an equal PGA of 0.1g. Hence, the frequencies are different for each spectrum, causing a large variety in results in Chapter 6. This is chosen to show how the SFT structure responds to different dominant frequencies and bandwidths.

In the results of Chapter 6 it was visible that the low frequency earthquakes "Van" and "Derince" both created more severe responses, whereas the SFT was less sensitive to the high frequency earthquake "Bingol". This is caused by the fact that the dominant frequencies of the low frequency earthquakes are closer to the fundamental natural frequencies of the SFT.

7.2.0.3 Multi-Support-Excitation

The results of subsection 6.2.5 show that applying an earthquake with a horizontal or vertical delay can cause large increments of displacements and forces in SFTs and should be taken into account explicitly or by means of a safety factor. However, the increment factor is very much dependent on the configuration of the tunnel (geometry and material parameters) and cannot be generalized to other configurations. The critical shear wave velocity is dependent on the natural frequencies of the vertical and horizontal beam and longitudinal rod. The combinations of the behavior of the 3 elements yields the critical velocity.

For the horizontal forcing, the largest stresses were found when the spectrum was rotated with 70 – 90°, such that the y-direction was forced with the primary acceleration spectrum and the x-direction with the secondary acceleration spectrum. The Soil-Structure-Interaction lowered the normal forces in the SFT, compared to the "Non-SSI" case. This implies that with SSI the longitudinal x-direction becomes less critical then the transverse y-direction, and the horizontal spectrum with largest amplitude should be placed in transverse horizontal direction.

Chapter 8

Conclusion & recommendations

This chapter describes the conclusions and recommendations that emerge from this master thesis. The recommendations are split up in design recommendations for SFTs and recommendations with respect to future research and knowledge gaps that remain after this study.

8.1 Conclusion

The conclusion covers the main findings of this research and provides an answer to the following subquestions:

1) What types of transition structures can be used and how can these be modelled?

5 types of standard end-joints are covered in Chapter 2: Monolithic, GINAx10, GINA, GINA/10 and Hinged joints. Moreover, 2 special end-joints are described: the seismic base isolation with structural fuse and a flexible joint with viscous damping. Their behavior can be modelled using spring-dashpot interface elements between the rotational and longitudinal translation DOF's of the end-joint. Their performance is tested in the parameter study of Chapter 6. Optionally, a pile foundation and extra mass can be included by adding vertical springs and extra local mass.

2) What method is most appropriate for the assessment of the dynamic SFT+land tunnel model, including the effects of soil, water, and earthquake loading?

The main objective of this thesis was to develop a model that correctly describes the behavior of the SFT and land tunnel. To do so, the interaction of the SFT with water and the land tunnel with soil should be considered with equal rigor. It was chosen to employ this in a 1D finite element model, written in the programming language Python, such that local damping and stiffness additions could be implemented in a straightforward manner. The dynamic stiffness of the soil is derived in a submodel in Comsol Multiphysics and the dynamic tether stiffness is derived using a rod submodel in Python. The (global) system of equations is solved in the frequency domain, as this gave insight in the influence of design choices on the natural frequencies and structural response. For frequency domain models, the soil and tether behavior can be described by dynamic springs, instead of explicitly including the elements in the model. This reduced the number of DOFs drastically with more than 99% and increased the computational efficiency. An additional benefit of the FEM frequency domain analysis, is that it is relatively fast compared to an equivalent time-history FEM analysis.

The global model has been validated with a DIANA FEA time-history analysis in Chapter 4. Here, the SFT is modelled with a single tether and land tunnels are supported on a Winkler foundation. Rayleigh damping is included, but Morison damping could not be properly be applied in the software. Natural frequencies, displacements and internal forces are compared in all 3 directions and showed good correspondence between both methods.

3) The model is validated and the SFT's behavior can be realistically analyzed. The focus of this research regards the global seismic behavior, and more specifically the response of the end-joints. The following conclusions are drawn:

- In general (i.e. bridge and building design), to a certain level of earthquake loading the $SLS_{seismic}$ loadcase will not govern the design (i.e. no design adaptations required for low

level earthquakes). However, for SFT structures this is not applicable. From the presented SFT analyses, it followed that the stresses due to static load + low seismic loads ($SLS_{seismic}$) are already exceeding static $ULS_{fundamental}$ stresses. In this seismic load-case, damage is allowed to secondary components and all other parts of the SFT should remain undamaged and functional. Therefore, earthquake analyses should always be performed for SFT structures and will almost always lead to design adaptations (e.g. increased longitudinal post-tensioning to compensate for tensile stresses).

- From a static and hydrodynamic point of view large tether cross-sections might be desirable to limit the SFT's displacements. Although, for dynamics of SFT structures subject to seismic loading it can be detrimental. More vertical stiffness in the form of tethers attracts higher tether normal forces. Therefore it is advisable to decrease the tether stiffness in one of the two following manners: decrease the cross-sectional area of the vertical tethers or apply the tethers diagonally to decrease the stiffness. In both cases, tension in the tethers will increase and stiffness will decrease, which also decreases the risk of tether slack.

The following statements for maximum PGA's are case specific, regarding the geometry and soil conditions. The results below originate from the low-frequency earthquakes (Van & Derince), which are most critical for SFT structures. SFT structures are less vulnerable to high-frequency earthquakes (e.g. Bingol), allowing for higher PGA's then mentioned below. The judgment is based on the maximum transverse displacements and normal stresses in the SFT and tether stresses. End-joint opening has not been considered (large openings can be designed for with special gaskets). SFT normal stresses are normative in all cases.

- From a durability and maintenance point of view a monolithic SFT is preferred, as these end-joints are less prone to leakages. However, for areas where seismicity with PGA's above 0.05g is expected, Monolithic end-joint's are not advisable. For $PGA > 0.05g$, the concrete stresses in the SFT elements near the shore will exceed the maximum level of concrete prestress.
- Adjustment of the tether configuration can allow the monolithic end-joint to be used in area's with some seismicity. The transition between the stiff bedding and the flexible SFT should then be smoothened. This can be obtained by increasing the number of tethers near the end-joint and gradually decreasing the number or cross-sectional area. The measure decreased the vertical bending moments over the majority of the SFT with 64%. A similar principle can be applied in horizontal direction by applying more mooring lines near the shore.
- Flexible end-joints, such as a hinge or GINA/10, perform well in areas with seismicity up to a PGA of 0.2g. This reduces stresses at the transition structure, but it also causes stress reductions along the remaining alignment. Displacements are reduced as well. This is caused by two phenomena. Firstly, natural frequencies are slightly lowered for the flexible end-joints, compared to the monolithic end-joint. Secondly, the transfer functions show a lower response at the dominant earthquake frequencies, compared to the monolithic end-joint. This indicates that the flexible joints transfer less seismic energy to the structure than a monolithic joint.
- Further reductions of the seismic response can be obtained using seismic base isolation. This can be applied to further increase the longitudinal end-joint flexibility and applicability in areas with seismicity expected up to a PGA of 0.7g (only based on Derince spectrum). It should be combined with a structural fuse to limit end-joint opening in SLS. It causes a decrease of the natural frequencies and shifts the fundamental frequency below the dominant earthquake frequencies. This lowers the normal forces with -93% compared to the monolithic end-joint. This is the preferred mitigation measure when large normal force-induced stresses are expected.
- Viscous dampers can be applied to dampen the longitudinal displacement, as well as the vertical rotation at the end-joint. It allowed for seismicity with a maximum PGA of 0.5g (only based on Van spectrum). This measure caused a -93% decrease in normal forces and a vertical bending moment reduction of -82% compared to the monolithic end-joint. The influence of the local damping on the natural frequencies is negligible, but it reduces the transfer function values. This results in lower amplitudes and a faster decline of the

response in the time-domain. This is the preferred mitigation measure when large bending moment-induced stresses are expected. It is not preferred in cases where normal stresses are mainly caused by bending moments, as the costs of viscous dampers are estimated to be significantly higher than those of seismic base isolation.

- The velocity and angle of attack of a horizontally passing earthquake strongly influence the displacements and internal forces. The response is maximized (for Derince) when the horizontal shear wave velocity is 100 m/s and the primary horizontal seismic acceleration is applied in the transverse horizontal direction ($70 - 90^\circ$ angle of attack). The horizontal traveling earthquake led to an increment of stress by 50%.
- One vertical passing earthquake has been studied with a delay in arrival time due to variations in soil configuration. The earthquake arrived at the outer elements ($x = 0$ and $x = 1500m$) first and the delay increased inward to the middle of the SFT. The SFT system behaved similarly to the horizontal traveling earthquake, but with a delay from two sides instead of one. This doubled the SFT stresses (+100%). The doubling may be due to the maximum forcing acting from both sides of the SFT simultaneously. The SFT behavior to a vertical passing wave shall be studied more in depth to obtain more insight in this phenomenon.
- Soil Structure Interaction (SSI) decreased the transfer of seismic forcing in the longitudinal direction, compared to a case where SSI is not taken into account. This is presumably due to the damping and stiffness from the dynamic bedding springs. Ground displacements are not transferred 1:1 from the soil to the structure. This added flexibility might give a better representation of the actual displacements and forces at the transition structure. However, only one Comsol substructuring model is used, and the effect of the longitudinal SSI effect should be studied more in depth. On the other hand, soil in reality only has a limited shear stress capacity, causing an overestimation of Normal forces in tunnel tubes for linear non-SSI models. Linear elastic models, often overestimate this force, allowing for some degree of conservatism and safety in the global model. Eventually, the longitudinal SFT response was of minor importance compared to the transverse horizontal response, with respect to normal stresses. Applying the principal horizontal acceleration in the transverse horizontal direction gave the largest response.
- In general, SSI increased the transfer of seismic forcing in transverse directions, compared to a case where SSI is not taken into account. It shifts the natural frequencies of the SFT in all directions, and based on how it shifts relative to the earthquake Fourier spectrum, it increases or decreases the amplitudes. Therefore it is advised to prioritize the application of a rotational flexibility end-joint, as this reduces the impact of vertical and horizontal bending moments to the normal stress. The application of longitudinal flexibility should be of secondary importance since the normal forces play a smaller role in the normal stress behavior.

8.2 Recommendations for design of SFTs

For SFTs in areas with seismicity in the range of $0.05g \leq PGA \leq 0.2g$, flexible joints are preferred rather than monolithic joints. Monolithic end-joints might be applicable for slightly higher seismicities by creating a more smooth transition of the land tunnel to the SFT. This can be done by increasing the number of tethers near the land tunnel. The tether stiffness should be kept low to prevent large tether normal forces and large discontinuities in vertical shear forces of the SFT. This can be constructed using vertical highly prestressed tethers with small cross-sections or the application of inclined tethers. It will reduce the tether stiffness without reducing the cross-sectional area. In case of PGA's above 0.2g, other alternative solutions for the end-joint should be taken into consideration. This can be seismic base isolation combined with a structural fuse (max. PGA of 0.5g) or viscous dampers (max. PGA of 0.7g). Dampers are best applicable when bending moment-induced stresses should be reduced. Base isolation is best applicable when normal force-induced stresses should be reduced.

8.3 Recommendations for future research

To further improve the understanding of SFT behavior and optimize the design, the following topics might be valuable to future research:

1. The effect of end-joint opening can occur when a flexible gasket is applied. The gasket has limited deformation capacity and must remain under compression such that water tightness is guaranteed. The more rotational and translational flexibility was added at transition structure, the better the model performed for seismic loading. For these situations the end-joint opening might be the limiting factor;
2. Vertical traveling earthquakes are not considered elaborately in this research, since only one wave velocity, one soil configuration and one angle of attack has been considered. Other combinations might increase the effect.
3. Earthquakes in marine areas often lead to tsunamis or under water landslides. The combination of these effects can increase the forcing on the structure. Its likelihood and the magnitude of the combined forcing can be studied, since there is a serious risk of simultaneous occurrence;
4. Tuned-Mass-Dampers (TMD) might be applicable for SFT structures to dampen the fundamental mode or move the main mode away from problematic frequencies. In its simplest form, a combination of a spring and a mass can be applied at mid span, or multiple locations over the SFT span if necessary. The mass can have a Buoyancy-Weight-Ratio of 1.0, so no extra weight is attached to the SFT. For the spring a highly elastic material or type of damper with a physical spring build-in can be applied. In this manner the vertical and/or horizontal dynamic response can be tuned for specific frequencies. The model of this thesis can be adapted with one extra DOF containing a mass, which is connected to a SFT DOF with a translation spring or spring-dashpot element.

References

- AFAD. (2022). *Turkish disaster and emergency management authority*. Retrieved from <https://tadas.afad.gov.tr/>
- Comsol documentation. (2022). Retrieved from <https://doc.comsol.com/6.0/docserver/#!/com.comsol.help.comsol/helpdesk/helpdesk.html>
- Ditmar, P. (2021). *Cie5260-2021 structural response to earthquakes - lecture 2. part 1-3*. (Accessed: 2022-22-04)
- EC. (2022, Feb). *Transport and the green deal*. Retrieved from https://ec.europa.eu/info/strategy/priorities-2019-2024/european-green-deal/transport-and-green-deal_en
- Haji, T. K. (2017). *Evaluating the Effects of Tunnel Construction on Buildings* (Tech. Rep.). Retrieved from <http://eprints.nottingham.ac.uk/48052/1/TwanaHajiPhDthesis.pdf>
- Journée, J. M. J., & Massie, W. W. (2001). *Offshore Hydromechanics - First Edition* (Tech. Rep.). Delft: Delft University of Technology.
- Li, K., & Jiang, X. (2016). Research on Section Form of Submerged Floating Tunnels Considering Structural Internal Force Optimization under Fluid Action. In *Procedia engineering* (Vol. 166, pp. 288–295). Elsevier Ltd. doi: 10.1016/j.proeng.2016.11.551
- Li, Q., Jiang, S., & Chen, X. (2018, 12). Experiment on Pressure Characteristics of Submerged Floating Tunnel with Different Section Types under Wave Condition. *Polish Maritime Research*, 25(s3), 54–60. doi: 10.2478/pomr-2018-0112
- Long, X., Ge, F., & Hong, Y. (2015). Feasibility study on buoyancy-weight ratios of a submerged floating tunnel prototype subjected to hydrodynamic loads. *Acta Mech. Sin*(5), 750–761. doi: 10.1007/s10409-015-0428-3
- Luco, J. E., & Johnson, J. J. (1980). *Linear soil-structure interaction*. Technical Information Dept., Lawrence Livermore Laboratory.
- Martire, G., Faggiano, B., Mazzolani, F. M., Zollo, A., & Stabile, T. A. (2010). Seismic analysis of a SFT solution for the Messina Strait crossing. *Procedia Engineering*, 4, 303–310. doi: 10.1016/j.proeng.2010.08.034
- Martire, G., & Mazzolani, F. (2010). *THE DEVELOPMENT OF SUBMERGED FLOATING TUNNELS AS AN INNOVATIVE SOLUTION FOR WATERWAY CROSSINGS* (Tech. Rep.).
- Meriç, E., Görmüş, M., & Avşar, N. (2007, 4). Holocene geologic history of the Golden Horn (Istanbul, NW Turkey) based on foraminiferal data. *Journal of Asian Earth Sciences*, 30(2), 353–363. doi: 10.1016/j.jseaes.2006.10.006
- NEN-EN 1991-2 (Tech. Rep.). (2021). NEN. Retrieved from www.nen.nl
- NEN-EN 1992-1-1 (Tech. Rep.). (2011). NEN. Retrieved from www.nen.nl
- NEN-EN 1998-1 (Tech. Rep.). (2005). NEN. Retrieved from www.nen.nl
- Pecker, A. (2015). Seismic analyses and design of foundation soil structure interaction. *Geotechnical, Geological and Earthquake Engineering*, 39, 153–162. doi: 10.1007/978-3-319-16964-4\ }6
- Peters, D. (1993, may). *Tuiconstructies, constructief gedrag en optimalisering*.
- Speelman, B. (2021). *Submerged Floating Tunnel Dynamic response due to earthquakes* (Tech. Rep.). Retrieved from <https://repository.tudelft.nl/islandora/object/uuid%3Ac53b1240-35ae-4b89-b7a4-ec8ad1fef027>
- Tsouvalas, A. (2020, 9). *Lecture Notes CIE5260: Structural Response to Earthquakes* (Tech. Rep.). Delft: TU Delft.
- USGS. (2022, June). *What is directivity?* Retrieved from <https://earthquake.usgs.gov/data/rupture/directivity.php>
- Wells, G. N. (2009). *The Finite Element Method: An Introduction* (Tech. Rep.). University of Cambridge and Delft University of Technology.
- Wolfram, J. (1999). *On Alternative Approaches to Linearization and Morison's Equation for Wave*

Forces (Vol. 455; Tech. Rep.). Retrieved from <https://royalsocietypublishing.org/doi/10.1098/rspa.1999.0434>

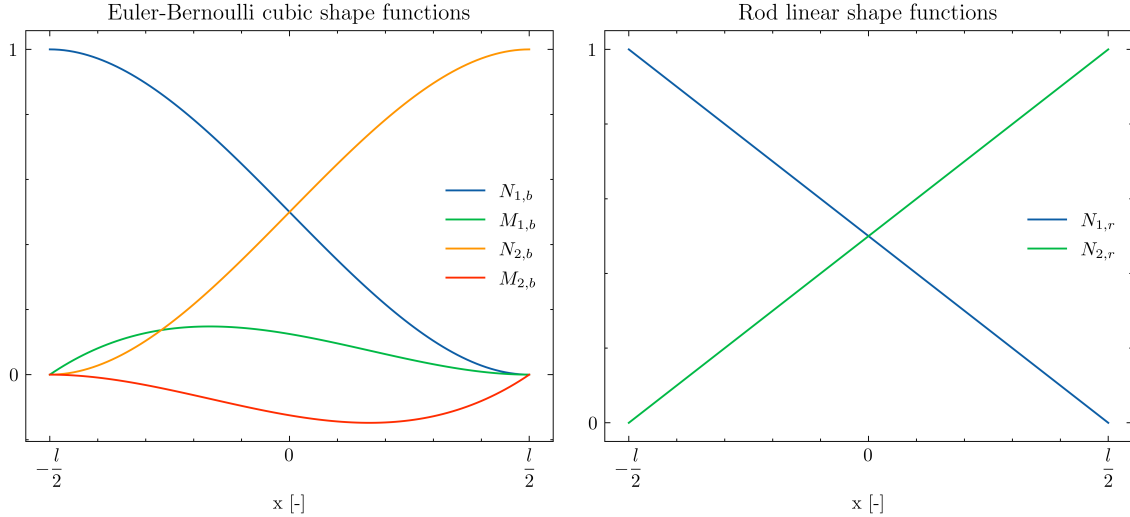
Appendices

Appendix A

Shape functions, Mass & Stiffness matrix definitions

The element mass (\mathbf{M}) and stiffness matrices (\mathbf{K}) of the 2D bending + extension beams (Euler-Bernoulli) have been obtained from the separate element mass and stiffness matrices of the 1D beam and rod respectively. The mass matrix is found using a variational approach such that the mass is distributed over the element (Wells, 2009). To apply this method, shape functions of the different element type are needed. The beam cubic shape functions with C2 continuity are applied, whereas for the rod linear shape functions with C0 continuity are applied (see Equation A.1 below). Thus moment lines will be continuous, but at element interfaces jumps will be visible in the shear force and normal force lines.

$$\left. \begin{aligned} \mathbf{N}_{\text{beam}} &= [N_{1,b} \quad M_{1,b} \quad N_{2,b} \quad M_{2,b}] \\ N_{1,b} &= \frac{-(x-x_2)^2(-l+2(x_1-x))}{l^3} \\ N_{2,b} &= \frac{x}{l} + \frac{l}{2} \\ M_{1,b} &= \frac{(x-x_1)(x-x_2)^2}{l^2} \\ N_{2,b} &= \frac{(x-x_1)^2(l+2(x_2-x))}{l^3} \\ M_{2,b} &= \frac{(x-x_1)^2(x-x_2)}{l^2} \end{aligned} \right| \begin{aligned} \mathbf{N}_{\text{rod}} &= [N_{1,r} \quad N_{2,r}] \\ N_{1,r} &= -\frac{x}{l} + \frac{l}{2} \\ N_{2,r} &= \frac{x}{l} + \frac{l}{2} \end{aligned} \quad (\text{A.1})$$



(a) Euler-Bernoulli C2 continuous shape functions

(b) Rod C0 continuous shape functions

Figure A.1: Shape function visualisation for EB-beam (left) and rod (right)

The derivation of the matrices is demonstrated in the Equation A.2 below, where l is the element length, N is a shape function and \mathbf{N} is a shape function vector. The subscript e stands for element, b for beam, r for rod and superscript "cons" for constitutive.

$$\left. \begin{aligned} \mathbf{k}_{e,b} &= EI \int_{-\frac{l}{2}}^{\frac{l}{2}} (\mathbf{N}_{,xx})^T \mathbf{N}_{,xx} dx \\ \mathbf{m}_{e,b}^{\text{cons}} &= \rho A \int_{-\frac{l}{2}}^{\frac{l}{2}} \mathbf{N}^T \mathbf{N} dx \end{aligned} \right| \begin{aligned} \mathbf{k}_{e,r} &= EI \int_{-\frac{l}{2}}^{\frac{l}{2}} (\mathbf{N}_{,x})^T \mathbf{N}_{,x} dx \\ \mathbf{m}_{e,r}^{\text{cons}} &= \rho A \int_{-\frac{l}{2}}^{\frac{l}{2}} \mathbf{N}^T \mathbf{N} dx \end{aligned} \quad (\text{A.2})$$

$$\begin{aligned}
\mathbf{k}_{e,b} &= \begin{bmatrix} \frac{12EI}{l^3} & \frac{6EI}{l^2} & -\frac{12EI}{l^3} & \frac{6EI}{l^2} \\ \frac{6EI}{l^2} & \frac{4EI}{l} & -\frac{6EI}{l^2} & \frac{2EI}{l} \\ -\frac{12EI}{l^3} & -\frac{6EI}{l^2} & \frac{12EI}{l^3} & -\frac{6EI}{l^2} \\ \frac{6EI}{l^2} & \frac{2EI}{l} & -\frac{6EI}{l^2} & \frac{4EI}{l} \end{bmatrix} & \mathbf{k}_{e,r} = \begin{bmatrix} \frac{EA}{l} & -\frac{EA}{l} \\ -\frac{EA}{l} & \frac{EA}{l} \end{bmatrix} \\
\mathbf{m}_{e,b}^{\text{cons}} &= \frac{\rho Al}{420} \begin{bmatrix} 156 & 22l & 54 & -13l \\ 22l & 4l^2 & 13l & -3l^2 \\ 54 & 13l & 156 & -22l \\ -13l & -3l^2 & -22l & 4l^2 \end{bmatrix} & \mathbf{m}_{e,r}^{\text{cons}} = \begin{bmatrix} \frac{\rho Al}{3} & \frac{\rho Al}{6} \\ \frac{\rho Al}{6} & \frac{\rho Al}{3} \end{bmatrix}
\end{aligned} \tag{A.3}$$

$$\begin{aligned}
\mathbf{m}_e^{\text{cons}} &= \rho A \begin{bmatrix} \frac{l}{3} & 0 & 0 & 0 & 0 & \frac{l}{6} & 0 & 0 & 0 & 0 \\ 0 & \frac{13l}{35} & \frac{11l^2}{210} & 0 & 0 & 0 & \frac{9l}{70} & -\frac{13l^2}{420} & 0 & 0 \\ 0 & \frac{11l^2}{210} & \frac{l^3}{105} & 0 & 0 & 0 & \frac{13l^2}{420} & -\frac{l^3}{140} & 0 & 0 \\ 0 & 0 & 0 & \frac{13l}{35} & \frac{11l^2}{210} & 0 & 0 & 0 & \frac{9l}{70} & -\frac{13l^2}{420} \\ 0 & 0 & 0 & \frac{11l^2}{210} & \frac{l^3}{105} & 0 & 0 & 0 & \frac{13l^2}{420} & -\frac{l^3}{140} \\ \frac{l}{6} & 0 & 0 & 0 & 0 & \frac{l}{3} & 0 & 0 & 0 & 0 \\ 0 & \frac{9l}{70} & \frac{13l^2}{420} & 0 & 0 & 0 & \frac{13l}{35} & -\frac{11l^2}{210} & 0 & 0 \\ 0 & -\frac{13l^2}{420} & -\frac{l^3}{140} & 0 & 0 & 0 & -\frac{11l^2}{210} & \frac{l^3}{105} & 0 & 0 \\ 0 & 0 & 0 & \frac{9l}{70} & \frac{13l^2}{420} & 0 & 0 & 0 & \frac{13l}{35} & -\frac{11l^2}{210} \\ 0 & 0 & 0 & -\frac{13l^2}{420} & -\frac{l^3}{140} & 0 & 0 & 0 & -\frac{11l^2}{210} & \frac{l^3}{105} \end{bmatrix} + \\
& \begin{bmatrix} 0 & 0 & 0 & 0 & 0 & 0 & 0 & 0 & 0 & 0 \\ 0 & \frac{13l}{35} m_{\text{add},z} & \frac{11l^2}{210} m_{\text{add},z} & 0 & 0 & 0 & \frac{9l}{70} m_{\text{add},z} & -\frac{13l^2}{420} m_{\text{add},z} & 0 & 0 \\ 0 & \frac{11l^2}{210} m_{\text{add},z} & \frac{l^3}{105} m_{\text{add},z} & 0 & 0 & 0 & \frac{13l^2}{420} m_{\text{add},z} & -\frac{l^3}{140} m_{\text{add},z} & 0 & 0 \\ 0 & 0 & 0 & \frac{13l}{35} m_{\text{add},y} & \frac{11l^2}{210} m_{\text{add},y} & 0 & 0 & 0 & \frac{9l}{70} m_{\text{add},y} & -\frac{13l^2}{420} m_{\text{add},y} \\ 0 & 0 & 0 & \frac{11l^2}{210} m_{\text{add},y} & \frac{l^3}{105} m_{\text{add},y} & 0 & 0 & 0 & \frac{13l^2}{420} m_{\text{add},y} & -\frac{l^3}{140} m_{\text{add},y} \\ 0 & 0 & 0 & 0 & 0 & 0 & 0 & 0 & 0 & 0 \\ 0 & \frac{9l}{70} m_{\text{add},z} & \frac{13l^2}{420} m_{\text{add},z} & 0 & 0 & 0 & \frac{13l}{35} m_{\text{add},z} & -\frac{11l^2}{210} m_{\text{add},z} & 0 & 0 \\ 0 & -\frac{13l^2}{420} m_{\text{add},z} & -\frac{l^3}{140} m_{\text{add},z} & 0 & 0 & 0 & -\frac{11l^2}{210} m_{\text{add},z} & \frac{l^3}{105} m_{\text{add},z} & 0 & 0 \\ 0 & 0 & 0 & \frac{9l}{70} m_{\text{add},y} & \frac{13l^2}{420} m_{\text{add},y} & 0 & 0 & 0 & \frac{13l}{35} m_{\text{add},y} & -\frac{11l^2}{210} m_{\text{add},y} \\ 0 & 0 & 0 & -\frac{13l^2}{420} m_{\text{add},y} & -\frac{l^3}{140} m_{\text{add},y} & 0 & 0 & 0 & -\frac{11l^2}{210} m_{\text{add},y} & \frac{l^3}{105} m_{\text{add},y} \end{bmatrix}
\end{aligned}$$

Figure A.2: Full mass matrix of rod + 2D beam incl. added mass

$$\mathbf{k}_e = \begin{bmatrix}
\frac{EA}{l} & 0 & 0 & 0 & 0 & -\frac{EA}{l} & 0 & 0 & 0 & 0 \\
0 & \frac{12EI_{zz}}{l^3} & \frac{6EI_{zz}}{l^2} & 0 & 0 & 0 & -\frac{12EI_{zz}}{l^3} & \frac{6EI_{zz}}{l^2} & 0 & 0 \\
0 & \frac{6EI_{zz}}{l^2} & \frac{4EI_{zz}}{l} & 0 & 0 & 0 & -\frac{6EI_{zz}}{l^2} & \frac{2EI_{zz}}{l} & 0 & 0 \\
0 & 0 & 0 & \frac{12EI_{yy}}{l^3} & \frac{6EI_{yy}}{l^2} & 0 & 0 & 0 & -\frac{12EI_{yy}}{l^3} & \frac{6EI_{yy}}{l^2} \\
0 & 0 & 0 & \frac{6EI_{yy}}{l^2} & \frac{4EI_{yy}}{l} & 0 & 0 & 0 & -\frac{6EI_{yy}}{l^2} & \frac{2EI_{yy}}{l} \\
-\frac{EA}{l} & 0 & 0 & 0 & 0 & \frac{EA}{l} & 0 & 0 & 0 & 0 \\
0 & -\frac{12EI_{zz}}{l^3} & -\frac{6EI_{zz}}{l^2} & 0 & 0 & 0 & \frac{12EI_{zz}}{l^3} & -\frac{6EI_{zz}}{l^2} & 0 & 0 \\
0 & \frac{6EI_{zz}}{l^2} & \frac{2EI_{zz}}{l} & 0 & 0 & 0 & -\frac{6EI_{zz}}{l^2} & \frac{4EI_{zz}}{l} & 0 & 0 \\
0 & 0 & 0 & -\frac{12EI_{yy}}{l^3} & -\frac{6EI_{yy}}{l^2} & 0 & 0 & 0 & \frac{12EI_{yy}}{l^3} & -\frac{6EI_{yy}}{l^2} \\
0 & 0 & 0 & \frac{6EI_{yy}}{l^2} & \frac{2EI_{yy}}{l} & 0 & 0 & 0 & -\frac{6EI_{yy}}{l^2} & \frac{4EI_{yy}}{l}
\end{bmatrix}$$

Figure A.3: Full stiffness matrix of rod + 2D beam

Appendix B

Spring-dashpot interface element definitions

The spring-dashpot interfaces at the transition between the SFT and the land tunnels are modelled using the interface elements described below. The spring coefficients can be given a high value to imitate a rotational or translational rigid connection (monolithic). Alternatively, the spring and damping coefficients can have a intermediate value (joint with bending stiffness and damping) or a zero value, such that no forces or moments due to the interfaces are exerted on the system when the connected DOFs are in motion.

$$\mathbf{k}_e^{\text{spring}} = \begin{bmatrix} k_{wx} & 0 & 0 & 0 & 0 & -k_{wx} & 0 & 0 & 0 & 0 \\ 0 & k_{Wz} & 0 & 0 & 0 & 0 & -k_{Wz} & 0 & 0 & 0 \\ 0 & 0 & k_{\theta z} & 0 & 0 & 0 & 0 & -k_{\theta z} & 0 & 0 \\ 0 & 0 & 0 & k_{wy} & 0 & 0 & 0 & 0 & -k_{wy} & 0 \\ 0 & 0 & 0 & 0 & k_{\theta y} & 0 & 0 & 0 & 0 & k_{\theta y} \\ -k_{wx} & 0 & 0 & 0 & 0 & k_{wx} & 0 & 0 & 0 & 0 \\ 0 & -k_{wz} & 0 & 0 & 0 & 0 & k_{wz} & 0 & 0 & 0 \\ 0 & 0 & -k_{\theta z} & 0 & 0 & 0 & 0 & k_{\theta z} & 0 & 0 \\ 0 & 0 & 0 & -k_{wy} & 0 & 0 & 0 & 0 & k_{wy} & 0 \\ 0 & 0 & 0 & 0 & -k_{\theta y} & 0 & 0 & 0 & 0 & k_{\theta y} \end{bmatrix} \quad (\text{B.1})$$

$$\mathbf{c}_e^{\text{dashpot}} = \begin{bmatrix} c_{wx} & 0 & 0 & 0 & 0 & -c_{wx} & 0 & 0 & 0 & 0 \\ 0 & c_{Wz} & 0 & 0 & 0 & 0 & -c_{Wz} & 0 & 0 & 0 \\ 0 & 0 & c_{\theta z} & 0 & 0 & 0 & 0 & -c_{\theta z} & 0 & 0 \\ 0 & 0 & 0 & c_{wy} & 0 & 0 & 0 & 0 & -c_{wy} & 0 \\ 0 & 0 & 0 & 0 & c_{\theta y} & 0 & 0 & 0 & 0 & c_{\theta y} \\ -c_{wx} & 0 & 0 & 0 & 0 & c_{wx} & 0 & 0 & 0 & 0 \\ 0 & -c_{wz} & 0 & 0 & 0 & 0 & c_{wz} & 0 & 0 & 0 \\ 0 & 0 & -c_{\theta z} & 0 & 0 & 0 & 0 & c_{\theta z} & 0 & 0 \\ 0 & 0 & 0 & -c_{wy} & 0 & 0 & 0 & 0 & c_{wy} & 0 \\ 0 & 0 & 0 & 0 & -c_{\theta y} & 0 & 0 & 0 & 0 & c_{\theta y} \end{bmatrix} \quad (\text{B.2})$$

Appendix C

Results

C.1 Synchronized support excitation analysis results

C.1.1 Bingol

Item	SFT with Monolithic end-joint subjected to Bingol (0.1g)					units
Joint type	Monolithic	GINA x10	GINA	GINA /10	Hinged	m/s
$w_{z,min}$	-0.009374	-0.009834	-0.010121	-0.010147	-0.010148	m
$w_{z,max}$	0.009379	0.009481	0.009249	0.009117	0.009098	m
$M_{z,min}$	-297253	-189314	-79720	-77342	-76998	kNm
$M_{z,max}$	249945	156024	82403	79919	79547	kNm
$V_{z,min}$	-5313.85	-3842.23	-3083.56	-3125.89	-3127.66	kN
$V_{z,max}$	5313.85	3842.23	3083.56	3125.89	3127.66	kN
$u_{x,min}$	-0.007824	-0.007841	-0.007883	-0.007870	-0.007824	m
$u_{x,max}$	0.010610	0.010611	0.010611	0.010611	0.010611	m
$N_{x,min}$	-33615.1	-30120.59	-19074.84	-5524.78	-33615.06	kN
$N_{x,max}$	33615.1	30120.59	19074.84	5524.78	33615.06	kN
$w_{y,min}$	-0.040000	-0.023360	-0.006575	-0.003430	-0.003439	m
$w_{y,max}$	0.039240	0.022180	0.006191	0.003412	0.003419	m
$M_{y,min}$	-4477109	-2135805	-685911	-546581	-528425	kNm
$M_{y,max}$	3636217	1695178	619705	537719	526350	kNm
$V_{y,min}$	-5313.85	-21320.65	-10730.12	-9951.98	-9876.33	kN
$V_{y,max}$	5313.85	21317.29	10731.79	9956.95	9881.28	kN
$\sigma_{sft1,min}$	-1.554	-0.997	-0.434	-0.394	-0.438	N/mm ²
$\sigma_{sft1,max}$	1.553	0.996	0.434	0.394	0.436	N/mm ²
$\sigma_{sft2,min}$	-1.031	-0.557	-0.190	-0.138	-0.213	N/mm ²
$\sigma_{sft2,max}$	1.031	0.556	0.188	0.139	0.209	N/mm ²
$\sigma_{teth1,min}$	138.19	135.16	131.86	131.14	131.05	N/mm ²
$\sigma_{teth1,max}$	174.56	171.58	172.69	173.03	173.08	N/mm ²

C.1.2 Derince

Item	SFT with Monolithic end-joint subjected to Derince (0.1g)					units
Joint type	Monolithic	GINA x10	GINA	GINA /10	Hinged	m/s
$w_{z,min}$	-0.065618	-0.054919	-0.041956	-0.041280	-0.041259	m
$w_{z,max}$	0.074314	0.060594	0.044664	0.043923	0.044046	m
$M_{z,min}$	-2799713	-1763642	-407321	-322222	-320928	kNm
$M_{z,max}$	3361975	2132500	498132	272862	271874	kNm
$V_{z,min}$	-37388.75	-24692.33	-8038.75	-4267.67	-3986.77	kN
$V_{z,max}$	37388.75	24692.33	8038.75	4267.67	3986.77	kN
$u_{x,min}$	-0.064000	-0.064040	-0.064070	-0.064040	-0.064001	m
$u_{x,max}$	0.051945	0.051882	0.051857	0.060780	0.051945	m
$N_{x,min}$	-59558.71	-55828.25	-33460.26	-21547.21	-59557.71	kN
$N_{x,max}$	59558.71	55828.25	33460.26	21547.21	59558.71	kN
$w_{y,min}$	-0.270808	-0.227590	-0.130190	-0.043771	-0.042320	m
$w_{y,max}$	0.554211	0.444900	0.161480	0.056301	0.055137	m
$M_{y,min}$	-11623236	-9685065	-2871980	-1669236	-1637245	kNm
$M_{y,max}$	17793692	13486140	3812687	1746039	1567895	kNm
$V_{y,min}$	-85853.07	-54832.22	-21448.99	-10928.21	-10143.22	kN
$V_{y,max}$	85863.49	54818.36	21453.83	10924.49	10140.46	kN
$\sigma_{sft1,min}$	-16.933	-11.127	-2.748	-1.477	-1.580	N/mm2
$\sigma_{sft1,max}$	16.931	11.125	2.748	1.477	1.579	N/mm2
$\sigma_{sft2,min}$	-4.067	-3.057	-0.869	-0.386	-0.473	N/mm2
$\sigma_{sft2,max}$	4.069	3.055	0.869	0.386	0.470	N/mm2
$\sigma_{teth1,min}$	-23.83	-38.63	-59.33	-66.06	-66.93	N/mm2
$\sigma_{teth1,max}$	354.60	350.80	359.06	363.55	364.13	N/mm2

C.1.3 Van

Item	SFT with Monolithic end-joint subjected to Van (0.1g)					units
Joint type	Monolithic	GINA x10	GINA	GINA /10	Hinged	m/s
$w_{z,min}$	-0.049953	-0.049670	-0.049306	-0.048678	-0.048560	m
$w_{z,max}$	0.047359	0.051269	0.055604	0.056084	0.056104	m
$M_{z,min}$	-1520653	-987773	-840434	-786626	-779179	kNm
$M_{z,max}$	1252883	873419	776691	761903	761132	kNm
$V_{z,min}$	-27239.87	-26086.85	-26424.41	-26061.47	-25995.32	kN
$V_{z,max}$	27239.87	26086.85	26424.41	26061.47	25995.32	kN
$u_{x,min}$	-0.041696	-0.041696	-0.041696	-0.045129	-0.041696	m
$u_{x,max}$	0.029864	0.029780	0.032159	0.037243	0.029864	m
$N_{x,min}$	-175247.27	-167883.53	-76982.80	-23092.59	-175247.27	kN
$N_{x,max}$	175247.27	167883.53	76982.80	23092.59	175247.27	kN
$w_{y,min}$	-0.528176	-0.345916	-0.070662	-0.028253	-0.028035	m
$w_{y,max}$	0.461915	0.363486	0.096354	0.041856	0.034233	m
$M_{y,min}$	-26651283	-15097443	-3645114	-2335063	-2306207	kNm
$M_{y,max}$	28255385	15159185	5368006	3233915	2951557	kNm
$V_{y,min}$	-154030.66	-112748.86	-31857.06	-26061.47	-22105.17	kN
$V_{y,max}$	154044.14	112727.65	31829.16	26061.47	22097.5	kN
$\sigma_{sft1,min}$	-8.561	-5.524	-4.044	-3.761	-3.742	N/mm2
$\sigma_{sft1,max}$	8.562	5.526	4.042	3.761	3.739	N/mm2
$\sigma_{sft2,min}$	-6.261	-3.984	-1.185	-0.714	-1.207	N/mm2
$\sigma_{sft2,max}$	6.263	3.985	1.187	0.714	1.212	N/mm2
$\sigma_{teth1,min}$	153.99	52.79	41.49	40.54	40.45	N/mm2
$\sigma_{teth1,max}$	173.60	257.89	257.22	260.65	261.03	N/mm2

C.2 Multi-Support-Excitation with various shear wave velocities - results

Item	SFT with Monolithic end-joint subjected to Derince (0.1g) with MSE and reduced tethers ($A_{teth} = 0.150m^2$)											units
v_s	100	200	300	400	500	600	700	800	900	1000	Sync.	m/s
$w_{z,min}$	-0.0436	-0.0420	-0.0419	-0.0418	-0.0418	-0.0418	-0.0418	-0.0417	-0.0416	-0.0416	-0.0414	m
$w_{z,max}$	0.0470	0.0447	0.0442	0.0441	0.0441	0.0441	0.0441	0.0440	0.0440	0.0440	0.0439	m
$M_{z,min}$	-330984	-277767	-261193	-246805	-244829	-236581	-234704	-232745	-232646	-232067	-218109	kNm
$M_{z,max}$	283706	225512	202370	200808	193440	196552	198570	193688	188348	184480	175210	kNm
$V_{z,min}$	-4042.9	-3515.5	-3248.8	-3357.5	-3186.1	-3336.7	-3167.6	-3136.9	-3103.6	-3135.8	-2924.9	kN
$V_{z,max}$	4047.4	3344.32	3032.17	3088.06	3320.01	2858.27	3005.93	3269.94	2755.6	2675.34	2924.87	kN
$u_{x,min}$	-0.0687	-0.0668	-0.0666	-0.0655	-0.0650	-0.0649	-0.0648	-0.0647	-0.0647	-0.0646	-0.0640	m
$u_{x,max}$	0.0756	0.0632	0.0603	0.0577	0.0559	0.0553	-0.0548	0.0543	0.0539	0.0536	0.0608	m
$N_{x,min}$	-20,411	-18,824	-21,860	-22,615	-22,595	-19,834	-18,841	-18,230	-17,739	-17,343	-21,547	kN
$N_{x,max}$	15,445	22,618	25,923	28,524	21,342	14,726	11,211	13,395	16,253	18,148	21,547	kN
$w_{y,min}$	-0.0423	-0.0423	-0.0423	-0.0423	-0.0423	-0.0423	-0.0423	-0.0423	-0.0423	-0.0423	-0.0438	m
$w_{y,max}$	0.05814	0.05675	0.05617	0.05586	0.05569	0.05559	0.0555	0.05543	0.05538	0.05534	0.0563	m
$M_{y,min}$	-960283	-1E+06	-2E+06	-1E+06	-1E+06	-841482	-952709	-1E+06	-1E+06	-1E+06	-2E+06	kNm
$M_{y,max}$	970565	1155833	1434605	925624	941236	778545	1201353	1244939	1087217	1180537	1746039	kNm
$V_{y,min}$	-8769.7	-8411.6	-12992	-9112.6	-8030.7	-8440.5	-11627	-8226.4	-9696.3	-10171	-10928	kN
$V_{y,max}$	8657.2	11326.1	14053.7	9289.92	9766.15	11425.8	11496.3	10601.6	9786.21	10909.8	10924.5	kN
$\sigma_{sft1,min}$	-1.49	-1.24	-1.17	-1.12	-1.10	-1.07	-1.06	-1.05	-1.05	-1.05	-1.48	N/mm2
$\sigma_{sft1,max}$	1.57	1.30	1.22	1.16	1.13	1.10	1.09	1.08	1.08	1.07	1.48	N/mm2
$\sigma_{sft2,min}$	-0.26	-0.31	-0.36	-0.29	-0.25	-0.25	-0.29	-0.31	-0.34	-0.34	-0.39	N/mm2
$\sigma_{sft2,max}$	0.24	0.33	0.42	0.30	0.26	0.20	0.25	0.26	0.28	0.26	0.39	N/mm2
$\sigma_{teth1,min}$	241.756	261.971	268.563	269.068	268.798	268.547	268.377	268.33	268.369	268.302	266.94	N/mm2
$\sigma_{teth1,max}$	722.801	705.023	699.837	698.545	698.739	698.821	698.305	698.342	698.544	698.693	699.376	N/mm2

C.3 Multi-Support-Excitation with various angles of attack - results

Item	SFT with Monolithic end-joint subjected to Derince (0.1g) with MSE and reduced tethers ($A_{teth} = 0.150m^2$)							units
α	0	15	30	45	60	75	90	$^\circ$
$w_{z,min}$	-0.043563	-0.043957	-0.04462	-0.04644	-0.04591	-0.04587	-0.040025	m
$w_{z,max}$	0.046978	0.047117	0.04731	0.04869	0.048812	0.04644	0.040295	m
$M_{z,min}$	-330984	-331443	-337006	-356750	-397634	-429218	-486646	kNm
$M_{z,max}$	283706	287671	314908	382257	392544	372995	407994	kNm
$V_{z,min}$	-4042.92	-4096.35	-4121.59	-4529.38	-5163.44	-5221.44	-5472.04	kN
$V_{z,max}$	4047.45	4153.3	4065.42	4818.35	4746.47	4799.16	5628.59	kN
$u_{x,min}$	-0.00950	-0.01097	-0.00928	-0.01412	-0.01243	-0.01780	-0.01123	m
$u_{x,max}$	0.00745	0.00845	-0.01300	0.00956	0.00878	0.01699	0.00754	m
$N_{x,min}$	-4600.48	-5027.327	-5580.31	-5785.7	-5330.53	-6870.59	-4508.58	kN
$N_{x,max}$	5634.81	6695.25	7645.59	8147.59	7012.87	10000.33	5441.31	kN
$w_{y,min}$	-0.04232	-0.048098	-0.055918	-0.061035	-0.06629	-0.06726	-0.0709	m
$w_{y,max}$	0.05814	0.07055	0.08153	0.08696	0.0873	0.083213	0.07345	m
$M_{y,min}$	-960282.97	-997843	-1150720	-1145999	-1339548	-1183054	-1035235	kNm
$M_{y,max}$	970564.54	1026273	1170132	1158588	1231440	1269897	1334833	kNm
$V_{y,min}$	-8769.67	-10118.12	-10737.03	-11207.46	-11104.93	-9978.87	-5472.04	kN
$V_{y,max}$	8657.19	9565.07	11047.83	10246	11453.38	9409.2	5628.59	kN
$\sigma_{sft1,min}$	-1.5319	-1.5281	-1.5634	-1.7276	-1.8438	-1.9593	-2.2269	N/mm ²
$\sigma_{sft1,max}$	1.5309	1.5238	1.5539	1.7304	1.8436	1.9436	2.2233	N/mm ²
$\sigma_{sft2,min}$	-0.2128	-0.2323	-0.2568	-0.2615	-0.3113	-0.2889	-0.2785	N/mm ²
$\sigma_{sft2,max}$	0.2181	0.2281	0.25998	0.2565	0.2803	0.2851	0.311	N/mm ²
$\sigma_{teth1,min}$	241.76	240.45	234.48	224.71	196.83	109.47	179.25	N/mm ²
$\sigma_{teth1,max}$	722.80	725.02	729.05	736.48	743.93	800.53	799.67	N/mm ²